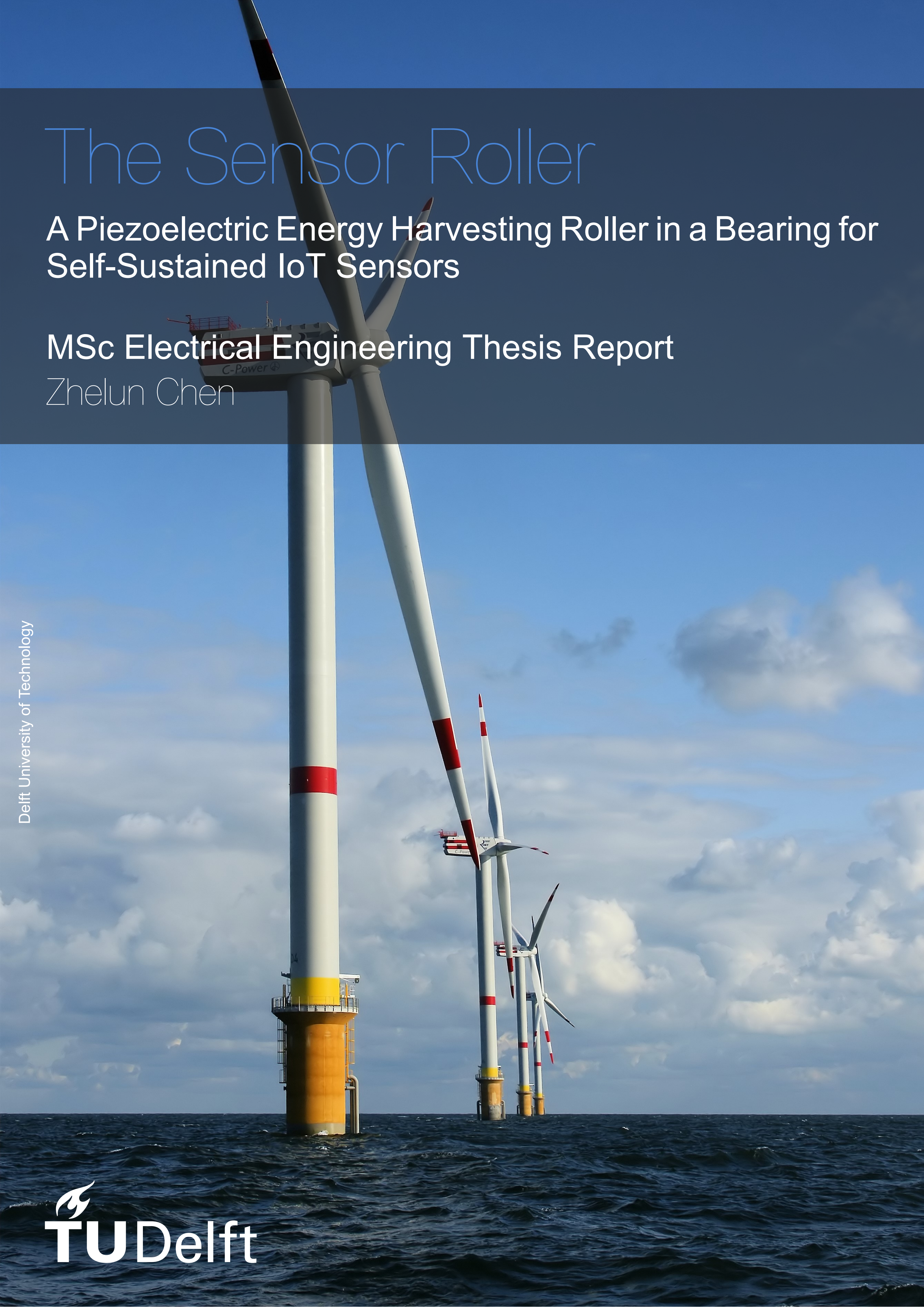

The Sensor Roller

A Piezoelectric Energy Harvesting Roller in a Bearing for Self-Sustained IoT Sensors

MSc Electrical Engineering Thesis Report

Zhelun Chen

Delft University of Technology

The Sensor Roller

A Piezoelectric Energy Harvesting Roller in a Bearing for Self-Sustained IoT Sensors

by

Zhelun Chen

to obtain the degree of Master of Science
at the Delft University of Technology,
to be defended publicly on Tuesday August 30, 2022 at 2:00 PM.

Student number:	5361060	
Project duration:	January, 2022 – August, 2022	
Thesis committee:	Dr. Sijun Du,	TU Delft, supervisor
	Prof. dr. K.A.A Makinwa,	TU Delft
	Dr. Massimo Mastrangeli,	TU Delft

TU Delft

Preface

After nearly one year of full-time research at the Electronic Instrumentation Laboratory of TU Delft, this thesis report draws my MSc student life to a perfect end. The time of the last two years at Delft was indeed a marvelous experience that I will remember for the rest of my life.
Firstly, I would like to express my sincere thanks to my supervisor Dr. Sijun Du for his dedicated and passionate guidance. In addition, I would also like to thank Andre and Ben of SKF for their collaboration on this project. Then I would like to thank all the Power Management research team members, who gave me a lot of help during my research. Besides, I also would like to thank all my friends for the joyful time we have had together during the two years. Finally, I want to thank my parents for their support and encouragement.

Zhelun Chen
Delft, August 2022

Abstract

With the high-speed development of the Internet of Things (IoT), powering such a massive number of wireless IoT sensors with chemical batteries become more and more unpractical. To make the IoT sensors self-sustained, Piezoelectric Energy Harvesting (PEH) technology provides an excellent solution to power the devices with a relatively long service time. By harvesting the ambient mechanical vibrations, PEH could generate a stable power source without wind or light.

Currently, the famous bearing manufacturer, SKF, collaborates with TU Delft to design a self-sustained smart IoT roller with PEH technology, which will be implanted in huge bearings, such as the bearing in the wind turbines. This thesis project is a feasibility study investigating the possibility of replacing the chemical battery with the Piezoelectric Energy Harvester in SKF's smart IoT roller, called Sensor Roller.

The objective of this project includes the system design of two generations of the prototype harvester. The first prototype concentrates on the properties of the piezoelectric material, while the second prototype focuses on the structure of the harvester. The design work consists of the raw data analysis of the target roller from SKF and the prototype construction and simulation in COMSOL Multiphysics. Besides, to make the results more reliable, two stages of the test with the practical components are made to study the harvester's performance under the actual working condition of the roller in the bearing. As a result, a tube shape Piezoelectric Energy Harvester with suitable materials and parameters is built. According to the simulation results, under a safe pressure level of the piezoelectric material, the proposed harvester achieves $8.1mW$ *output power, which is enough for the loading sensors. The designed Piezoelectric Energy Harvester is being manufactured at present, and it is planned to be installed in the target roller to get the system-level test in the future.*

In addition to the harvester, some rectifiers are designed and taped out to improve the performance of the proposed Piezoelectric Energy Harvesting system. Three rectifiers are made with the Silicon Carbide (SiC) process to obtain a high voltage and temperature tolerance: a Full Bridge Rectifier (FBR), a Passive Rectifier, and a Synchronized Switch Harvesting on Inductor (SSHI) rectifier. Meanwhile, another SSHI rectifier is made with the $0.18\mu m$ *Silicon BCD process that focuses on solving the cold-startup problem. Consequently, simulated with the real transducer of the proposed harvester, both the FBR circuit and the Passive Rectifier circuit with the SiC process achieve over* $10mW$ *output power, and the SiC SSHI circuit achieves* $37.1mW$ *output power. As for the cold-startup SSHI rectifier circuit, it successfully reduces the required open circuit voltage by* $4\times$ *to start up the SSHI system from the cold state.*

The results of this project show the great potential for applying the Piezoelectric Energy Harvesting technology to power the IoT sensors in the roller of bearing. Although some future works should be finished to build the commercial version of the energy harvesting roller, we are convinced that the fully self-sustained Sensor Roller with Piezoelectric Energy Harvesting technology will possibly show up in the near future.

Contents

Preface i

Summary ii

1 Introduction 1
- 1.1 Background 1
- 1.2 Project objectives 2
- 1.3 Project workflow 4
- 1.4 Thesis outline 4

2 Literature Review 5
- 2.1 Introduction to Piezoelectricity 5
  - 2.1.1 Piezoelectric effect 5
  - 2.1.2 Mathematical description 6
  - 2.1.3 Piezoelectric material and polarization 6
- 2.2 Piezoelectric energy harvesting applications 8
  - 2.2.1 Applications in transportation 8
  - 2.2.2 Applications in body movement 9
- 2.3 Piezoelectric energy harvesting rectifiers 10
  - 2.3.1 Full-bridge rectifier 11
  - 2.3.2 SSHI circuit 12
- 2.4 Conclusion 13

3 Harvester design 14
- 3.1 Workflow 14
- 3.2 Overview of the target roller 14
- 3.3 Raw data analysis 15
  - 3.3.1 Raw data from the SKF 15
  - 3.3.2 Dynamic stress analysis 16
  - 3.3.3 Introduction to COMSOL 18
  - 3.3.4 Feasibility simulation 18
- 3.4 First prototype design 20
  - 3.4.1 Structure design 20
  - 3.4.2 Time-dependent simulation 21
  - 3.4.3 Output power simulation 23
- 3.5 First prototype test 25
  - 3.5.1 Preparations and settings 25
  - 3.5.2 Destructive test 26
  - 3.5.3 Verification test 26
- 3.6 Second prototype design 28
  - 3.6.1 Supporting material simulation 28
  - 3.6.2 Piezoelectric material simulation 29
  - 3.6.3 Structure design 31
  - 3.6.4 Prototype structure simulation 32
  - 3.6.5 Preload design 35
  - 3.6.6 Summary 36
- 3.7 Second prototype test 37
- 3.8 Conclusion 37

4 Rectifier design 38
- 4.1 Rectifier circuits with the SiC technology 38

    - 4.1.1 Introduction to the SiC technology . . . 38
    - 4.1.2 FBR circuit with the SiC technology . . . 39
    - 4.1.3 Passive rectifier circuit with the SiC technology . . . 40
    - 4.1.4 SSHI rectifier circuit with the SiC technology . . . 40
    - 4.1.5 Results . . . 41
    - 4.1.6 Conclusion . . . 42
  - 4.2 Cold-startup SSHI rectifier circuit . . . 43
    - 4.2.1 Proposed design analysis . . . 43
    - 4.2.2 System architecture . . . 45
    - 4.2.3 Circuit implementation . . . 46
    - 4.2.4 Results . . . 47
    - 4.2.5 Conclusion . . . 49

5 Conclusion and future work 50
  - 5.1 Summary . . . 50
  - 5.2 Conclusion . . . 51
  - 5.3 Future work . . . 51
    - 5.3.1 Planned tests . . . 51
    - 5.3.2 Future harvester design . . . 53
    - 5.3.3 Future circuit design . . . 53

References 54

A Publication I 57

B Publication II 63

1

Introduction

This chapter introduces the main research themes of the thesis project "A Piezoelectric Energy Harvesting Roller in a Bearing for Self-Sustained IoT Sensors". In this chapter, a background of this project is firstly presented. Then the objectives and the workflow of this project will also be introduced. Finally, to help the readers better understand this thesis report, the outline is shown at the end of this chapter.

1.1. Background

In recent years, The Internet of Things (IoT) has kept a high speed of growth, especially for wireless IoT applications. As the report is shown in Fig. 1.1, the number of global IoT devices grew by 8% in 2021, and it will continue to grow in the next few years. Among these enormous number of IoT devices, wireless IoT devices take a large proportion.

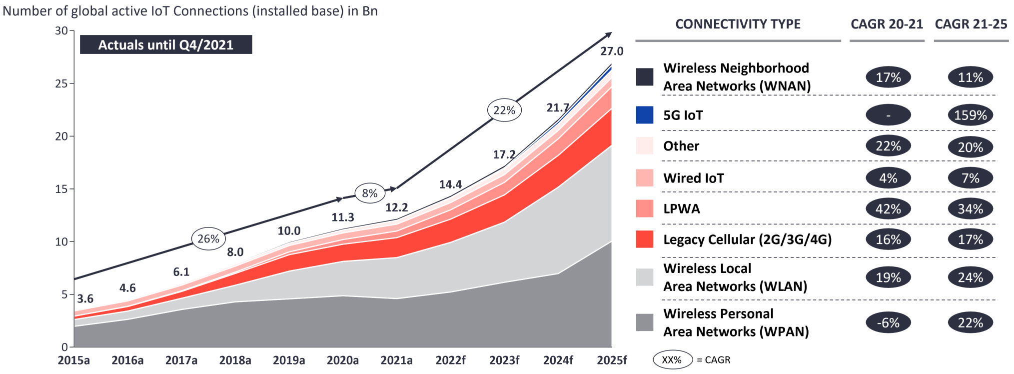

Figure 1.1: Global IoT market forecast (in billion connected IoT devices).[1]

Compared with wired IoT devices, wireless IoT devices have many advantages. For example, wireless IoT devices have better accessibility because wires do not limit their communication. Besides, wireless IoT device is easier to be installed since no more cables are needed, which are challenging to be connected and set up.

However, the power supply is a big challenge for wireless IoT devices. Without the wire or cable, the chemical battery is the most straightforward choice to provide the power. However, using the chemical battery to power the massive number of wireless IoT devices is not sustainable in many aspects. Firstly, manufacturing such a considerable amount of chemical batteries will cost a lot of the metal resources of the earth, such as Lithium and Lead. Secondly, the disposal of a big number of used batteries significantly damages the environment. For example, a trillion exhausted coin batteries are near the same volume as the stones to build 500 copies of the Colosseum in Rome [2]. Thirdly, due to the battery's limited service time, replacing the exhausted batteries is also a huge cost. Many wireless IoT devices are planted at extreme places that are hard to replace, such as underwater [3] and underground [4].

Therefore, compared with using the battery, energy harvesting technology is an excellent solution to power the wireless IoT devices and avoid the problems above. With the energy harvesting technology, it is possible to power the IoT device with the energy harvested from the surrounding environment, and the battery is not needed anymore.

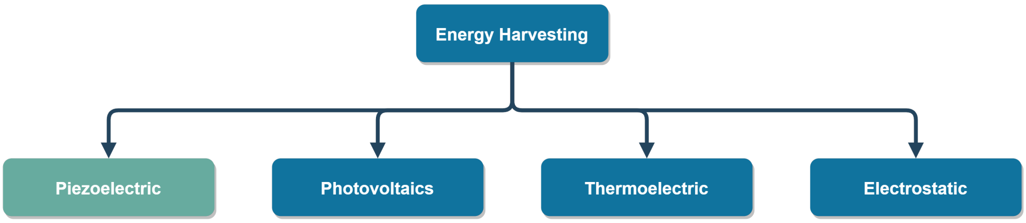

Figure 1.2: Energy harvesting sources.

In recent years, energy harvesting technology received a lot of research interest. There are many small-scale energy sources that can be harvested, such as piezoelectric, photovoltaic, thermoelectrics, and electrostatic, as shown in Fig. 1.2. There are also a lot of studies and applications based on these energy sources [5] [6] [7] [8]. Among these energy harvesters with different energy sources, piezoelectric has become more and more popular since it is easy to integrate with CMOS technology and has a high power density. Besides, the Piezoelectric energy harvester obtains the power from the ambient vibrations. Hence, compared with other energy harvesting technology, the piezoelectric energy harvester could be installed in many places even without any sunlight or wind. Therefore, Piezoelectric energy harvesting is a great choice to power wireless IoT devices in various scenarios. A report shows that the piezoelectric energy harvesting technology led the market in 2020, taking nearly half of the revenue share [9].

1.2. Project objectives

In this Big Data era, information plays an essential role in many fields, especially in industry. To collect and analyze the critical data and provide better products to the customers, a Swedish bearing and seal manufacturing company, SKF [10], is developing a commercial IoT device: the Sensor Roller.

Figure 1.3: Wind turbine bearing with the Sensor Roller.[11]

As Fig. 1.3 is shown, the Sensor Roller is usually implanted in a large bearing to support the rotation of the bearing, such as the bearing in the wind turbine. But different from the traditional roller, there is a bore in the middle of the roller that contains some smart sensors (the white part in the figure), which can collect some important information about the bearing. With the help of the radio frequency (RF) module in the Sensor Roller, the collected information of the bearing is able to be transferred wirelessly.

As for the bearing, there is much critical information during the operation, such as temperature, load, and rotation speed. By collecting and analyzing this information, many extra functions can be built. For example, the customers can use the data to monitor the performance of the bearing remotely, and the engineers can use the data to check the bearing's health conveniently. However, the power supply is a huge problem for this current Sensor Roller. Fig. 1.4 shows the inside view of the Sensor Roller, and it shows that all the electric components are powered by a Lithium battery.

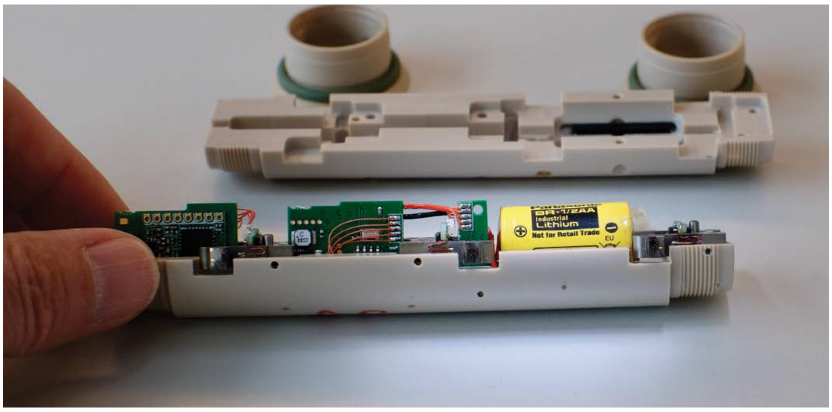

Figure 1.4: Inside view of the Sensor Roller.

Like most IoT devices powered with batteries, the service life of the Sensor Roller is highly dependent on the battery. Besides, replacing the battery in the Sensor Roller is nearly impossible since disassembling the bearing and installing the roller are very difficult after the bearing is installed.

To solve Sensor Roller's power supply problem, SKF decides to collaborate with TU Delft to design a new generation of the Sensor Roller, which will consist of a piezoelectric energy harvesting system as the power source. Powered by the piezoelectric energy harvester, the service life of the Sensor Roller will be significantly increased.

Therefore, the main objective of this project is to design a prototype of the piezoelectric energy harvesting system, in order to figure out the feasibility of using the piezoelectric energy harvester to replace the battery. To be more specific, the loading sensors of the current Sensor Roller need at least the power of $5mW$, hence, the goal of this project is to check the possibility of generating more than $5mW$ power with the proposed piezoelectric energy harvesting system.

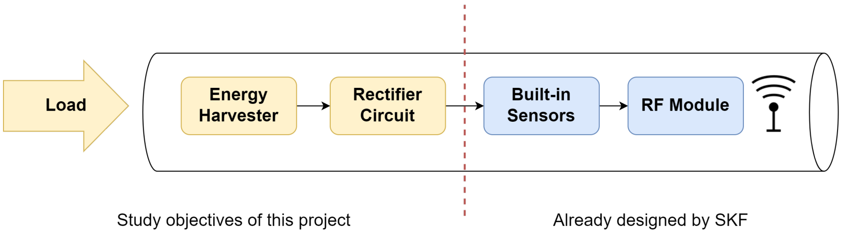

Figure 1.5: Objectives of the Sensor Roller.

Fig. 1.5 shows the study objectives of this project from the aspect of the Sensor Roller's system architecture. In the figure, on the left side of the red dash line, three yellow blocks are the three main study objectives of this project. Firstly, the mechanical load as the input to the harvesting system should be carefully analyzed. A clear understanding of the input load will help the further design of the harvester. Secondly, the piezoelectric energy harvester should be designed, which is the core work of this project. This design work includes the simulation and analysis of the piezoelectric material, the harvester structure design, the system-level test, etc. Thirdly, the rectifier circuit also should be designed to provide a suitable power source for the built-in sensors. By applying some cutting-edge rectification techniques, the output power of the harvester could be significantly increased. The blue blocks on the right represent the other tasks to build the Sensor Roller, which do not belong to the objectives of this project because they are already finished by SKF.

1.3. Project workflow

Fig. 1.6 shows the Gantt chart that introduces the workflow of the project. There are mainly two parts of the work: energy harvester design (green blocks in the chart) and rectifier circuit design (blue blocks in the chart). These two parts of work focus on the different domains of the Sensor Roller, and they are processed with different tools and software, hence, the two parts of work are planned to run simultaneously.

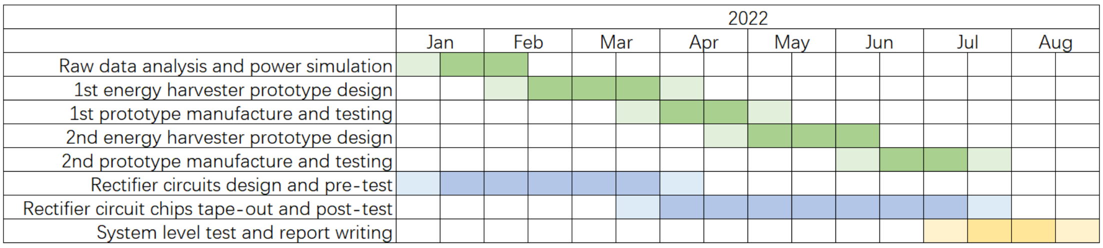

	2022															
	Jan		Feb		Mar		Apr		May		Jun		Jul		Aug	
Raw data analysis and power simulation	░	🟩	🟩													
1st energy harvester prototype design			░	🟩	🟩	🟩	░									
1st prototype manufacture and testing						░	🟩	🟩	░							
2nd energy harvester prototype design								░	🟩	🟩	🟩					
2nd prototype manufacture and testing											░	🟩	🟩	░		
Rectifier circuits design and pre-test	░	🟦	🟦	🟦	🟦	🟦	░									
Rectifier circuit chips tape-out and post-test						░	🟦	🟦	🟦	🟦	🟦	🟦	🟦	░		
System level test and report writing													░	🟨	🟨	░

Figure 1.6: Gantt chart of the project.

As for the part of energy harvester design, there are two generations of the energy harvester prototype that are planned to be built and tested. The first prototype will design a simple harvester to figure out the feasibility of the project and study the properties of the piezoelectric material, and the second prototype will design a harvester that can be embedded and tested in the real roller and try to improve its performance. As for the part of rectifier circuit design, more than one rectifier circuit will be built with different processes and techniques, in order to increase the power transfer efficiency of the energy harvesting roller.

In this chart, many tasks will be finished with the help of third parties, such as the manufacture of the harvester's material and tape-out of the rectifier chips. Therefore, the project schedule will be adjusted according to the real progress.

1.4. Thesis outline

This thesis outline is organized as follows: In chapter 1, a basic introduction is presented to show the central study theme and goal of this project and illustrate the objectives and workflow of this project. In chapter 2, the theories related to the energy harvesting roller are discussed. Some relevant research and publications are also introduced. In chapter 3, the details of the two generations of the harvester design are carefully presented. The results of the simulations and tests are included in this chapter. In chapter 4, the design of the rectifiers with different techniques and processes are shown, and the simulation results of these circuits are also presented. In chapter 5, a conclusion of this project is drawn. The results of the project are discussed, and future work is planned in this chapter. Furthermore, the list of references and two publications during the project are shown at the end of this report.

2

Literature Review

In this chapter, some background knowledge related to the project is introduced. Firstly and also most importantly, the theory of piezoelectricity will be introduced. By introducing the theory, the design principle behind the energy harvester could be better understood. Secondly, based on piezoelectricity, some well-designed piezoelectric energy harvesting applications are shown. The ideas of these applications are helpful to design the energy harvesting roller. Finally, the piezoelectric energy harvesting rectifiers are discussed, which have a significant influence on the performance of the harvester.

2.1. Introduction to Piezoelectricity

Before making use of piezoelectricity to design the energy harvester, two questions should be figured out: what is piezoelectric energy, and how to harvest it, and this section focus on the first question.

2.1.1. Piezoelectric effect

Around 140 years ago, two French brothers, Pierre Curie and Jacques Curie first discovered the piezoelectric effect [12]. The piezoelectric effect can be simply expressed as: when a piezoelectric material is deformed by an external squeezing, an electric field (and the corresponding electric charges) across the material is generated. In this process, the mechanical energy is transferred into electric energy, this is the direct piezoelectric effect. This process is reversible, called the inverse piezoelectric effect: by applying the voltage to a piezoelectric material, a mechanical deformation can be observed.

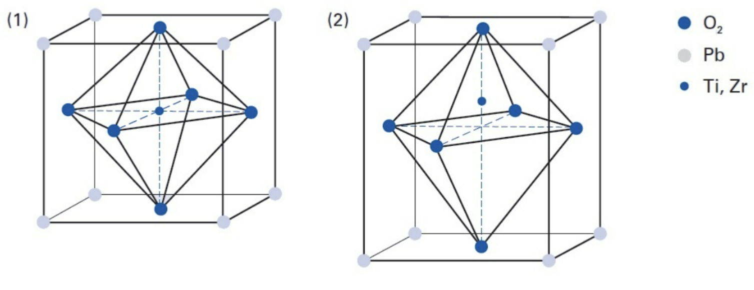

Figure 2.1: PZT crystal unit: (1) default situation (2) apply a strain. [13]

From a view of the microcosm, the piezoelectric effect is easier to understand. In Fig. 2.1, two Lead Zirconate Titanate (PZT) crystal units are shown. The big blue balls in the figure represent the oxygen atoms, which have the negative charge, while the grey balls and the small blue ball represent the lead atoms and the Zirconate or Titanate atoms, respectively, and they have the positive charge. The left crystal unit (1) is under the default situation while this is no external stress applied to it. According to the polarity of the crystal's atom, the positive charge center is at the same position as the negative charge center. Therefore, it is an electrical neutralization situation, and this is no electric field.

However, as the left crystal units (2) shown, when it is deformed by the external stress, the central Zirconate or Titanate atom will be displaced. This lead to the shift of the positive charge center and the electrical neutralization situation is broken. Consequently, an electric field is formed in this crystal unit, and the free charge is this crystal will be moved by the formed electric field. Those moving charges can be collected as a form of electrical energy.

2.1.2. Mathematical description

After understanding the mechanism of the piezoelectric effect, using the mathematical formula to describe this effect is necessary. The mathematical description starts with the linear electrical behavior of the material:

$$D = \varepsilon E \tag{2.1}$$

where D is the electric displacement field, ε is the absolute permittivity, and E is the electric field. Then we introduce Hooke's law for linear elastic materials:

$$S = sT \tag{2.2}$$

where S is the strain, s is the stiffness of the material, and T is the stress. Then with the kinematic relation, where u is the displacement vector:

$$S = \frac{\nabla u + u\nabla}{2}, \quad \nabla \cdot T = 0 \tag{2.3}$$

Combine the equation (2.1), (2.2) and (2.3) into the coupled tensor equations of the strain-charge form:

$$\begin{aligned} S &= sT + \partial^t E \\ D &= \partial T + \varepsilon E \end{aligned}$$

where ∂ is the piezoelectric tensor, and the ∂^t is the transpose matrix of it. With the coupled tensor equations, the relationship between the mechanical domain and electric domain is nicely described mathematically. These equations are widely used in finite element modeling and they are only suitable with small mechanical amplitudes and electric field so-called small-signal value.

2.1.3. Piezoelectric material and polarization

Selecting a suitable material is an essential task in harvester designing. The piezoelectricity is exhibited in many materials, such as Quartz, Topaz, Zinc oxide, and polymers. However, not all piezoelectric materials are suitable for energy harvesting applications. In recent research, there are mainly three types of piezoelectric materials that have been used in energy harvesting design: Lead Zirconate Titanate ceramic, polyvinylidene fluoride (PVDF), and piezo fiber [14]. These three materials show their own expertise in different application circumstances.

Figure 2.2: Piezoelectric devices with PZT material. [15]

Lead zirconate titanate ceramic, also known as PZT, is the most popular material in energy harvester design because it has some obvious advantages. Firstly, PZT ceramics are physically strong and chemically inert, hence the manufacturing cost is relatively low. Secondly, PZT ceramics can be easily shaped into various geometries, such as plates and tubes, as shown in Fig. 2.2. Finally, PZT ceramics also have a high coupling and high charge sensitivity with a high operating temperature compared with other materials [16].

However, PZT ceramics also show some disadvantages in the application. Like other ceramics materials, PZT ceramics lack flexibility. When the deformation is over its tolerance, the whole ceramic will be crushed into small pieces. In energy harvester design, since most of the harvesters are working in a dynamic state, it is necessary to avoid the PZT ceramics being crushed.

Another wild-used piezoelectric material is PVDF, Polyvinylidene fluoride, or polyvinylidene difluoride. This material is produced by the polymerization of vinylidene difluoride and shows strong piezoelectricity than other polymers. In piezoelectric applications, film shape PVDF material is most commonly used, which is shown in Fig. 2.3. Due to the piezoelectricity in PVDF, PVDF film can be used in piezoelectric sensors, energy harvesters, and actuators.

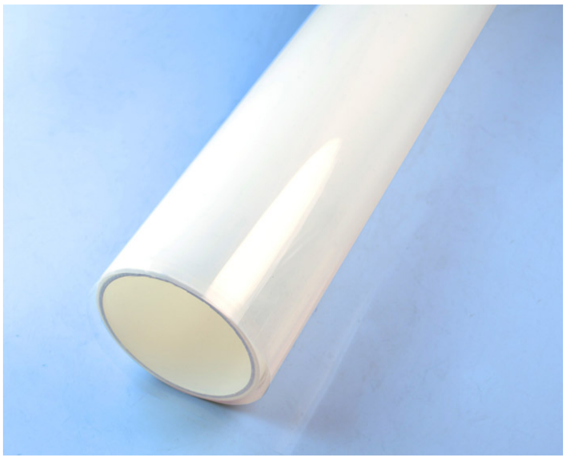

Figure 2.3: PVDF Films. [17]

Unlike the PZT ceramic, PVDF film has a great advantage in that it is much softer and more flexible. However, the piezoelectricity of PVDF is much less than PZT. For example, the piezoelectric charge coefficient in PZT is around 100 times larger than PVDF, and the relative permittivity in PZT is also 1000 times larger than PVDF [18]. These two parameters play very important roles in the output power of the piezoelectric energy transducer.

The third piezoelectric material is the piezo fiber, the nanofiber manufactured with different materials and methods [19]. Since the piezo fiber is usually thin and small, it could be used in many nanoscale applications. For example, Chen et al.[20] used the PZT nanofiber (Fig. 2.4 (b)) to design a nanogenerator (Fig. 2.4 (a)) for mechanical energy harvesting. The PZT nanofiber they used has a diameter of 60 nm and a length of 500um.

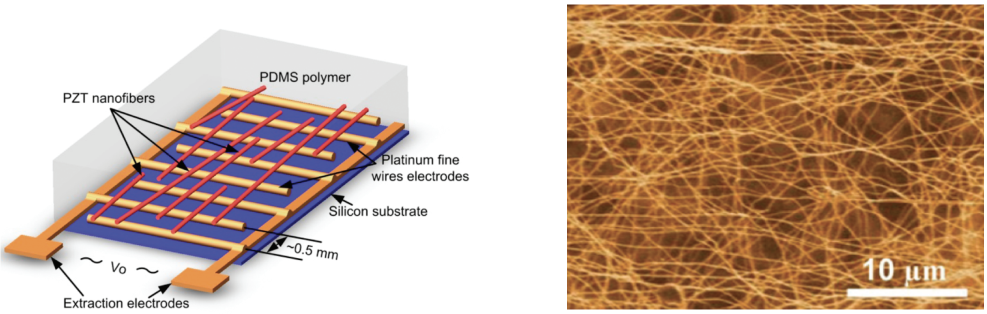

(a) Schematic view of the piezo fiber generator.

(b) Scanning electron microscopy image of the piezo fiber.

Figure 2.4: Example of the piezo fiber. [20]

But piezo fiber also has its disadvantages. On the one hand, most of the piezo fiber is in the experimental stage and has not been mass-produced, therefore, it is hard to directly purchase suitable piezo fiber to use in this project. On the other hand, the volume of piezo fiber is at the micrometer's arrange, but the volume of the roller in this project is much large than the fiber, hence, a huge amount of the piezo fiber could be used to build the harvester, which is not an economic and reasonable solution.

Besides the material, another problem that should be considered is the polarization of the piezo material. In nature, crystallites of piezo material are randomly oriented, as shown at the left of Fig. 2.5. In this situation, the piezoelectric behavior in the material is relatively weak. Therefore, to have a better piezoelectric performance, the origin piezo material should be polarized by applying a strong electric field to make most of the crystallites have the same orientation, as shown at the right of Fig. 2.5. The characteristic of certain materials is termed ferroelectricity.

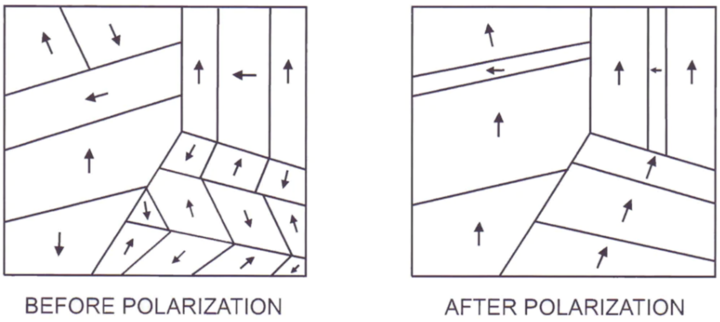

Figure 2.5: Principle of the ferroelectric polarization. [21]

Due to the piezo material having ferroelectric polarization, in the energy harvester design, the compressive stress should be applied to the same direction of polarization to get the best performance. Besides, the generated electric field is along the poling axis, therefore, the positive and negative electrodes should be located on the two sides of the poling axis to better harvest the generated charge.

Another problem that should be considered is depolarization. Under huge compressive stress, the ferroelectric material could be depolarized. The degree of the depolarization will influence the harvester's performance, and it is related to many factors, such as the loading force, loading time and working temperature [22]. Consequently, when designing the piezo energy harvest, we should avoid depolarization to make the harvester has a better performance and longer work life.

2.2. Piezoelectric energy harvesting applications

With the fast development of IoT devices, piezoelectric energy harvesting becomes an alternative energy supply solution to replace the traditional battery. By applying piezoelectric energy harvesting technology, some IoT devices are able to power themselves, called self-sustained devices, which reduce environmental pollution and save a lot of chemical battery use. In recent years, there are many piezoelectric energy harvesting applications appear in different domains, and the ideas of these novel designs are helpful to reference for this project.

Generally, the applications of piezoelectric energy harvesting focus on these fields: transportation, structures, aerial applications, in-water applications, smart systems, microfluidics, bio-medicals, wearable, and implantable electronics [23]. Considering the device's scale and the level of input energy, the applications in two fields are more helpful and related to our project: transportation and body movement. Some of the applications in these two fields will be introduced in this section.

2.2.1. Applications in transportation

Modern transportation gives people the convenience to move at a high speed and a comfortable experience. However, only a small portion of the energy is used to overcome the friction during the vehicle's moving, and a big amount of energy is wasted in the form of mechanical energy and heat. piezoelectric energy harvesting makes it possible to reuse part of the wasted mechanical energy, such as from the road and from the tires.

The train usually has a fast speed and heavyweight and plays an important role in the modern transportation system. Some piezoelectric energy harvesters are designed to absorb the energy from trains to power some IoT nodes on the rail. Gao et al. [24] designed a piezoelectric energy transducer with a PZT cantilever piezoelectric beam (Fig. 2.6), which can be clamped at the end of the rail. When a train passes by the rail, the interaction between the wheels of the train and the rail transfers the mechanical energy to the piezoelectric beam and finally become electric energy by the transducer. According to their testing, with the realistic assumption, a peak-peak output power of $4.9mW$ and output voltage of $22.1V$ can be achieved.

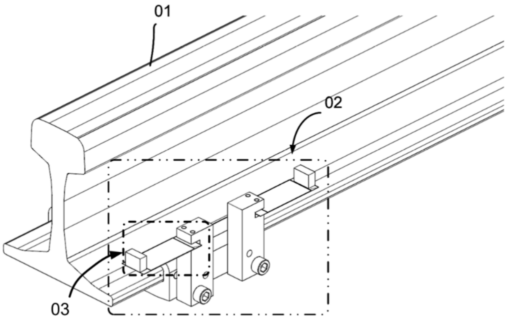

Figure 2.6: Configuration of the rail-borne piezoelectric transducer. [24]

Speed bumps on the road are designed to control the speed of the vehicles to keep traffic safe. The mechanical energy transferred into the speed bump from the passing vehicles also can be harvested to power some IoT devices, such as car detection sensors. To make these sensors become self-sustained, Chen et al. [25] designed a piezoelectric vibration cantilever energy harvester to absorb the energy from a speed bump. Fig. 2.7 shows the structure of the harvester. In this structure, they use a striking bar (c) and springs (d) to transfer the striking force of the passing vehicle to the piezoelectric cantilevers. Besides, they also design a low-power power management circuit to control the harvested energy. Finally, $1.26mJ$ of energy can be harvested when one car passes the speed bump.

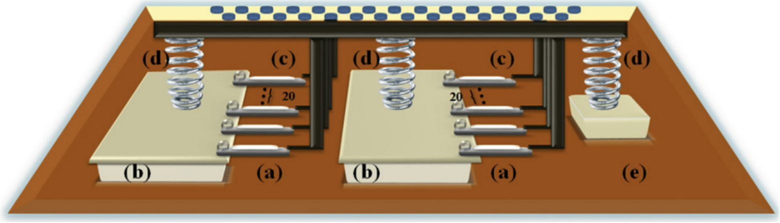

Figure 2.7: Structure of piezoelectric vibration cantilever energy harvester for the speed bump. [25]

Nowadays, more and more sensors are used in vehicles, therefore, the piezoelectric energy harvesting system comes in handy to power these sensors. For example, the tires of vehicles are the possible place to apply this technique. Esmaeeli et al. [26] introduced a rainbow piezoelectric energy harvesting system to power the monitoring sensors in the tire. They used a flexible metal substrate and a piezoelectric material layer to build the rainbow-shape harvested as shown in Fig. 2.8. This structure is helpful to transform the strain energy of the tire into electric energy to power the loading sensors. According to their simulation, this design achieves a $9.7V$ and $5.85mW$ of maximum output voltage and power.

2.2.2. Applications in body movement

The movement of the human body is a good mechanical power source for piezoelectric energy harvesting. By harvesting the energy of body movement, many wearable and mobile devices can be powered.

Walking is one of the body movements with the highest frequency in our daily life, and it is also a potential mechanical energy source for piezoelectric energy harvesting. Turkmen et al. [27] built the shoes with piezoelectric material to harvest the walking energy of humans. They put a cymbal shape piezoelectric energy harvester (shown in Fig. 2.9) inside the sole of the shoes. When a human is

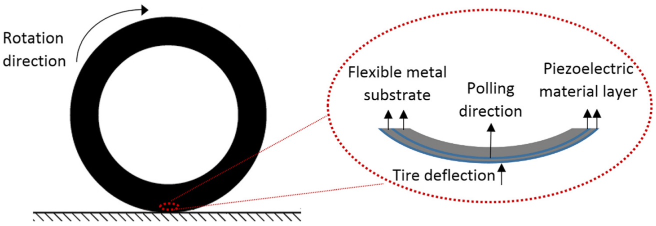

Figure 2.8: The rainbow-shaped PZT is mounted on the inner layer of the tire. [26]

wearing shoes and walking, the footfall on the sole will apply stress on the top of the cymbal, and then transformed into a displacement along the piezoelectric material bar (the brown part in the figure), and finally, the electric energy will be harvested by the piezoelectric material. As the result of their analysis, when a human of $90kg$ is using these shoes, a $1.43mW$ of electrical power can be harvested.

Figure 2.9: Cymbal shape piezoelectric energy harvester. [27]

In addition to walking, other human body movements also could be harvested by applying piezoelectric material. Jung et al. [28] designed a curved piezoelectric generator to harvest the energy from human body movement and power wearable devices. As Fig. 2.10 shows, two separated curved piezoelectric generators are back-to-back connected. Each generator consists of some layers, including two piezo layers made of PVDF. This generator can be installed in many places around the human body, such as in watches and clothes. In the testing, the curved piezoelectric generator produced $3.9mW/cm^2$ of output power density, and it lit up 476 LED bulbs successfully.

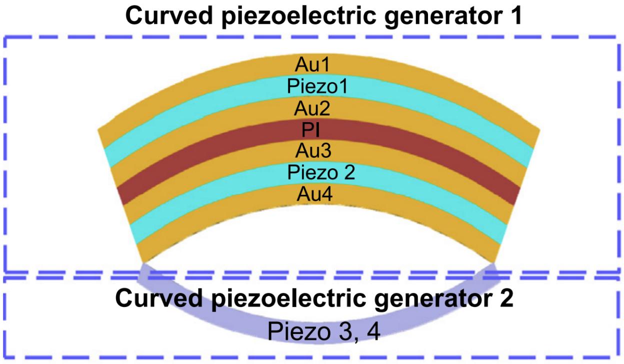

Figure 2.10: Structure of the curved piezoelectric generator. [28]

2.3. Piezoelectric energy harvesting rectifiers

After designing the structure of the harvester with piezoelectric materials, the rectifier is needed to provide a stable electric signal to the loading devices. To design the rectifier from the circuit aspect, the electric input from the piezoelectric material should be introduced. The left part of Fig. 2.11 shows the electromechanical model of the piezoelectric element in energy harvesting [29], and it is divided into the mechanical domain and the electrical domain.

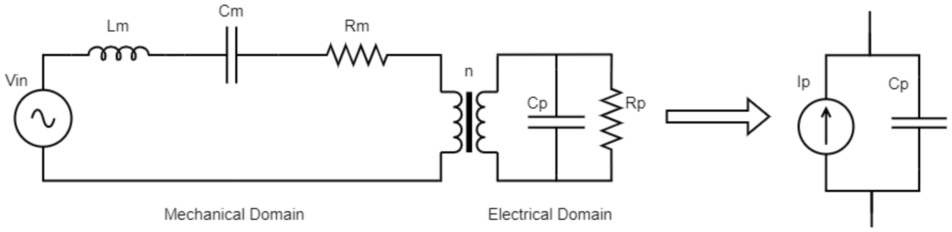

Figure 2.11: Equivalent circuit of the piezoelectric material.

In this figure, L_m represents the mechanical mass of the piezoelectric material, C_m represents the mechanical stiffness of the material, R_m shows the mechanical loss of the system, and V_{in} is the exciting velocity of the external exciting force on the piezoelectric material. This mechanical domain is coupled with the electrical domain by a transformer. In the electrical domain, C_P represents the inner capacitance of the piezoelectric material, paralleled with a resistance R_P. When the piezoelectric material is close to its resonance and the frequency of the external force is relatively high, the electromechanical model can be simplified into the equivalent circuit as shown in the right of Fig. 2.11. The equivalent circuit includes a sinusoidal current source I_P and a parallel capacitance C_P. With the equivalent circuit of the piezoelectric transducer (PT), some rectifier circuits will be introduced, to increase the power extraction efficiency of the energy harvesting system.

2.3.1. Full-bridge rectifier

Fig. 2.12 shows the circuit of the full-bridge rectifier (FBR), which is the simplest and also most commonly used rectifier to convert the AC voltage from the output of a piezoelectric harvester into a DC voltage.

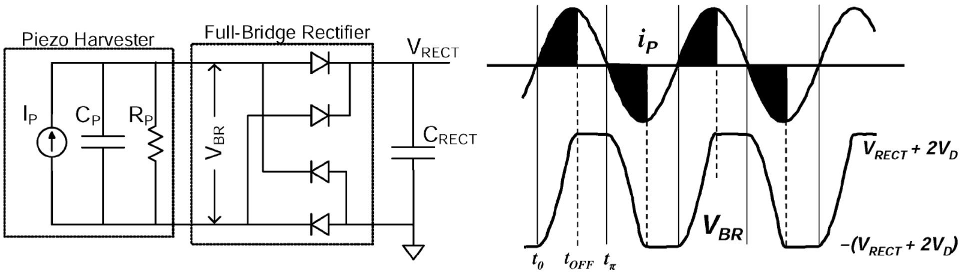

Figure 2.12: The full-bridge rectifier with associated simulated voltage and current waveform. [30]

The FBR is popular because it is easy to use: only four diodes are needed, and it is also fully passive rectifiers that can be used in most situations. However, its power extraction efficiency is very limited. Assuming the voltage drop of each diode is V_D, in the FBR, the current source of the PT will start to charge the Cp first at each half-cycle of the waveform until the voltage on Cp reaches the $V_{RECT} + 2V_D$, the current source start to charge the output capacitor V_{RECT}. Besides, when the direction of the current source is changing, a part of the charge is needed to eliminate the residual charge on the Cp from the last half-cycle. Therefore, a part of the generated charge is wasted, and the shadow part of the current waveform indicates the charge that does not go into the output.

The sinusoidal current of the PT can be expressed as $I_P = I_0 sin(\omega t)$, where $\omega = 2\pi f_P$ and I_o is the amplitude of the generated current, f_P is the frequency of the external force. Then the charge generated in a half period can be expressed as:

$$Q_{total} = \int_0^{\frac{T}{2}} I_0 sin\omega t \, dt = \frac{2I_0}{\omega} \tag{2.4}$$

The open circuit voltage amplitude of the PT can be expressed as:

$$V_{OC} = \frac{Q_{total}}{2C_p} = \frac{I_0}{\omega C_p} \tag{2.5}$$

Since the part of the charge is wasted when the V_{BR} flipping between $V_{RECT}+2V_D$ and $-(V_{RECT}+2V_D)$, the charge transfer to the output capacitor C_{RECT} can be expressed as:

$$\begin{aligned} Q_{FBR} &= Q_{total} - [V_{RECT} + 2V_D + (V_{RECT} + 2V_D)]C_P \\ &= Q_{total} - 2(V_{RECT} + 2V_D)C_P \end{aligned} \tag{2.6}$$

Therefore, the energy transferred to C_{RECT} is:

$$E_{FBR} = V_{RECT}Q_{FBR} = 2C_P V_{RECT}(V_{OC} - V_{RECT} - 2V_D) \tag{2.7}$$

Also, the generated power in a half period is:

$$P_{FBR} = \frac{E_{FBR}}{T/2} = 4C_P V_{RECT} f_P (V_{OC} - V_{RECT} - 2V_D) \tag{2.8}$$

By adjusting the output voltage to make $V_{RECT} = \frac{V_{OC}}{2} - V_D$, the maximum power point (MPP) can be tracked, while the maximum power transferred to C_{RECT} is:

$$P_{FBR,Max} = 4C_P f_P (\frac{V_{OC}}{2} - V_D)^2 \tag{2.9}$$

The voltage drop of diode V_D could be usually much lower than V_{OC} by using some technique such as the active diodes [31]. Hence the V_D can be ignored, and the maximum output power of FBR is:

$$P_{FBR,Max} = C_P f_P V_{OC}^2 \tag{2.10}$$

2.3.2. SSHI circuit

To reduce the charge wasting when the PT's voltage is flipping and increase the power extraction efficiency[32], the synchronized switch harvesting on the inductor (SSHI) rectifier circuit is introduced [30][33][34]. Fig. 2.13 shows the schematic of the SSHI circuit and its simulated voltage and current waveforms. Compared with the FBR, an inductor L_{BF} is added in parallel with the PT, which can form an RLC loop to flip the voltage across the PT, and there is also a switch $M1$ to control the connection of the inductor. Every time when the current of I_p is changing direction, the switch $M1$ will be turned ON with a very short time to flip the voltage across the PT by the current path through the inductor L_{BF}. The switch control signal ϕ_{BF} should be synchronously generated and its pulse-width should be a half period of the RLC system to have better performance.

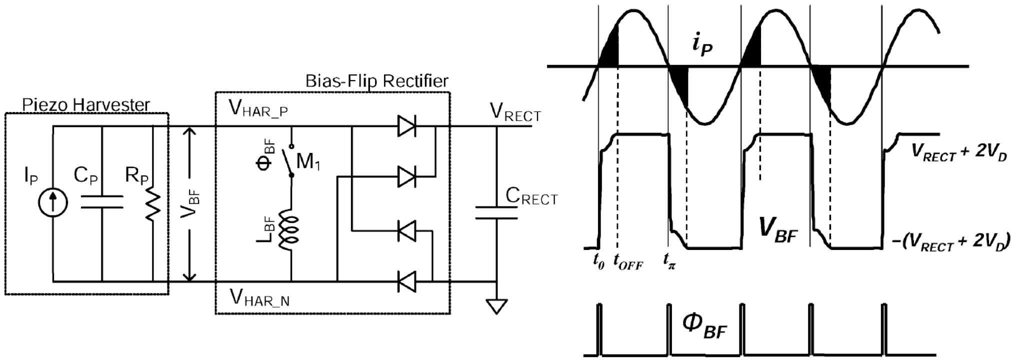

Figure 2.13: The SSHI rectifier circuit with associated simulated voltage and current waveforms. [30]

Due to the damping of the RLC loop, there is still some energy loss during the flipping. Assuming the voltage across PT is V_F after the flipping, it is expressed as:

$$V_F = (V_{RECT} + 2V_D)\eta_{SSHI} \tag{2.11}$$

where η_{SSHI} is defined as the voltage flip efficiency of the SSHI rectifier, which is only dependent on the constants of the RLC loop, and its value is between 0 to 1:

$$\eta_{SSHI} = e^{-\frac{\pi}{\sqrt{\frac{4L}{R^2 C_P}}}} \tag{2.12}$$

With the flip efficiency, the charge transferred into the output capacitor C_{RECT} in a half period is:

$$\begin{aligned} Q_{SSHI} &= Q_{total} - C_P(V_{RECT} + 2V_D - V_F) \\ &= C_P[2V_{OC} - (V_{RECT} + 2V_D)(1 - \eta_{SSHI})] \end{aligned} \tag{2.13}$$

Then the transferred energy is:

$$E_{SSHI} = V_{RECT} Q_{SSHI} = C_P V_{RECT}[2V_{OC} - (V_{RECT} + 2V_D)(1 - \eta_{SSHI})] \tag{2.14}$$

Therefore, the generated power of the SSHI rectifier is:

$$P_{SSHI} = \frac{E_{SSHI}}{T/2} = 2C_P V_{RECT} f_P[2V_{OC} - (V_{RECT} + 2V_D)(1 - \eta_{SSHI})] \tag{2.15}$$

The MPP also can be found when $V_{RECT} = \frac{V_{OC}}{1-\eta_{SSHI}} - V_D$, and the maximum output power is:

$$P_{SSHI,Max} = 2C_P f_P(1 - \eta_{SSHI})(\frac{V_{OC}}{1 - \eta_{SSHI}} - V_D)^2 \tag{2.16}$$

The voltage drop of diode V_D is usually much lower than V_{OC}, and if we ignore it, the maximum output power of the SSHI rectifier is:

$$P_{SSHI,Max} = \frac{2}{1 - \eta_{SSHI}} C_P f_P V_{OC}^2 \tag{2.17}$$

Compared the result of FBR, we have:

$$\frac{P_{SSHI}}{P_{FBR,VD}} = \frac{2}{1 - \eta_{SSHI}} \tag{2.18}$$

In the real circuit, with a few millihenry inductors, more than 80% of the voltage flip efficiency η_{SSHI} can be achieved, and the output power of the SSHI is more than 10x than the FBR. Therefore, the SSHI rectifier has much better power extraction efficiency than the FBR.

2.4. Conclusion

The introductions to the related theories and previous works in this chapter provide a lot of help to design the piezoelectric energy harvesting roller. Firstly, by showing the principle behind piezoelectricity, the energy harvester can be designed by fully making use of the piezoelectric effect. Secondly, the discussion about the widely used piezoelectric materials highlights the main properties of these materials, which is useful when selecting the material in the Sensor Roller. Thirdly, some previous works are presented in this chapter, and these ideas are illuminating to design the harvester in this project. Finally, the different types of piezoelectric energy harvesting rectifiers are also introduced, some of these circuits could be used in the Sensor Roller to rectify the generated voltage.

3

Harvester design

In this chapter, the design of the piezoelectric energy harvester in the bore of the roller is introduced. This chapter is mainly focused on the physical domain design of the energy harvester system, as the electric part, which will present in the next chapter. The workflow of the design process is presented at the beginning of this chapter. Following the workflow, the details of the harvester design are carefully shown, including the results of the simulations and tests. By the end, the conclusion of this chapter is discussed at the end of this chapter.

3.1. Workflow

The workflow of the harvester design is shown in Fig. 3.1. The process of the harvester design can be divided into two stages: stage one is from the beginning to the test of the first prototype, while another stage starts with the second prototype design till the end.

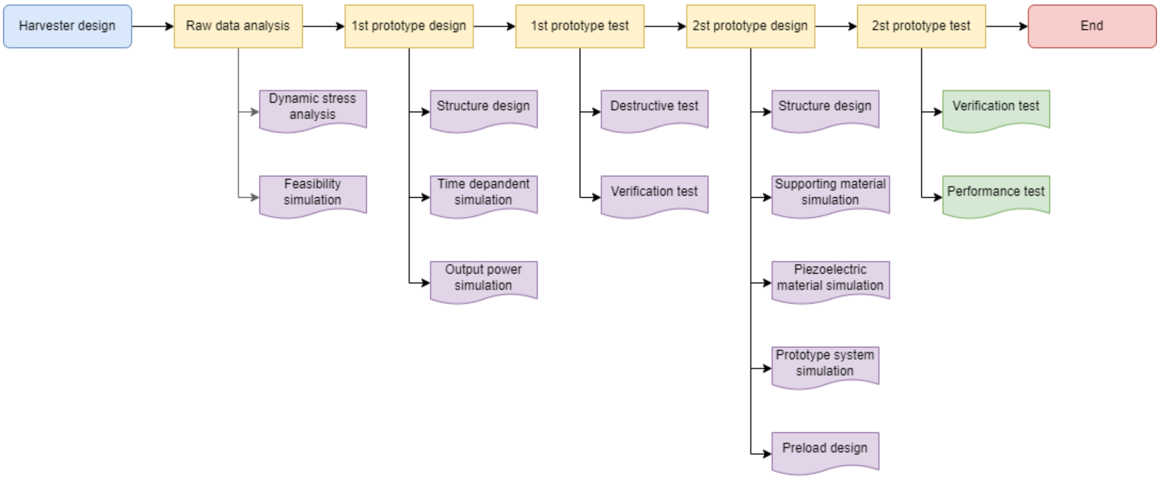

Figure 3.1: Workflow chart of the harvester design.

In Fig. 3.1, the yellow rectangles represent the main steps of the harvester design, and each of them is introduced in a single section. Below these steps, there are the sub-tasks of the steps. The purple sub-tasks represent the finished tasks, which results are shown in this chapter, while the green sub-tasks represent the planned tasks to finish in the future.

3.2. Overview of the target roller

To start the analysis and modeling of the roller, an overview of the target roller is necessary to be introduced, including the what is its geometry and how it moves in the bearing. A photo of the target roller is shown in Fig. 3.2. It is a cylindrical roller used in the single roller bearing of SKF [35], and there is a cylindrical bore inside the roller. The bore is the place to put the energy harvest system and smart sensors. According to the drawing of the roller, the cylindrical bore has a height of $83.2mm$ and a diameter of $21mm$.

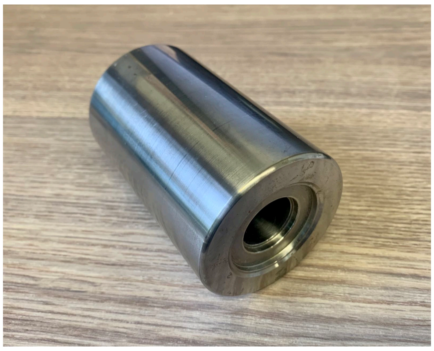

Figure 3.2: The target roller provided by SKF.

Fig. 3.3 shows a sectional view of the cylindrical roller bearing, and there are some cylindrical rollers located between the housing seat (outer raceway) and the shaft seat (inner raceway). The target bearing is under a pure radial load, in other words, the radial force to the roller keeps the same when the bearing is rotating. When the bearing shaft is rotating, the roller will also be spinning due to the friction on the contact line with the roller. The rotational speed of the target roller is 120 rpm, therefore, the radial force to the roller has the frequency of $2Hz$.

Figure 3.3: Cylindrical roller bearing of SKF.

In conclusion, based on the movement of the roller and the bearing, the stress profile on the roller can be roughly estimated. First of all, there are two stresses towards the roller, and they are equal in magnitude, however opposite in direction, and located at the two contact lines between the roller and the bearing rings. Besides, due to the rotation of the roller, the two stresses will also rotate around the roller at $2Hz$, but the amplitude of the stress will keep the same during the rotation.

3.3. Raw data analysis

After qualitatively understanding the movement and stress of the roller, quantificationally analyzing those physical quantities is necessary to determine the feasibility of the project. The analysis begins with the raw data of the roller provided by SKF.

3.3.1. Raw data from the SKF

There are nine RPT files [36] provided by SKF as the input raw data for our analysis. Three of the nine files are one group, which includes one type of information: strain, stress, and deformation of the roller.

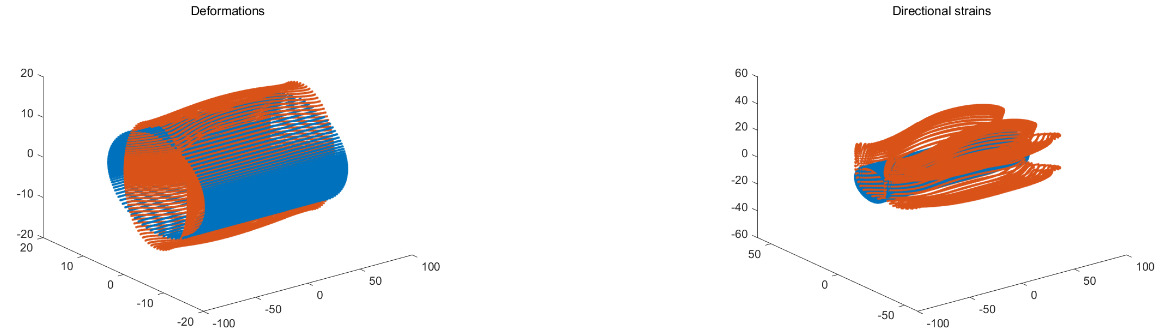

(a) Deformation of the bore.

(b) Strain of the bore.

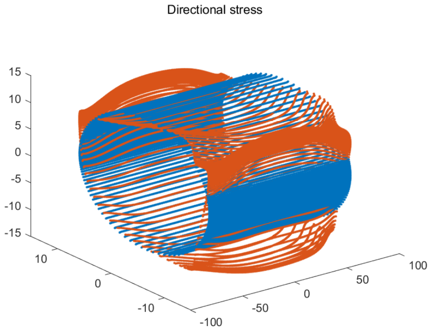

(c) Stress of the bore.

Figure 3.4: Raw data plots with MATLAB.

These data are collected with the Sensor Roller of the SKF during the real working condition, hence, these data are closed to the real case and useful for us when building the model.

However, the raw data cannot be directly used in modeling. It is needed to extract the useful data first and process it to get the helpful information. Open one of the files and the information can be found:

- Text information, such as the name of the report, and time of the collection.
- Setting of the measurement, such as the step time and variable of the measurement.
- The original coordinates of the roller with X, Y, and Z axis and its node ID.
- The coordinates after deformation of the roller with X, Y, and Z axis and its node ID.
- The value of the measurement variable associated with the node ID.

By observing the information, a 3D model of the roller can be built with the coordinates, and the variable of the measurement, such as strain and stress, also can be shown at the related location of the roller. With the help of MATLAB [37], a script was written to extract and combine the measurement information and plot it in a 3D figure.

In Fig. 3.4, the results of the 3D plots are shown with three important variables: deformation (a), strain (b), and stress (c). There are many dots with two colors in these figures, and blue dots show the original coordinates of the bore's position, while the red dots show the measurement variables associated with its coordinates. These results are scaled with a suitable value to be easier to observe, and due to confidentiality only relative values are shown.

With these figures, a basic understanding of the loading situations of the roller can be obtained. For example, it can be found that the maximum of the radical deformation is around $15um$, and a basic distribution of the stress is also observable. However, if want to make a quantificationally analysis, the data should be further processed.

3.3.2. Dynamic stress analysis

In the last part, the figure of some important physical variables is obtained with the related coordinates. But these figures only show the value of the physical variables at a certain dot, the dynamic stress analysis on a certain area is more helpful for future modeling.

Before making the dynamic stress analysis, it can be known that the piezoelectric material in the bore of the tube should be divided into several segments. This is because if put a whole symmetric piezoelectric material in the bore, the resultant force the piezoelectric material received is approximately zero during the rotation, hence, due to the law of charge conservation, the sum of the generated charges (positive charge and negative charge) on the whole material also should be zero.

Therefore, as shown in Fig. 3.5, the piezoelectric materials are cut into four and eight segments. In this situation, when the roller is rotating, the resultant force on each of the segments will not be zero, and the energy can be harvested from this unbalanced force distribution.

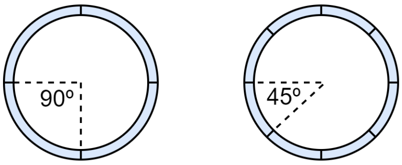

Figure 3.5: Divided the piezoelectric tube into several segments.

After that, a dynamic stress analysis of the average stress on each segment can be done by processing the raw data. Here are the steps of the data process:

1. Calculate the average pressure in the direction of the cylinder's height.
2. Originating from the center of the cylinder, turn the Cartesian coordinate system into the polar coordinate system.
3. Calculate the average pressure on every 5 degrees of the polar coordinate.
4. Calculate the average pressure on a single segment (90 degrees and 45 degrees) of the piezoelectric material.
5. Combined with the rotational speed, the stress-time graphs of the two segment situations are obtained.

The result of the dynamic stress analysis shows in Fig. 3.6, while the blue line represents the four-segments situation and the red line represents the eight-segments situation.

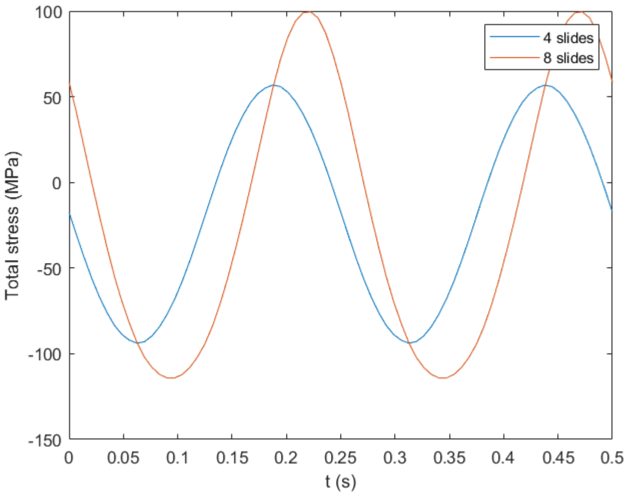

Figure 3.6: Stress-time graphs of the four and eight segments situation.

This figure shows that the dynamic stresses in both the two situations are nearly the sinusoidal waves with a positive offset, and both of their frequency is 4 Hz. Besides, it can be observed that in the eight-segment situation, the peak-peak average stress on each segment is 213.7 MPa, which is higher than the four-segment situation that the peak-peak average stress is 150.6 MPa.

3.3.3. Introduction to COMSOL

After the data analysis, the input of the simulation is already prepared. Then the modeling software is needed to simulate the piezoelectricity of the energy harvester. In this project, COMSOL Multiphysics (Version 5.3a) [38] is used to make the simulation.

COMSOL Multiphysics is widely used to simulate the coupled multiphysics situation. In this project, the mechanical domain and the electric domain is coupled through the piezoelectricity, therefore it is suitable to use COMSOL to make the simulation.

Based on the finite element method, COMSOL provides a complete simulation platform for multiphysics modeling, and accurate experimental results can be simulated, which are useful for designing the energy harvested. Here is the general workflow of the COMSOL modeling [39]:

1. Selecting the target physics domains and the type of the study, such as stationary study or frequency domain study.
2. Building the geometry of the simulation target or importing the geometry from the CAD files.
3. Defining the material of the geometry, which includes the properties of the material, such as density, Poisson's ration, and Young's modulus.
4. Setting the initial condition and the boundary condition of the system.
5. Meshing the geometry into finite elements.
6. Selecting the outputs of the simulation, such as 2D plots and tables of results.

Following the steps above, the numerical solution will be obtained by COMSOL. This solution is accurate enough to help the feasibility study of the project and is also useful to the structure design of the energy harvester. In the next sections, the two generations of the modeling works will be present based on the general workflow of COMSOL.

3.3.4. Feasibility simulation

Before designing the energy harvester prototype, a feasibility simulation is made with COMSOL to roughly check the possibility of the project. This feasibility simulation is helpful to find the direction of the prototype structure design and also useful to have a rough concept of the output power level of the energy harvester roller.

Modeling

Fig. 3.7 shows the designed geometry of the feasibility simulation in COMSOL. The structure of the geometry is simple: a steel hollow cylinder represents the target roller, and inside the bore of the roller, a tube with four 90-degree segments is attached to the inner surface of the bore, and the material of the tube is PZT-5A, a common PZT ceramic material. As for the size of the geometry, the roller's size is chosen as the real target roller, and the thickness of the piezoelectric material is set as $1mm$.

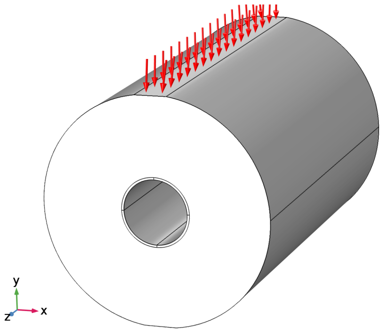

Figure 3.7: Geometry of the feasibility simulation.

The next step is to set the boundary condition of the roller. The boundary condition for this feasibility simulation is simple: the red arrows represent the applied force on the roller to simulate real working conditions in the bearing. The bottom of the roller is fixed to support the structure. The amplitude of the applied force is based on the previous study of SKF, and a rotation parameter is defined to simulate the rotation of the roller.

In addition to the geometry of the harvester, the coordinate system of the second prototype also should be redefined to fit the tube shape piezoelectric material. As shown in Fig. 3.8, different from the 3D Cartesian coordinate system, the new coordinate system is defined in that the Z axis (the blue one) is perpendicular to the surface of the piezoelectric material. Therefore, it is easy to use the new coordinate system to describe the polarization of the piezoelectric material, and the results are much closer to reality.

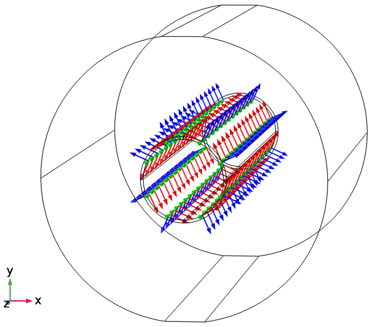

Figure 3.8: The coordinate system for the tube piezoelectric material.

In COMSOL, this new coordinate system can be made by defining the three vectors in the basic base vector system as follows:

$$x1 = \begin{bmatrix} -sin(atan2(y,x)) \\ cos(atan2(y,x)) \\ 0 \end{bmatrix} \quad x2 = \begin{bmatrix} 0 \\ 0 \\ 1 \end{bmatrix} \quad x3 = \begin{bmatrix} -sin(atan2(y,x)) \\ cos(atan2(y,x)) \\ 0 \end{bmatrix} \tag{3.1}$$

Finally, the stationary study is selected in this feasibility simulation to find out the generated electric potential on the piezoelectric material.

Results and discussion

Fig. 3.9 shows the generated electric potential distribution on the piezoelectric material when the loading force is at the nominal value. The direction of the applied force is along the y axis in the figure. The graphical result shows that the maximum generated electric potential is higher than $600V$, even under the minimum loading force. Besides, the electric potential distribution shows a high level of symmetry. The highest positive electric potential area is at the top and bottom of the piezoelectric tube, while the lowest negative electric potential area is located at the left and right parts of the tube.

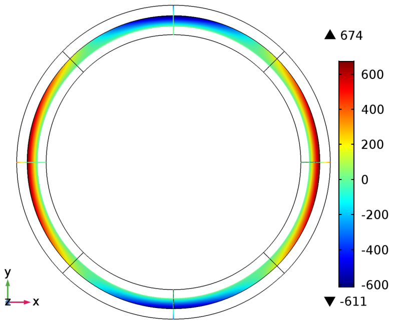

Figure 3.9: Electric potential distribution with nominal applied force.

The symmetrical electric potential distribution also shows in Fig. 3.10. This figure plots the generated electric potential along the arc length of the four divided segments. The locations of these four segments are shown in the figure, which is related to the locations in Fig. 3.9.

Finally, a sweep simulation is made as the result shown in Fig. 3.11. This figure shows the volume maximum electric potential on the top and left segments when the applied is changing from minimum

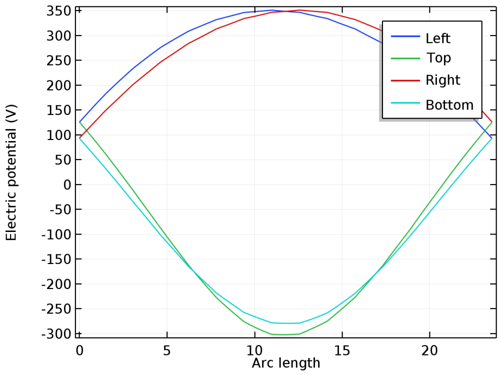

Figure 3.10: Electric potential distribution on each segment with nominal applied force.

to maximum. It shows the linear relationship between the volume maximum electric potential and the applied force.

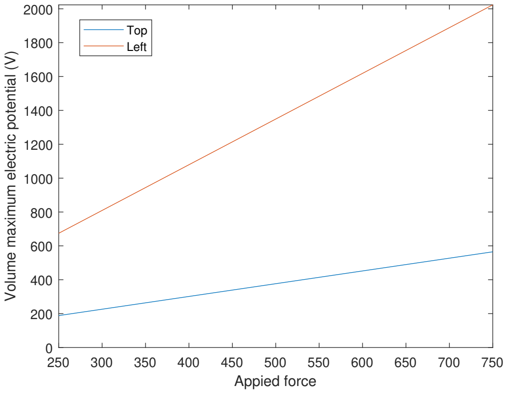

Figure 3.11: Volume maximum electric potential with the applied force from minimum to maximum.

In conclusion, the results of the feasibility simulation show that the project has a very high probability of success since the generated electric potential is high enough to power the loading devices in the smart roller. With the equation (2.10), since the frequency of the loading force is $4Hz$, and assuming the capacitance of the piezoelectric device is $10nF$ when the open circuit voltage is equal to $400V$, which is very possible according to the simulation, then the output power can be calculated, which is $6.4mW$. The conservative output power estimation indicates that even with a simple FBR, the energy harvester has a very strong potential to meet the $5mW$ power requirement of the project.

However, the feasibility simulation is too simple to reflect the situation in the real world. Many details of the real harvester are not considered. For example, the very high electric potential possibly damages the electric circuit, and the piezoelectric device could be crashed under this high loading force. Therefore, further simulations and tests are necessary to manage the risks.

3.4. First prototype design

After the feasibility simulation, the first prototype is ready to start the design. First of all, the structure of the first prototype needs to be settled. Then based on the structure, some simulations should be made to check its performance. Besides, the output power is also can be simulated with the rectifier circuit. In this section, these steps above are introduced.

3.4.1. Structure design

The purpose of the first prototype design is not to finish the final design of the energy harvest roller but focus on the relationship between the loading stress and the generated voltage, and the physical properties of the piezoelectric material.

On the one hand, the structure of the first prototype should be close to the real situation, in order to provide enough information to help to design the second prototype. On the other hand, the first prototype structure better not be too complex, because a complex structure will take a lot of time to simulate and test.

Therefore, a simple structure is designed with COMSOL geometry function, as shown in Fig. 3.12.

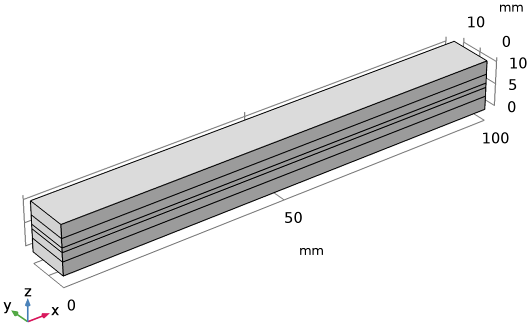

Figure 3.12: The structure of the first prototype.

The structure is like a ”sandwich”, and it contains five layers. In the middle, it is the piezoelectric material layer, and in the simulation, one of the most popular piezoelectric materials in energy harvesting is selected: the PZT ceramic. Above and below the piezoelectric material, two supporting layers are designed to protect the piezoelectric material, this is because the piezoelectric material, such as PZT ceramic, is extremely fragile. The two supporting layers help the loading force more evenly distribute on the piezoelectric material layer. Besides, by changing the material of the supporting layers, the applied stress on the piezoelectric material layer can be adjusted. Finally, at the top and bottom of the ”sandwich” structure, two metal layers are designed to simulate the real situation when the harvester is embedded in the metal roller.

The size of the structure also needs to be carefully considered. Firstly, for the piezoelectric layer, considering the cost and time, it is wise to purchase the piezoelectric material product on the market. Therefore, in the modeling, it is better to make the size of the piezoelectric material layer close to the product can be directly purchased. This is also helpful for future testing. Besides, the size of the piezoelectric material is highly related to the final output power of the energy harvester. Generally, the bigger the piezoelectric material is, the higher output power can be achieved. Hence, it is necessary to balance the trade-off between available space in the bore of the roller and the size of the piezoelectric material.

The size of the supporting layer also affects the output power of the harvester because the thickness of the supporting layer is related to the transferred stress on the piezoelectric layer. If the supporting layer is too thick, most of the deformation is absorbed by the elasticity of the supporting layer. Therefore, a sweep simulation of the supporting layer’s thickness is necessary to find the suitable thickness, which not only protects the piezoelectric layer but also transfers enough stress to it. Finally, the size of the top and bottom metal layers is not very important, since the simulations are concentrated on the behavior of the middle three layers.

3.4.2. Time-dependent simulation

Different from the feasibility simulation, the time-dependent simulation will show the generated current on the piezoelectric devices, rather than the electric potential in the stationary study. By making the time-dependent simulation in COMSOL, the terminal current could be obtained, which is more convincing information to calculate the output power of the harvester.

Modeling

Since the main study target of the time-dependent simulation is the relationship between the load force and the current on the piezoelectric material layer, the wild-used PZT-5A is selected as the piezoelectric material. As for the metal layer and supporting layer, they are not concerned in this study, therefore, Aluminum is selected to represent both of these two layers, in order to reduce the influence of these two layers in this simulation. Besides, to make the simulation more realistic, the size of the sandwich structure is selected that can be embedded inside the bore of the roller.

After defining the material and the size of the geometry, the boundary condition should be set to make the simulation. As for this first prototype, the main boundary condition is the boundary load on the top of the metal layer, as shown in Fig. 3.13. In the time-dependent simulation, the boundary condition is set as the pressure value from the results of raw data analysis. Besides, some other basic boundary conditions are needed. For example, the bottom metal layer should be fixed to support the whole harvester, and the ground and the output terminal should be selected for the electrostatics domain in COMSOL.

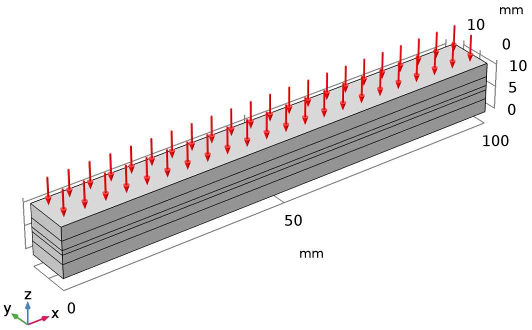

Figure 3.13: The boundary load of the first prototype.

When the boundary conditions are settled, the type of the study should be selected, which determined how will the simulation work. Apparently, the time-dependent study mode is chosen in this simulation and it is helpful since the load applied on the harvester is time-varying in real situations. By making the time-dependent study, the generated voltage and current can be simulated by COMSOL. Also, the change of some variables over time, such as displacement and stress, can be observed by time-dependent study.

The last step before running the simulation is building the mesh for the geometry. A suitable mesh helps the simulation run fast and makes more accurate results. Finding a suitable mesh means the correct element types and sizes of the finite element method should be chosen, based on the characteristics of the target geometry and physical behaviors. In COMSOL, some different element types to build the mesh, as shown in Fig. 3.14, and from left to right are the tetrahedron, hexahedron, triangular prism, and pyramid.

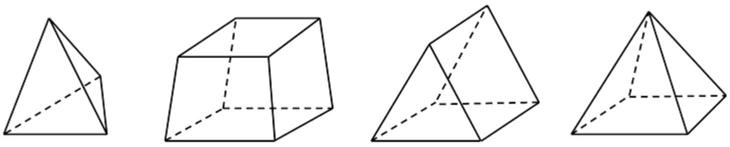

Figure 3.14: Mesh elements in COMSOL. Image source: [40]

The mesh built for the first prototype is shown in Fig. 3.15. Considering the simple ”sandwich” structure of the geometry and the vertical boundary load from the top, the swept mesh tool in COMSOL is used to mesh the geometry into small hexahedron elements to make the simulation. The element size of the mesh can be adjusted to satisfy the tolerance requirement of the results.

Results and discussion

Fig. 3.16 shows the results of the time-dependent simulation: the generated terminal charge vs time (a), then by using the equation:

$$I = \frac{dQ}{dt} \tag{3.2}$$

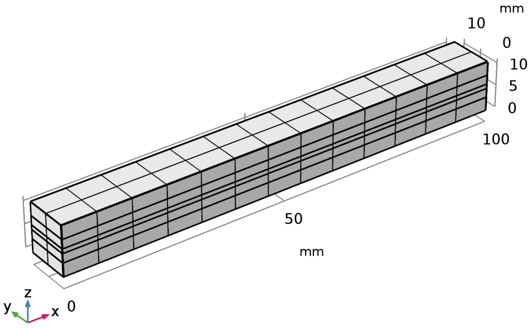

Figure 3.15: The mesh of the first prototype.

the generated terminal current vs time (b) waveform is obtained.

The results show that the generated current is close to a sinusoidal wave, as same as the input stress waveform as shown in 3.6. These results are expected since the feasibility simulation discovered the linear relationship between applied force on the piezoelectric material and the generated eclectic potential. Besides, the amplitude of the generated terminal current is around $180uA$, which is good news since it is a high generated current compared with other piezoelectric energy harvesters.

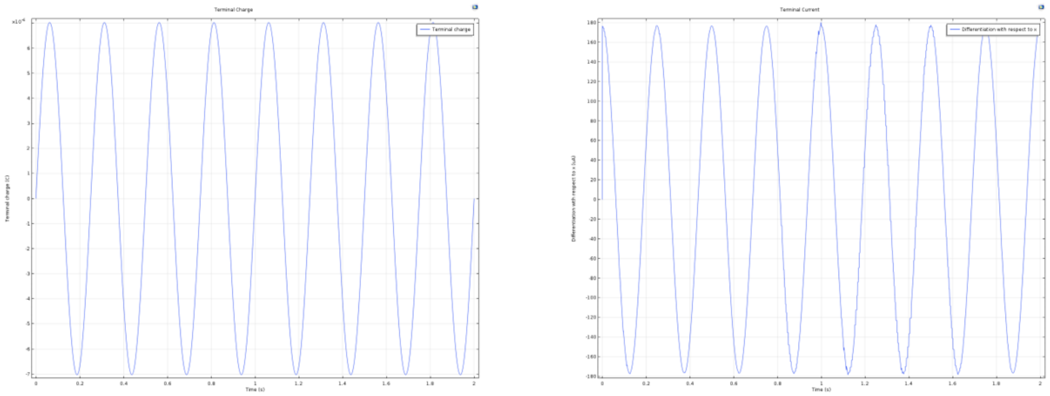

(a) Terminal charge vs time.

(b) Terminal current vs time.

Figure 3.16: Results of the time-dependent simulation

3.4.3. Output power simulation

With the results of generated terminal current, a precise output power simulation can be done with the help of the Simulation Program with Integrated Circuit Emphasis (SPICE).

Method

To simulate the generated output power, in addition to the generated current waveform, the capacitance of the piezoelectric plate and a rectifier circuit designed in the SPICE are needed.

The capacitance of the piezoelectric plate can be calculated by the equation of the parallel-plate capacitor:

$$C_P = \varepsilon_P \varepsilon_0 \frac{A}{t} \tag{3.3}$$

where ε_P is the permittivity of the piezoelectric material, for PZT-5A, the $\varepsilon_P = 826.6$. ε_0 is the permittivity of free space, and A, t represent the area and thickness of the piezoelectric plate respectively.

Then a simple FBR circuit is designed in Cadence Virtuoso [41] to make the output power simulation, as shown in 3.17.

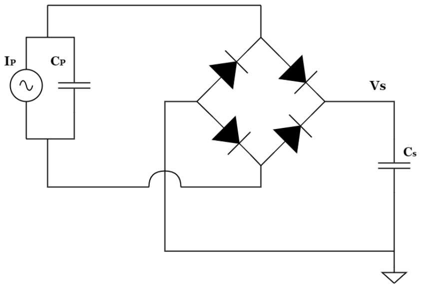

Figure 3.17: FBR circuit for output power simulation.

In this circuit, the current source I_P is designed to generate the current waveform, which is obtained from the COMSOL simulation. C_P represents the inner capacitance of the piezoelectric place, whose capacitance is calculated with the real parameters. Four analog diodes are used to form the FBR, and the voltage drop V_D of the didoes is $0.5V$. Finally, the loading capacitance C_S is used to collect the generated charge pass through the FBR.

By running the time-dependent simulation in Virtuoso, the voltage waveform V_S on the loading capacitance is obtained. Then by using the following equations, the output power can be precisely calculated:

$$E = \frac{1}{2} C_S V_S^2 \tag{3.4}$$

$$P = \frac{\Delta E}{\Delta t} \tag{3.5}$$

Results and discussion

Fig. 3.18 shows the final results of the output power simulation. Two situations are presented: Four segments situation (a) means the whole piezoelectric tube in the bore of the roller is divided into four segments, and eight segments situation is the tube divided into eight segments. The difference between these two situation influence the area of the piezoelectric plate and the applied stress on it.

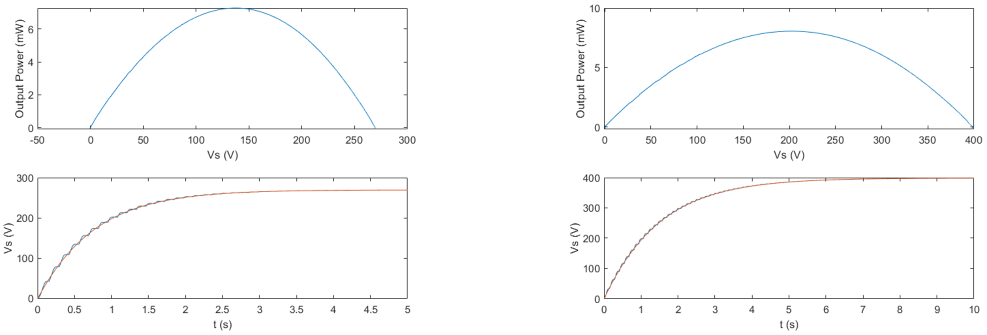

(a) Four segments situation.

(b) Eight segments situation.

Figure 3.18: Output power and voltage

In Fig. 3.18, the lower figures show the waveform of the output voltage V_S, and the upper figures show the calculated output power. The blue lines in the lower figures represent the original waveform, while the red lines are the result after the curve fitting. Since the frequency of the generated current is relatively low, a curve fitting is necessary to make the output power curve smooth.

The results show that the maximum output powers of both situations are close, which are both around $13mW$. The maximum output point for the eight segments situation is $195V$, which is higher than the four segments situation of $132V$.

Fig. 3.18 focus on the output of the single segments of these two situations. Therefore, to better compare them, the overall output power is calculated as shown in Table 3.1.

Table 3.1: Results of the output power

	4 segments	8 segments
Single segment capacitance	46.5 nF	23.2 nF
Single segment output power	12.4 mW	13.3 mW
Maximum output point	132 V	195 V
Total output power	49.6 mW	106.4 mW

The final results show that the eight segments situation achieves about double the output power that the four segments situation, although it has a higher maximum output point. Since both of the situations meet the $5mW$ power requirement, the four segments situation is also a possible solution, since it has a low complexity on the aspect of the rectifier circuit.

3.5. First prototype test

To make the results more reliable, some tests with the real piezoelectric material are necessary. Real testing results are helpful to observe the behavior of the piezoelectric material under the real load, and it is also useful to find the challenges and opportunities in harvester design. In this section, the process of testing for the first prototype will be introduced.

3.5.1. Preparations and settings

To verify the simulation results of the first prototype, the testing piezoelectric material should be similar to the piezoelectric layer in the ”sandwich” structure. Therefore, two kinds of piezoelectric plates were purchased from the STEINER & MARTINS [42] to make the testing, as shown in Fig. 3.19. They have different sizes and thicknesses, and the total generated power of the whole harvester can be estimated by scaling the sizes. Besides, the material of the big plate is PZT-5H, and the material of the small plate is PZT-8. They are all PZT ceramic, and the difference between the two materials helps us to figure out the influence of the material in testing.

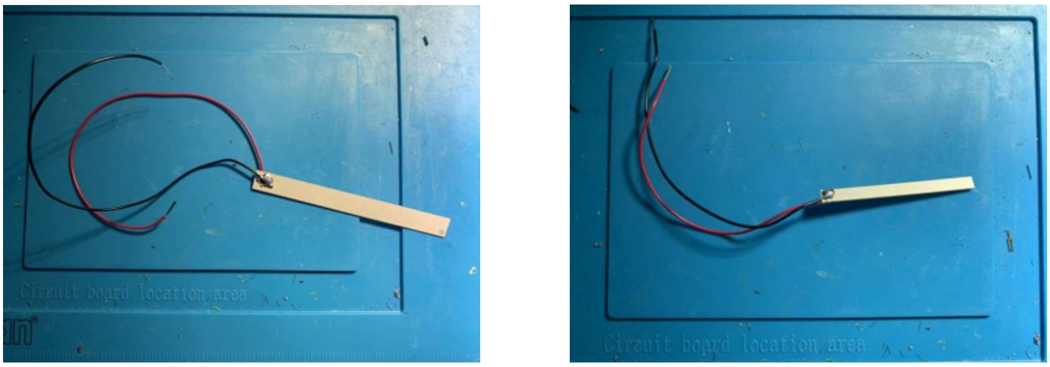

(a) Big plate (90x9x0.5mm).

(b) Small plate (60x5x0.3mm).

Figure 3.19: Piezoelectric plates for the testing

As shown in the figure, both the piezoelectric plate has silver electrodes on the top and bottom surface, and the electrodes are bounded with copper wires by solder, in order to connect with the loading device. After the bounding, the capacitance of the piezoelectric plates should be measured and recorded, this is because the capacitance shows the health of the piezoelectric material and it is also an important constant in the output power estimation.

As in the simulation, vertical load stress should be applied to the top surface of the ”sandwich” structure, therefore, the dynamic testing machine [43] was used in the testing. The dynamic testing machine in this testing is able to provide the loading force with a maximum of $500kN$, which is enough to simulate the real stress condition in the bore of the roller. Besides, the pattern of the loading force is also can be set as the sinusoidal wave with a frequency of $4Hz$ as the real condition.

In addition to the dynamic test machine, a simple FBR circuit was built on a breadboard to rectify the output AC output from the piezoelectric plate. The capacitors with various capacitance were used in the breadboard as the output to store the generated charge. By measuring the change of the stored voltage on the output capacitor, the output power of the piezoelectric plate can be calculated.

As for the measurement equipment, a multimeter and an oscilloscope were used to measure the generated current and voltage signal from the piezoelectric plate as well as the storage voltage on the output capacitor. Same as the simulation, two supporting layers were put above and below the piezoelectric material. Some different materials we used in the test as the supporting layer, such as plastic and robber.

(a) Clamp the piezoelectric plate. **(b)** Connect piezoelectric with a multimeter.

Figure 3.20: Setup for the first testing

Fig. 3.20 shows the setup of this testing. At first, the piezoelectric plate with the supporting layers is clamped with the dynamic test machine (a), and the bounding area is not clamped to connect the wires. Then the two connection wires can be connected to the loading device, for example, they can be connected with the multimeter to measure the open-circuit voltage (b).

3.5.2. Destructive test

Since the piezoelectric ceramic is fragile, a destructive test is necessary to find the maximum stress it can stand. In the previous simulation, the fragile character of the piezoelectric material is not concluded, therefore, the destructive test in the real world is helpful to design the real harvester.

Method

The method of the destructive test is easy. First of all, clamp the piezoelectric plate with the dynamic test machine, start to press the prototype with relatively small stress, and keep the stress for a while. Then open the clamp to check whether the plate is broken by the stress. If the plate is not broken, increase the stress to repeat the test until it is broken.

Results and discussion

During the destructive test, many piezoelectric plates crashed as shown in Fig. 3.21. Consequently, the highest loading force the plate can stand is $2.7kN$, converted to pressure it is $3.75MPa$, considering the effective area of the plate.

This safe stress value is much lower than the used simulation value before, it might be due to some problems with the test set: Firstly, the used support materials are not very flat, and the fluctuation on the contact surface could cause some huge point pressure that crash the plate; secondly, the applied force by the dynamic test machine is not stable and balanced, therefore, the plate might be crashed by the unbalanced force.

3.5.3. Verification test

After the destructive test, the verification test is made to observe some important properties of the piezoelectric material. The verification test concludes many simple experiments and measurements, which are helpful to the next prototype design.

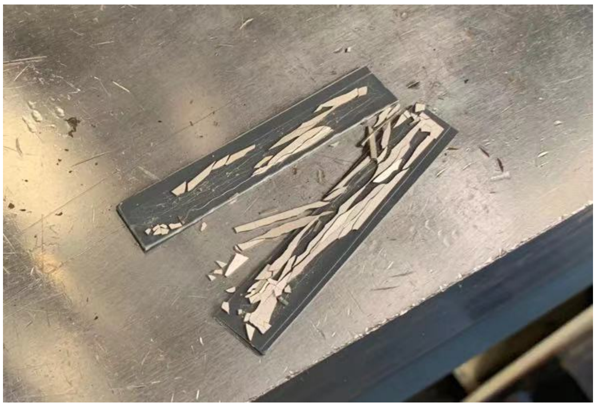

Figure 3.21: Crashed piezoelectric plate.

Method
During the verification test, the following experiments and measurements are made:

Open-circuit measurement:

Apply safe dynamic loading stress to the piezoelectric plate, and connect the plate with a millimeter to measure the range of the generated AC voltage and current. Then according to the measured range, choose the suitable probes to measure and record the AC voltage with the oscilloscope. Increase the amplitude of the loading stress and repeat the test to observe the change of open-circuit voltage.

Output capacitor's voltage measurement:

Connect the piezoelectric plate with the FBR circuit on the breadboard, then measure and record the stored voltage on the output capacitor. Keep record the voltage until the capacitor is fully charged. Then short circuit the capacitor to clear stored charge, and repeat the test with different loading stress and piezoelectric plate.

Study of the supporting material:

Change the type of the supporting material and repeat the destructive test and open-circuit measurement, to observe the influence of different supporting materials.

Study of the depolarization:

Measure the inner capacitance of the piezoelectric plates before and after the testing above, to find out whether the polarization of the plates is damaged by the loading stress.

Results
Fig. 3.22 shows the measurement results which are obtained under the safe stress from the destructive test. Fig. 3.22 (a) shows the open-circuit voltage of the piezoelectric prototype, and the waveform is a sinusoidal wave that fits with the simulation conclusion before. The amplitude of the open circuit is around $70V$, which is possible to meet the power requirement based on the simulation experience before. Fig. 3.22 (b) shows measured single terminal voltage with the breadboard FBR circuit. The results show that the FBR circuit is operating correctly and the output voltage is successfully build-up.

Same as the steps in the output power simulation in the last section, the output power is obtained. In Fig. 3.23 (a), the green line represents the simulated output power of the single piezoelectric plate in the test. The maximum output power is $0.48mW$ when $V_S = 39V$. The output power of a single plate is low, but in the real roller, more than one plate could be planted. Fig. 3.23 (a) also shows the total output power with the different piezoelectric material cover areas. The result shows that with a more than around 80% piezoelectric material cover area, the harvester will achieve the output power goal of $5mW$.

In addition, as mentioned before, the SSHI rectifier will significantly increase the output power of the piezoelectric energy harvester. As shown in Fig. 3.23 (b), even using an SSHI rectifier with just 40% flip efficiency, the output power is much higher than FBR. More than $15mW$ output power could be easily achieved by using the SSHI rectifier.

Furthermore, the study of the supporting material shows that the supporting material has an obvious influence on the performance of the piezoelectric plate. For example, a soft rubber will reduce the open-circuit voltage more than hard plastic. Therefore, further simulations about the supporting material are

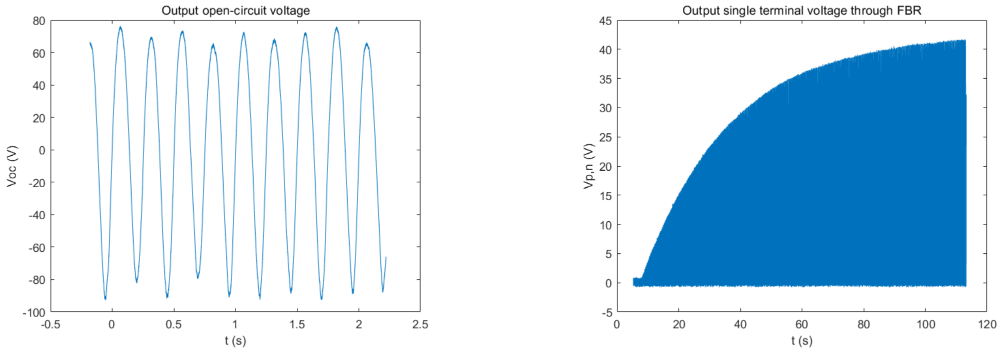

(a) Open-circuit voltage.

(b) Rectified prototype voltage.

Figure 3.22: Measurement results under the 3.75MPa safe stress

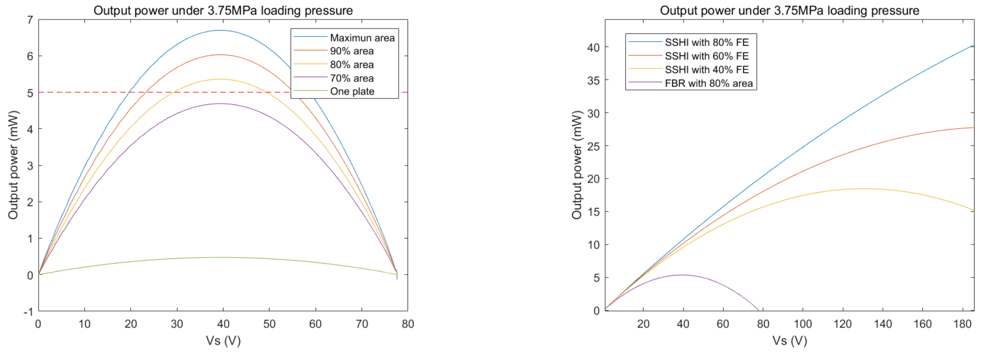

(a) Output power with the different coverage area.

(b) Output power with SSHI rectifier.

Figure 3.23: Results of the output power simulation with 3.75 MPa stress

needed, which will be presented in the next section. Besides, there is no obvious depolarization on the piezoelectric material after the test. Therefore, there is no need to take into account the depolarization in the second prototype design.

3.6. Second prototype design

Based on the experiences and results of the first second prototype, the design of the second prototype is more practical and reasonable. The second prototype design includes some simulations to solve the remaining problems, especially for the material selection of the second prototype. In addition to the simulation above, a system-level simulation and test are also necessary. The system-level simulation and test should be close to the real world, and the final design should be able to have manufactured and tested. Therefore, all the material and parameters in the simulation should be chosen from the real device that can be easily accessed.

3.6.1. Supporting material simulation

In the design of the first prototype, two layers of the supporting material are used to protest the piezoelectric device. However, the influence of the supporting material on the harvester's performance is not clear. In this subsection, the simulation in COMSOL is made to figure out the problem and help to decide what material should be used in the second prototype design.

Method

In the supporting material simulation, the ”sandwich” structure in the first prototype simulation is continually used as shown in Fig. 3.12, because the structure is helpful to study the influence of the supporting material.

Different from the setting before, the boundary condition in the simulation is selected as the displacement rather than the pressure. This is because in the real roller, not all the received pressure can be transferred to the harvester in the bore, but nearly all the displacement will transfer to the inner surface of the bore. By using the displacement as the input physical variable, the simulation output results are more close to the real situation.

The goal of the supporting material simulation is to find a suitable material type with a reasonable thickness. Therefore, four typical plastic materials are chosen: Acrylic, Polycarbonates (PC), ABS, and Polypropylene (PP). They are all easy to manufacture with the shape we want, which is an advantage for the following design. The main difference between these plastic materials is their Yong's modulus.

Yong's modulus is the mechanical parameter to describe the stiffness of the solid material, determined by the formula:

$$E = \frac{\sigma}{\varepsilon} \tag{3.6}$$

where σ is the compressive stress on the material and ε is the related proportional deformation. The unit of Yong's modulus E is usually chosen as gigapascals (GPa). Generally, a harder material has a higher Yong's modulus. Therefore, to study the influence of the supporting material, Yong's modulus of the material is the important parameter that should be simulated.

Another parameter in the supporting material simulation is the thickness of the supporting layer. A too thick supporting material layer might absorb all the stress from the loading force, and a too thin supporting material layer could not protect the piezoelectric plate from crashing. Therefore, a sweep simulation of the thickness of the supporting material is necessary to find out the suitable size.

Results and discussion

Fig. 3.24 shows the results of the supporting material simulation results. The two figures show the simulation results under the $5um$ minimum displacement situation (a) and the $30um$ maximum displacement situation separately. In each figure, there are four curves representing the relationship between the generated average surface pressure with the different thicknesses. The red dash lines in the figures note the safe pressure level from the destructive test, which is $3.75MPa$.

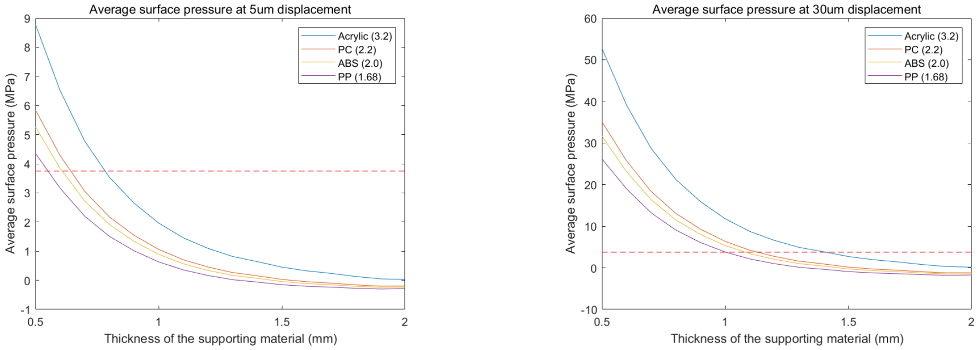

(a) Average surface pressure with 5um displacement.

(b) Output power with SSHI rectifier.

Figure 3.24: Supporting material simulation results.

The results indicate that if the safe pressure level is achieved, what kind of material is needed and how thickness it should be. For example, under the minimum displacement situation, the supporting material should be thinner than $0.5mm$ to make the piezoelectric plate get enough pressure. Under the $30um$ maximum displacement situation, to achieve a safe pressure level, the thickness of these four materials should be between $1mm$ to $1.5mm$.

In a conclusion, ABS plastic is chosen as the material for the supporting layers, because its Yong's modulus is moderate to transfer enough pressure to the piezoelectric layer. Besides, ABS plastic is easy to purchase and manufacture to the wanted shape.

3.6.2. Piezoelectric material simulation

The supporting material simulation helps select the type of the supporting layer, and then a piezoelectric material simulation is made to find the suitable material as the piezoelectric layer.

Method

As mentioned in chapter 2, in addition to the PZT ceramics, the PVDF is also a possible solution as the piezoelectric material in the energy harvesting roller. Compared with the PZT ceramics, the PVDF is much softer, hence by using the PVDF instead of PZT, the problem of crashing could be avoided. Therefore, piezoelectric material simulation is made to check out the possibilities of replacing the PZT ceramics with PVDF material.

For the piezoelectric material simulation, the geometry modeled in the COMSOL is simple. It looks like the ”sandwich” used before, but without the supporting layers since the simulation only focuses on the performance of the piezoelectric material. The boundary condition for this simulation is as same as the supporting material simulation, a displacement is applied to the geometry to simulate the real condition of the roller.

To compare the performance of these two materials, a stationary simulation is made to get the open circuit voltage on the surface of the piezoelectric plate, which can be used to estimate the output power of the harvester.

Results and discussion

Fig. 3.25 shows the generated open-circuit with two different materials under the same $30um$ displacement condition. The results show that the open-circuit voltage of the PVDF is much lower that the PZT-5A. The amplitude of the open-circuit voltage of the PVDF is only $20V$, which is nearly $30\times$ less than the PZT-5A.

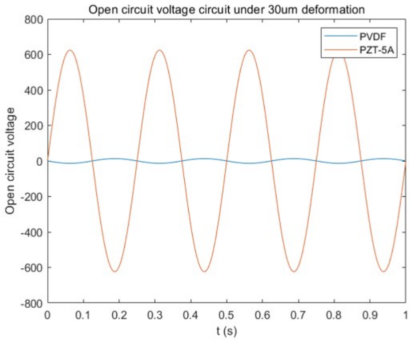

Figure 3.25: Piezoelectric material simulation results.

The significant difference in the generated open-circuit voltage might due to two reasons. Firstly, the piezoelectricity of the PVDF is lower than PZT-5A. The parameter, electrical properties d_33, is used to describe the piezoelectricity of a material. As for PVDF, $d_33 = -28$, and for PZT-5A, $d_33 = 390$. Secondly, the generated electric potential distribution in PVDF is as not linear as the PZT-5A, which is shown in Fig. 3.26. This nonlinear electric potential distribution makes the open-circuit voltage on the two surfaces of the place even less.

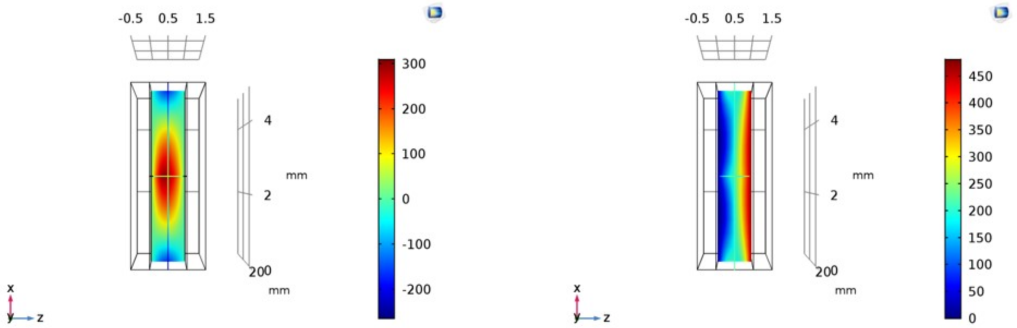

(a) Electric potential of PVDF.

(b) Electric potential of PZT-5A.

Figure 3.26: Generated electric potential distribution.

Combine with the relative permittivity of these two materials, and using the equation (2.10) and (3.3), the output power of the harvester can be estimated as shown in Table 3.2.

Table 3.2: Caparison of the output power

	PZT-5A	PVDF
Relative permittivity	1800	13.5
Capacitance	159nF	1.2nF
Open-circuit voltage	600V	20V
Output power	228mW	1.92uW

As a result, the estimated output power of the PVDF material is much less than the PZT-5A. Therefore, it is not reasonable to use the PVDF to replace the PZT ceramic in the harvester, even though the PVDF has nice flexible and deformable properties. Based on this conclusion, in the further harvester structure design, the protection of the fragile PZT ceramic should be carefully considered.

3.6.3. Structure design

Since the supporting layers and the piezoelectric layer are determined according to the results of the simulations, the next step is designing the structure of the energy harvester.

Different from the first prototype, the second prototype needs to be embedded in the bore of the roller. Therefore, the structure of the second prototype should be a cylinder shape. Besides, the size of the piezoelectric material should be set as the real piezoelectric device that can be directly purchased, because using the piezoelectric devices on the market will save a lot of money and time.

Fig. 3.27 shows the two different structures of the harvester for the second prototype. The left one is the tube structure (a) since a piezoelectric tube is used in this design, while the right one is the polygon structure, in which six piezoelectric plates form a polygon.

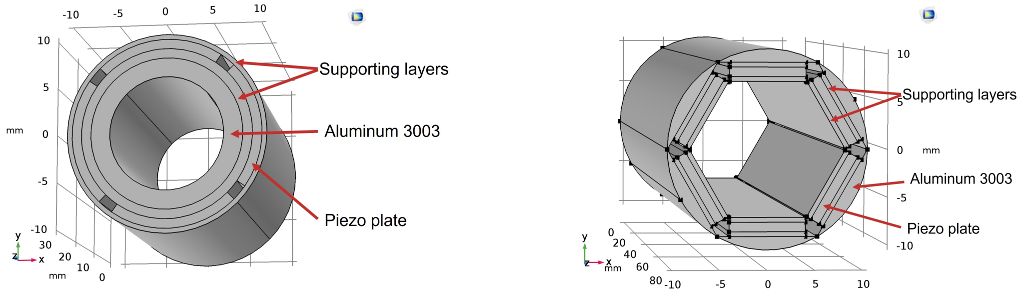

(a) Tube structure.

(b) Polygon structure.

Figure 3.27: Two structures of the harvester.

Both these two structures have four layers, including a piezoelectric material layer, two supporting layers, and a metal layer. As the tube structure, the who piezoelectric tube is cut into segments, and each of the segments is 80 degrees. These segments are covered by two supporting layers, and below the three layers, a metal layer is used to support the whole structure. The piezoelectric material of the tube structure can be purchased that has a length of 30 mm, an outer diameter of 20 mm, and an inner diameter of 18 mm.

The polygon structure takes the idea of the ”sandwich” structure in the first structure. The piezoelectric plate with the supporting layers forms the ”sandwich” structure. To find the cylinder bore of the roller, the sector shape of the metal layer is needed. In the figure, by using six of the ”sandwich” structure, a hexagon will be formed. Other polygons also can be formed, such as pentagons and octagons, depending on the width of the piezoelectric plate. To support the structure from the inside, another metal layer that fit the polygon shape is also needed, in the modeling, the inner metal is omitted.

Both of these two structures are possible to be manufactured and installed in the bore of the roller, and each of them has its own advantages. As for the tube structure, it is easy to assemble since it has fewer components. But the polygon structure is more close to the first prototype design, therefore, the simulation results before are more useful to design the polygon structure.

3.6.4. Prototype structure simulation

To decide which structure will be used in the final design, a system-level simulation is made as shown in this subsection.

Modeling

As shown in Fig. 3.27, the geometry of the tube structure and the polygon structure is made in COMSOL. In addition to the harvester inside the bore, the geometry of the roller is also built to better simulate the real condition, as shown in Fig. 3.28.

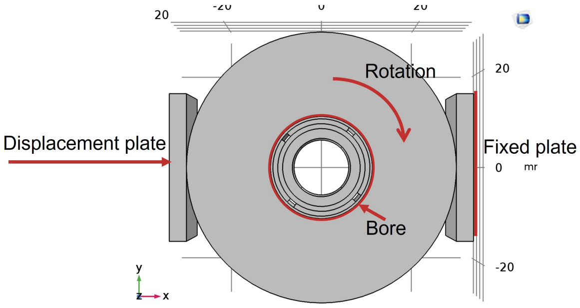

Figure 3.28: The geometry of the whole system.

In Fig. 3.28, a roller is designed with the real parameters of the target roller in Fig. 3.2. In the middle of the roller, the red circle represents the bore, and inside is the designed harvester (the tube structure is used as an example). To simulate the real loading condition, two plates are added: the left one is the displacement plate, which is used to apply the displacement to the roller, while the right one is a fixed plate to support the system. Besides, a rotation variable is added to simulate the change of the deformation's direction in the real roller.

As for the materials, in the second prototype simulation, all the materials are chosen to be the real material in real testing. For example, PZT-5A is selected as the piezoelectric material in the modeling, because the property of the PZT-5A is close to the piezoelectric tube we prepared to purchase. As for the supporting layer, the ABS plastic is used according to the conclusion of the simulation before. For the metal part, since it is not the focus of the study, the high-strength alloy steel is selected from the material library of COMSOL.

The setting of the boundary conditions is not very complex for the second prototype modeling. As shown in Fig. 3.28, a prescribed displacement is applied to the left plate of the system, and the value of the displacement is obtained from the raw data. Then the right plate is set as fixed to support the system. Besides the simulation of the loading displacement, a boundary pressure is applied to the inner surface of the harvest, to figure out the influence of the preload pressure.

In addition, to realize this simulation in COMSOL, the contact pairs should be created, since the roller is in contact with two plates. Before defining the contact pairs, it is necessary to set the geometry as the Form Assembly rather than Form Union. In this way, the two plates are considered as individual parts from the roller by COMSOL, and two contact pairs: a displacement plate with the roller and a fixed plate with the roller are built.

As for the simulation settings, the stationary is selected to study the stress distribution on the piezoelectric material. In the second prototype modeling, the function of parametric sweep in COMSOL is used to observe the change of the stress when some parameters are adjusted, such as the angle of the rotation and the amplitude of the displacement.

Fig. 3.29 (a) shows the mesh of the harvester system. For the second prototype, the default Physics-controlled mesh in COMSOL is used, which is an unstructured tetrahedral mesh. With the mesh statistics function, we can find the average element quality of this mesh is around 0.62, and the minimum element quality is about 0.14. In COMSOL, the mesh element quality should be high than 0.1 to have enough accuracy in the simulation [44]. Therefore, this mesh is accurate enough for the study and also easy to build.

If zoom in to observe the bore of the roller in Fig. 3.29 (b), it can be found that the mesh at that part is much finer than the outer metal since the bore contains many layers with different materials, the finer mesh is helpful to simulate the stress distribution on these layers accurately.

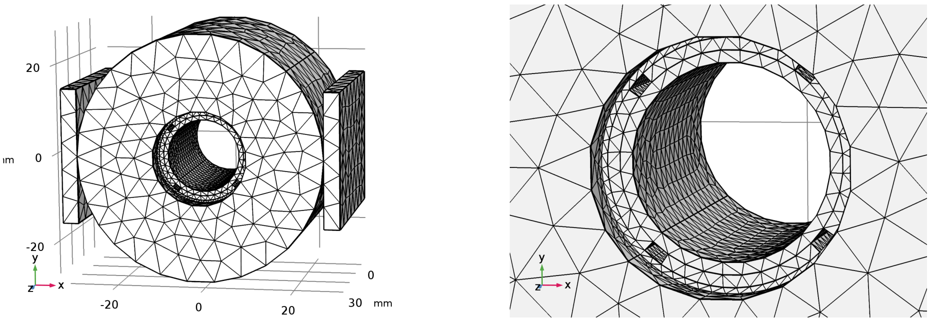

(a) Mesh of the entire system.

(b) Zoom in the bore of the roller.

Figure 3.29: Mesh of the second prototype.

Results and discussion

Fig. 3.30 shows the results of the simulated pressure distribution for the polygon structure. Two typical rotation situations are presented: when the loading is applied in the center of the plate (a) and the edge of the plate (b). As for the center loading situation, the structure works fine. The pressure is balanced and distributed on the plate. However, when the roller rotates, the edge loading situation is made. Under the edge loading situation, most of the pressure concentrated at the edge of the plate could damage the plate.

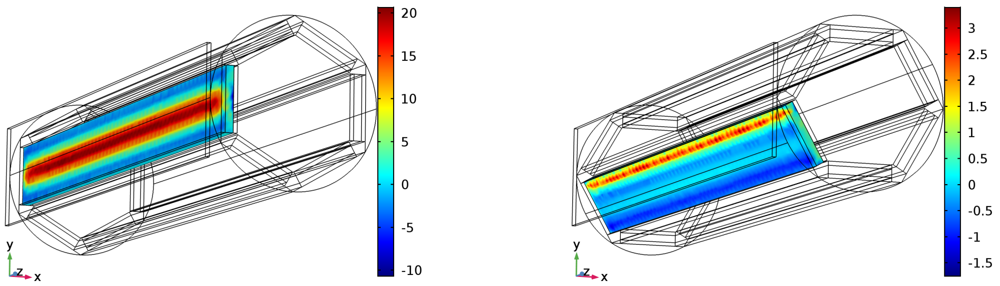

(a) Center loading.

(b) Edge loading.

Figure 3.30: Polygon structure: pressure distribution with 10um displacement (MPa).

This high-pressure concentration might be caused by the form level during the edge loading as shown in Fig. 3.31. Due to the small gap between the two plates, when the loading force is located in the joint of the top metal layer, a physical lever is formed, and it is dangerous to the piezoelectric plates.

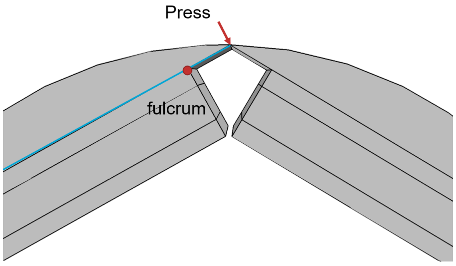

Figure 3.31: The formed lever during the edge loading.

As for the tube structure, the simulation results look better, as shown in Fig. 3.32.

In the tube structure, the pressure distribution shows more balanced on the piezoelectric segments. During the roller's rotation, the value of the pressure is more stable than the polygon structure. There-

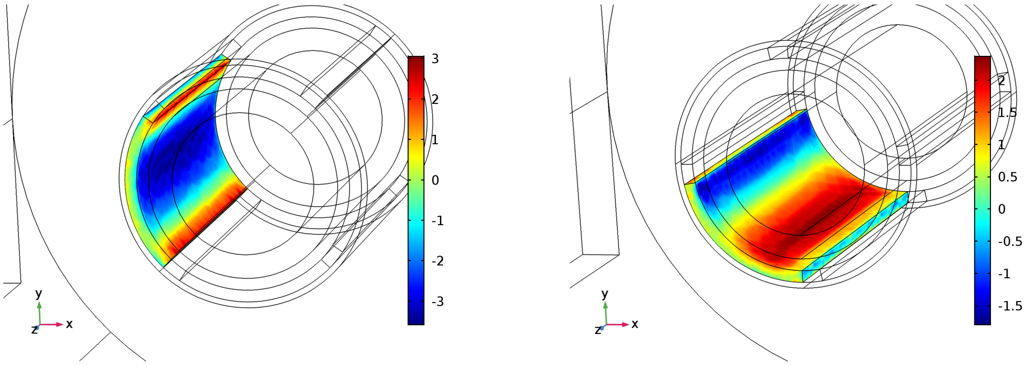

(a) Center loading.

(b) Edge loading.

Figure 3.32: Tube structure: pressure distribution with 10um displacement (MPa).

fore, according to the results of the system level simulation, the tube structure is selected to design the final energy harvester. Compared with the polygon structure, the tube structure is easy to assemble, and the pressure under the working condition is more stable and balanced to protect the piezoelectric devices.

Besides the pressure distribution, the generated electric potential is also simulated as shown in Fig. 3.33. With the minimum $10um$ displacement, around $130V$ open-circuit voltage is achieved, and with the maximum $30um$ displacement, the open-circuit voltage reaches nearly $400V$.

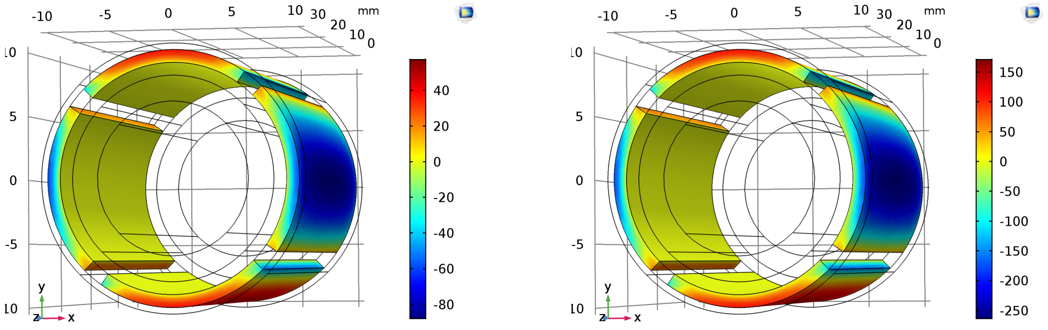

(a) Minimum 10um displacement.

(b) Maximum 30um displacement.

Figure 3.33: Generated electric potential (V).

With the results of the open-circuit voltage, the output power is calculated by equation (2.10) and (2.17), and the results are shown in Table 3.3.

Table 3.3: Estimation of the output power

	Minimum	Maximum
Displacement	10um	30um
Open-circuit voltage	130V	400V
Output power with FBR	2.0mW	19.2mW
Output power with SSHI (50% flip efficiency)	8.1mW	76.8mW

The results show that, with the four piezoelectric segments ($30nF$ capacitance in total), an $8.1mW$ output power is achieved by using the SSHI rectifier, which meets the $5mW$ output power goal of the project. Under the $30um$ maximum displacement, the output power goal is achieved even with a simple FBR.

3.6.5. Preload design

Preload is another important element that should be considered in the energy harvester design. In the proposed tube structure, a preload should be applied to the inner surface of the structure.

There are two main reasons to apply the preload. Firstly, since there are only a few micrometers of displacement that will be generated during the rotating, without any preload, the small displacement will be absorbed by the gaps between these layers. The gaps are inevitable due to the errors of mechanical manufacturing. In some extreme cases, the gaps could be bigger than the generated displacement, the piezoelectric devices cannot get any stress, and there is no generated power. Therefore, a preload will push the layers and reduce the gaps, in order to transfer as much as the displacement to the piezoelectric devices.

Secondly, a preload is also helpful to protect the piezoelectric devices. According to the study of the piezoelectric devices manufacturer, Physik Instrumente GmbH [45], it is suggested to apply a small preload on the piezoelectric ceramics to protect them from crashing by the strong dynamic force.

Applying the preload is not easy, because the size of the harvester is small, and the space inside the harvester should be saved for other components, such as the built-in sensors. Therefore, two structures are designed to apply the preload while not taking too much space. The idea of the first structure comes from the wall anchor, as shown in Fig. 3.34.

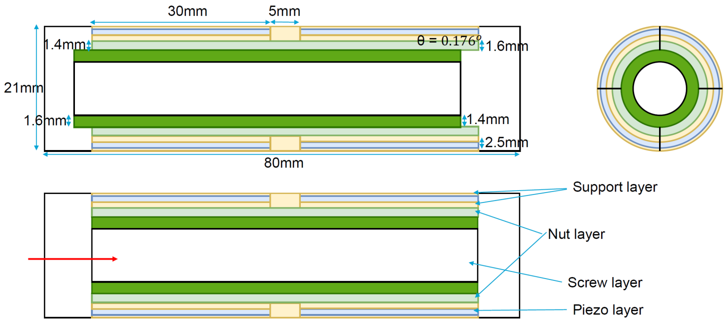

Figure 3.34: Draft of the preload design one: "wall anchor" structure.

As same as the wall anchor, a structure is from by a nut and a screw. Since the screw is designed a little bigger than the nut, when pressing the screw inside the nut, a preload pressure will be generated and transformed to the inner surface of the harvester. By adjusting the sizes of the nut and screw, the pressure level of the preload can be changed to a suitable value.

The idea of the second preload structure is obtained from the piston ring in the engines. As shown in Fig. 3.35, a spring shape piston ring is put inside the harvester. Since the height of the spring is reduced when is stretched, it can be put inside the harvester. Then release the stretching, and a preload is also applied to the inner surface of the harvester.

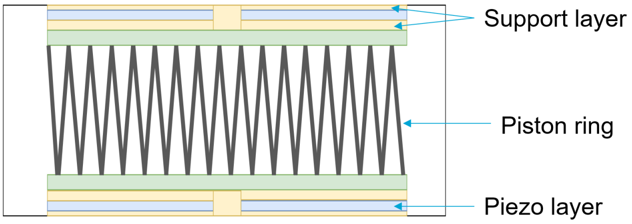

Figure 3.35: Draft of the preload design two: "piston ring" structure.

Since the strength of the preload is dependent on some parameters of the preload structure, such as the sizes and materials, some simulations and tests are necessary to be made in the final harvester design. Due to the time limitation of this project, this part of the work is planned for the future.

3.6.6. Summary

Based on the simulation and discussion before, the second prototype of the energy harvester is designed. Fig. 3.36 shows the rendering of the second energy harvester prototype, made with Solid Edge [46].

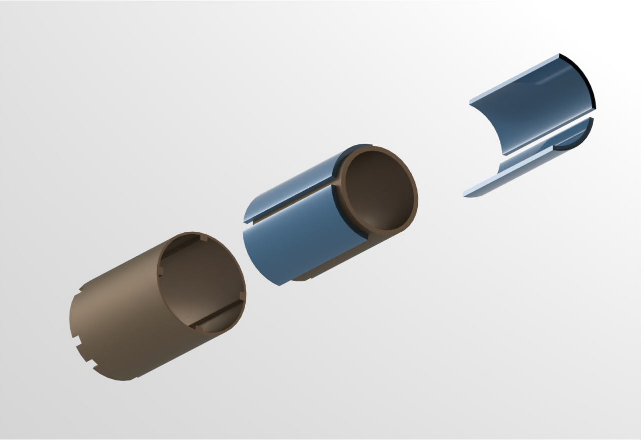

Figure 3.36: Rendering of the second prototype.

The energy harvester is assembled in three-part. The first part is the tube shape of piezoelectric segments, which are blue in the figure. The four piezoelectric segments are cut from a whole piezoelectric tube, and each segment has an 80^o radius, $30mm$ length, and $1mm$ thickness. The other two parts are the inner supporting layer and outer supporting layer, which are made of ABS plastic (brow color). As shown in the figure, the inner surface of the outer layer is not flat, some grooves are designed to better hold the four piezoelectric segments. On one side of the supporting layers, some holes are built as the area for bonding the electrodes of the piezoelectric segments. These supporting layers have the same length as piezoelectric segments, while the inner supporting layer has the $1mm$ thickness and the outer supporting layer has the $0.5mm$ thickness.

Figure 3.37: Rendering of the energy harvesting roller.

Finally, Fig. 3.37 shows the rendering of the energy harvesting roller. Since the available length of the roller is $82mm$, two sets of piezoelectric tubes are put inside the bore of the roller. Therefore, the results of the output power in Table 3.3 are doubled with two sets of piezoelectric tubes.

After putting the piezoelectric tubes, there is still some space for the built-in sensors. This figure only shows the harvester inside the bore, as for the real practical harvesting roller, some components are needed, such as the rectifier circuit and preload device. These extra components will be designed in the future after the tests of the second prototype.

3.7. Second prototype test

To verify the simulation results of the second prototype, some tests are needed. As the plan, there are two groups of testing will be made. Firstly, focusing on the performance of the harvester in Fig. 3.36, a group of verification tests is designed. The goal of the verification tests is to check whether the proposed harvester can generate enough power to meet the $5mW$ output power requirement of the project. Therefore, some questions should be figured out, such as will the piezoelectric segments crash during the test, and how much is the open-circuit voltage.

Secondly, if the verification tests show the harvester performing well, system-level tests are planned to verify the overall performance of the energy harvesting roller in Fig. 3.37. The tests should be made under the real working condition, therefore, the energy harvesting roller will be manufactured and put inside the real bearing to test. Output power and work lifetime are the most important target of the final tests.

Due to the delay of the mechanical manufacture and the limited time of the project, currently, these two groups of testing are still in progress and will be finished in the future. The details of these tests are presented in chapter 5.

3.8. Conclusion

This chapter introduced two generations of the prototype design in detail. As a result, the first prototype design finds the direction of the energy harvest and shows some important properties of the piezoelectric martial. With the help of the first prototype, the second prototype is more closed to the real world. Some critical simulations are made and many key points are settled during the second prototype design.

Consequently, a tube shape harvester is designed that can be put inside the real roller of SKF. According to the simulation, an $8.1mW$ output power is achieved with the SSHI rectifier, which satisfies the output goal of the project. The output power be could much large in the real energy harvesting roller, since more than one set of piezoelectric devices can be put inside the roller, and the input displacement could be large in the real tests, according to the raw data.

Although some components are planned to be designed in the future, these two generations of the prototype design show a great possibility of applying the cutting-edge piezoelectric energy harvesting techniques to the rollers in the bearing.

4

Rectifier design

A well-designed rectifier plays an important role in the performance of the piezoelectric energy harvesting system. On the one hand, the rectifier determines the power extraction efficiency of the energy harvesting system. The less power loss during the rectification, the higher output power will be achieved. On the other hand, the service time of the whole system is also influenced by the rectifier. When the harvester system works in an extreme environment, such as high temperature, the function of the rectifier could be damaged. Therefore, considering the real condition and demand of the energy harvesting roller, several on-chip rectifier circuits are designed with two different materials: the rectifiers with SiC technology to better fit the harsh working environment, and an SSHI rectifier made with $0.18\mu m$ *BCD process to achieve a low open-circuit requirement. The design of these rectifier circuits is introduced in this section, and the results of the simulation and testing of these circuits are also presented.*

4.1. Rectifier circuits with the SiC technology

Considering the high open-circuit voltage is possible in the energy harvester, the silicon carbide (SiC) technology is a great solution compared with conventional silicon technology in the on-chip circuit design. For this project, three SiC on-chip circuits are designed and taped out: the FBR circuit, the passive rectifier circuit, and the SSHI rectifier circuit. The details of these circuits will be presented in this section.

4.1.1. Introduction to the SiC technology

In the past decades, the SiC material absorbed a lot of interest from researchers. According to the report, the market for SiC material will continue to keep growing from 2022 to 2030, especially in the field of electrical and electronics [47].

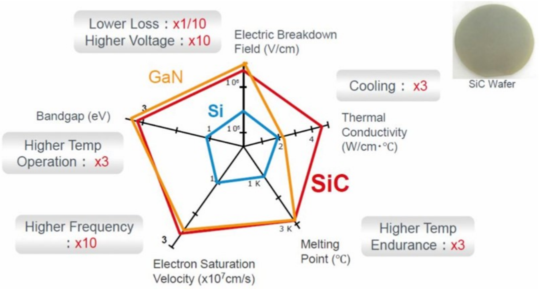

Figure 4.1: Semiconductor Material comparisons. Image source: [48]

Compared with the conventional silicon material, the SiC material has a larger bandgap. For example, the bandgap of 4H-SiC material is 3.2 eV, which is around three times larger than the silicon material (1.1 eV) [49]. The large bandgap provides the SiC material with many nice properties in electronics applications. As shown in Fig. 4.1, compared with a silicon material, the SiC material has a higher operating temperature and a higher voltage tolerance. These two advantages are useful for the project because the working temperature of the roller could be high, and the generated voltage also could be too high to be rectified with a silicon circuit.

For this project, the designed circuits are fabricated based on the 4H-SiC CMOS technology, provided by the Fraunhofer Institute for Integrated Systems and Devices Technology (IISB), based in Erlangen, Germany[50]. Since the Verilog-A SPICE compact model is provided, the n-MOSFETs and p-MOSFETS of the SiC technology can be imported to the library of the Cadence, and the process of the schematic design is as convenient as the silicon technology.

4.1.2. FBR circuit with the SiC technology

As the simplest rectifier circuit, the on-chip FBR circuit is designed for the energy harvester, as shown in Fig. 4.2. In the circuit, four diodes are formed as the full bridge rectifier, which is designed on the SiC chip. The PT in the circuit represents the power transducer, which is the piezoelectric energy harvest device in this project. A capacitor C_s is used to collect the generated charge as the output.

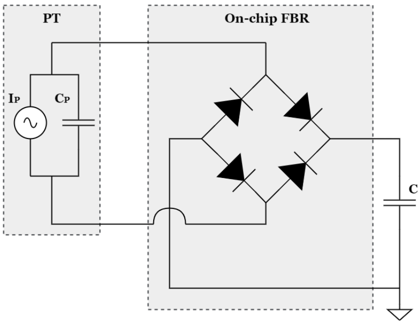

Figure 4.2: Proposed on-chip FBR circuit.

However, this is no diode model in the IISB CMOS library, hence, the diode-connected PMOS is proposed to replace the diode, whose drain, gate, and bulk are connected together as shown in Fig. 4.3. The diode-connected PMOS has a similar behavior as the two terminal diodes, and in conventional silicon technology, the cut-in voltage of the diode-connected is around one threshold voltage, while the forward voltage drop is about two times the threshold voltage [51].

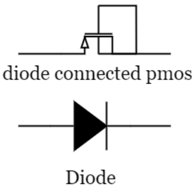

Figure 4.3: Diode connected PMOS.

The design of the FBR circuit is sent to IISB, and Fig. 4.4 shows the proposed layout of the FBR circuit.

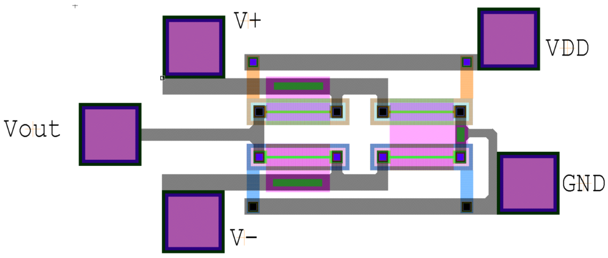

Figure 4.4: Proposed layout diagram of FBR.

4.1.3. Passive rectifier circuit with the SiC technology

An alternative rectifier circuit is designed, as shown in Fig. 4.5. This is a passive rectifier since only a passive device is used, and the structure of this rectifier is called Negative Voltage Converter (NVC) [52].

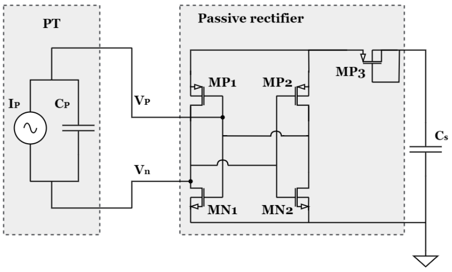

Figure 4.5: Proposed passive rectifier circuit.

This NVC is formed with two nMOS and two pMOS. When V_p is positive and V_n is negative, the nMOS, MN1, and the pMOS, MP2, will be turned on, and they provide a current path for PT to the output capacitor. At the same time, MP1 and MN2 are trued off, therefore, the reverse leakage current is effectively reduced. Another pMOS, MP3, is diode connected to reduce the leakage current from C_s. These five transistors are designed on a SiC chip as same as the FBR circuit. The proposed layout of the passive rectifier circuit is shown in Fig. 4.6.

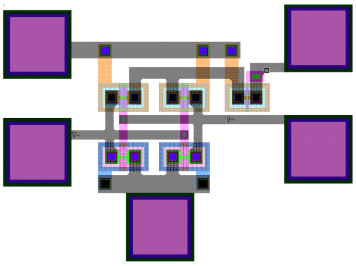

Figure 4.6: Proposed layout diagram of the passive rectifier.

4.1.4. SSHI rectifier circuit with the SiC technology

As mentioned before, compared with FBR, the power transfer efficiency of the SSHI rectifier circuit is much higher. Therefore, to have a better rectifier performance, an SSHI circuit is also proposed.

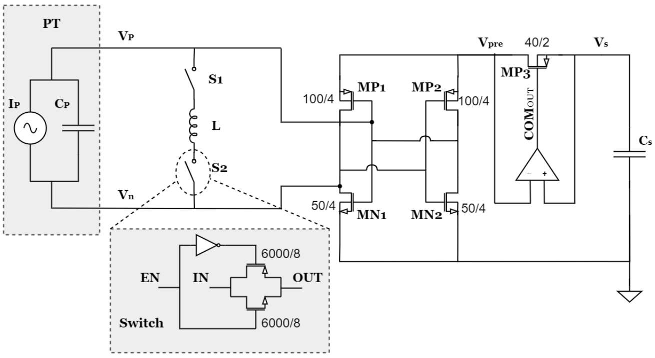

Figure 4.7: Schematic of the SSHI rectifier.

The schematic of the SSHI rectifier circuit is shown in Fig. 4.7. Similar to the passive rectifier circuit, an NVC is designed to rectify the AC voltage of PT. To increase the power transfer efficiency, an inductor and two switches are parallel connected with PT, to flip the AC voltage. When V_s is higher than V_{pre}, the comparator will generate a rising edge at its output COM_{OUT}, to the gate of the pMOS MP3. Then the MP3 is turned off to avoid the current leakage from the output capacitor C_s. Fig. 4.8 shows the schematic of the comparator, V_1 and V_2 are the input terminals of the comparator, and they connected with V_{pre} and V_s separately.

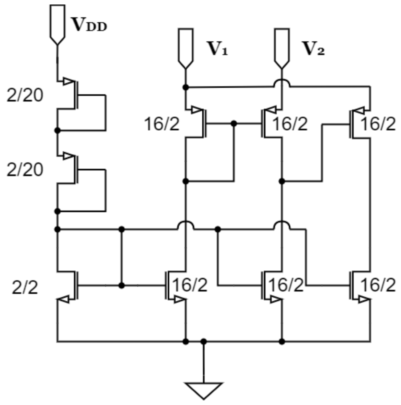

Figure 4.8: Schematic of the comparator.

Meanwhile, the rising edge from the comparator's output COM_{OUT} will pass through the switch control signal generation circuit shown in Fig. 4.9. A pulse signal will be generated by the circuit to control the COMS switch in Fig. 4.7, and the pulse width is adjustable by changing the capacitance of the out chip capacitor C_D.

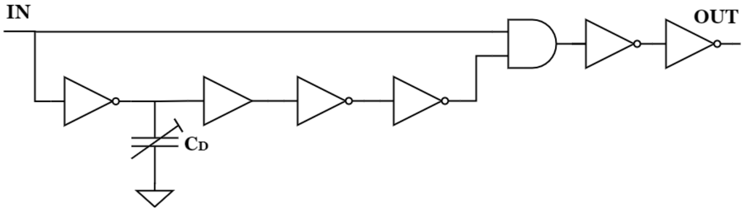

Figure 4.9: Switch control signal generation.

Considering the limitation of the SiC chip tape-out area, an out chip DC voltage source is needed to power the comparator, switches, and logical cells. In the future design, an on-chip low dropout regulator (LDO) could be added to replace the voltage source, in order to make the SSHI rectifier circuit into a fully on-chip design.

4.1.5. Results

These three rectifier circuits are sent to IISB and they will be taped out with the SiC technology. However, due to the time limitation of the project, the tape-out chip cannot be sent back before the project is finished. Therefore, only the pre-layout simulation is finished and the results are shown as follows.

Fig. 4.10 shows the simulation results of the FBR circuit (a) and passive rectifier circuit (b). The variables of this simulation are based on the results of the COMSOL modeling, where the open-circuit voltage of the PT is set to $200V$, and the frequency is $4Hz$. The inner capacitance of the PT is $20nF$, and the output capacitance is $1uF$.

In Fig. 4.10, the red line shows the voltage across PT, V_{PT}, and the blue line represents the voltage V_S on the output capacitance. The results show that both of these two rectifiers nicely convert the AC voltage across PT into a DC voltage. As a comparison, if zoom in the figure to look at the peak value of the V_{PT}, we can find that the differences between the V_{PT} and V_S of these two rectifiers are not the same, and this difference shows the voltage drop V_D through the rectifier. As for the FBR, $V_D = 8.8V$, which is higher than the voltage drop of the passive rectifier, where $V_D = 5.8V$.

This different voltage drop is caused by the structure of the rectifier. As for the FBR circuit in Fig. 4.2, the voltage drop from the V_S to V_{PT} is equal to two drain-source voltages of the pMOS transistor, but in the passive rectifier circuit in Fig. 4.5, the voltage drop from the V_S to V_{PT} is equal to two gate-source

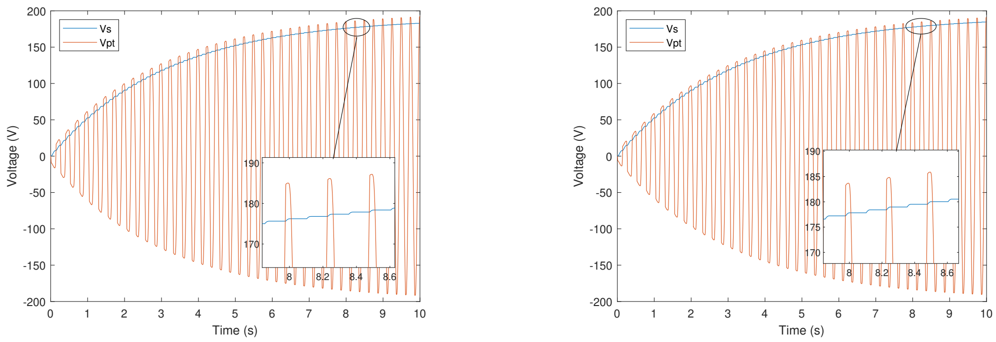

(a) Output of the FBR.

(b) Output of the passive rectifier.

Figure 4.10: Comparison of the FBR and passive rectifier.

voltages. Since the gate-source voltage is lower than the drain-source voltage when the pMOS is in the saturation region, the voltage drop of the passive rectifier is lower than the FBR.

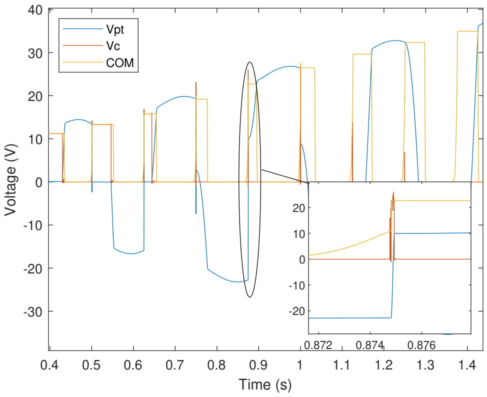

Figure 4.11: SSHI circuit simulation waveforms.

Fig. 4.11 shows the simulation waveforms of the SSHI circuit. In this figure, the voltage across PT is flipped by the switches and inductor in Fig. 4.7. The blue line represents the voltage across PT, V_{PT}, and it is flipping between positive and negative. If zoom in at the time when V_{PT} is flipping, we can see that a rising edge of the COM signal is generated, as the yellow line shows. Then the COM signal is passing through the switch control signal generation block in Fig. 4.9, and a pulse signal V_C is generated. The pulse signal V_C will turn on the switches connected with the inductor to form an RLC loop to flip the V_{PT}. Fig. 4.11 shows that the V_{PT} is flipped from around $-20V$ to $+10V$ at the zoomed area.

According to the simulation results, the output power of the rectifiers can be calculated, as shown in Fig. 4.12.

The figure shows that the SSHI achieves the highest output power $10.30mW$ when $V_C = 330V$. The output power of the passive rectifier is $2.95mW$, when $V_C = 96V$, which is a little higher than the output power of FBR which is $2.91mW$ when $V_C = 95V$.

4.1.6. Conclusion

The results show that with the same piezoelectric device, the SSHI rectifier achieves a significantly larger output power, which is $3.5\times$ than the conventional FBR. In the SSHI circuit, a $100mH$ inductor is used, and around a 40% flip efficiency is achieved. If using a larger inductor, an even higher output power will be achieved. However, the designed SSHI circuit needs an extra DC voltage supply to power the active components, such as the CMOS switches and logical blocks. In the future design, an on-chip LDO with SiC technology can be added to replace the DC voltage supply, in order to make the SSHI rectifier become fully self-sustained. Besides, a maximum power point tracking block is also needed to

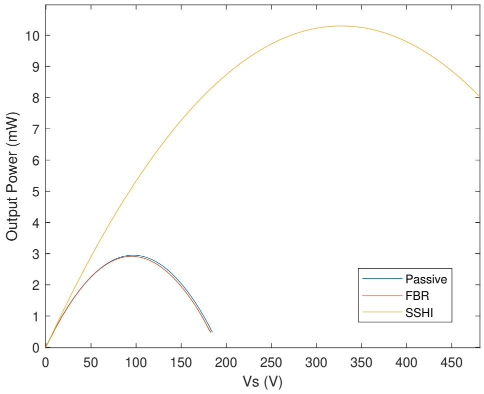

Figure 4.12: Output power of the rectifiers.

matins the maximum power. Since the maximum power point of the proposed SSHI circuit is very high ($V_C = 330V$), the circuit should be designed to have a high voltage tolerance.

As for the FBR and the passive rectifier, although they achieve a lower output power than SSHI, their generated powers also meet the requirement of the project. The simulation is made with a $20nF$ piezoelectric device, and as the discussion in the last chapter, two piezoelectric tubes with $36nF$ could be put inside the bore of the roller. Therefore, the final estimate of output power is shown in Table 4.1.

Table 4.1: Output comparison of the rectifiers

Rectifier	MPP (V)	P_{single} (mW)	$P_{all}(mW)$
SSHI	330	10.3	37.1
Passive	96	2.95	10.6
FBR	95	2.91	10.5

In this table, P_{single} represents the output power with a single $20nF$ piezoelectric device, while P_{all} represents the estimation output power of the whole bore of the roller. It shows that considering the whole area of the bore, the generated output power is more than $10mW$, both for FBR and passive rectifier. The result achieves the $5mW$ minimum output power requirement of this project.

4.2. Cold-startup SSHI rectifier circuit

In addition to the three rectifier circuits with SiC technology, another rectifier circuit with $0.18\mu m$ BCD technology is also designed to address the problem of the cold start of the SSHI system with a low open circuit voltage.

As mentioned before, the SSHI rectifier circuit is able to flip the voltage across the PT by using an inductor to form an RLC loop. However, the active components in the SSHI rectifier need a stable DC voltage supply, such as the active switches and logical control block. In many SSHI system designs, the voltage supply can be built up by the passive rectifier in the SSHI circuit, such as in [53], and [54]. However, in some cases, the PT's open circuit voltage V_{OC} could be much lower that the needed supply voltage. Hence, with enough supply voltage, the SSHI cannot to start flipping the voltage. This problem is possible to show up in this project, if the stress on the piezoelectric material is not high enough to generate the supply voltage for the active component, the SSHI rectifier is fail to start to operate.

Therefore, a reconfigurable Cold-Startup SSHI Rectifier is designed to make the SSHI rectifier able to start even if the V_{OC} is much lower than the required supply voltage.

4.2.1. Proposed design analysis

Fig. 4.13 shows the typical SSHI circuit with FBR to cold start. During the cold state, the SSHI circuit works as a passive FBR. The FBR will rectify the voltage across the PT and store the energy at the capacitor C_S. Then with the help of the LDO, a stable voltage V_{DD} is formed. Finally, the SSHI circuit will start to operate, since the active components can be powered with V_{DD}.

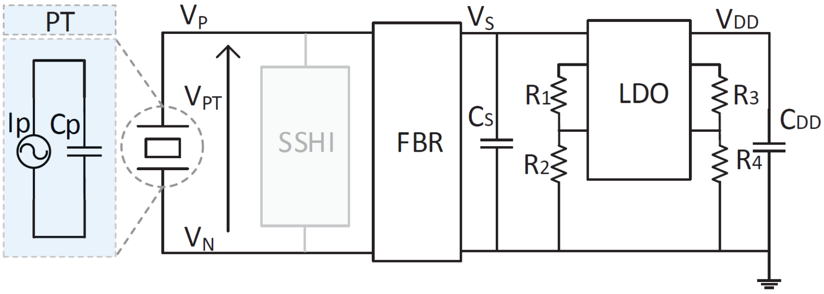

Figure 4.13: Conventional cold-startup SSHI circuit with FBR.

For the FBR, the maximum output voltage V_S is limited by the open circuit V_{OC} and the voltage drops the diode V_D as expressed below:

$$V_{S,max} = V_{OC} - 2V_D \tag{4.1}$$

Therefore, if the open circuit V_{OC} generated by the PT is not high enough, the maximum output voltage V_S will be lower than the required supply voltage V_{DD}, and the SSHI reciter will never start to correctly operate.

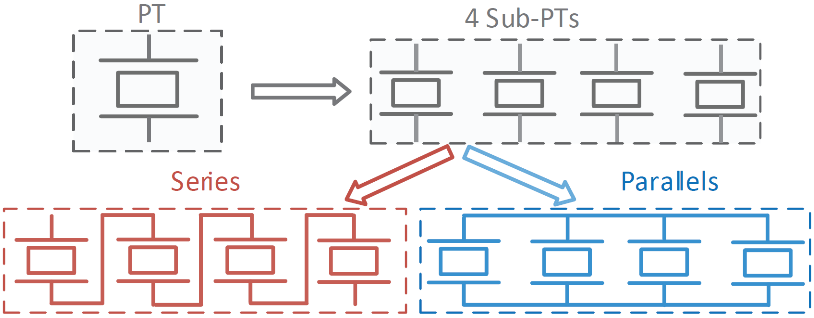

Figure 4.14: Configurable PT.

To solve this problem, in the proposed cold-startup circuit, the PT is divided into 4 equal sub-PTs, as shown in Fig. 4.14. Since these sub-PTs are fixed on the same substrate, they have the same amplitude and frequency of the generated current. Therefore, those sub-PTs can be connected in series or parallel as shown in the figure. When they are connected in parallel, they act as same as the monolithic PT. However, when they are connected in series, the total open circuit voltage is expressed as:

$$V_{OC,series} = 4 \times V_{OC} \tag{4.2}$$

and the maximum output voltage of FBR becomes:

$$V_{S,max} = V_{OC,series} - 2V_D = 4 \times V_{OC} - 2V_D \tag{4.3}$$

Consequently, the maximum output voltage V_S becomes nearly four times larger by applying the cold-startup circuit, which is a significant increase to meet the requirement of the supply voltage. As for this energy harvesting roller, to realize this circuit, a monolithic PZT ceramic in the bore can be divided into four sub-PTs as shown in Fig. 4.15. By switching the connection when the roller is working, a higher supply voltage is achieved to start the SSHI operation.

As the equation (2.17) shows, the output power of the SSHI circuit can be calculated. Assuming the following conditions: $V_{OC} = 0.5V$, $V_D = 50mV$, $\eta_{SSHI} = 85\%$, the corresponding extracted power is simulated as shown in Fig.4.16.

The grey line represents the extracted power of the series connection, while the red line shows the extracted power of the parallel connection. The simulation shows the extracted power of the series

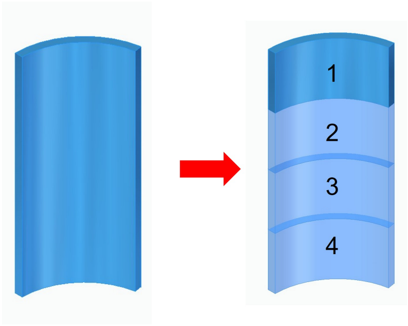

Figure 4.15: Divide monolithic PZT ceramic into sub-PTs.

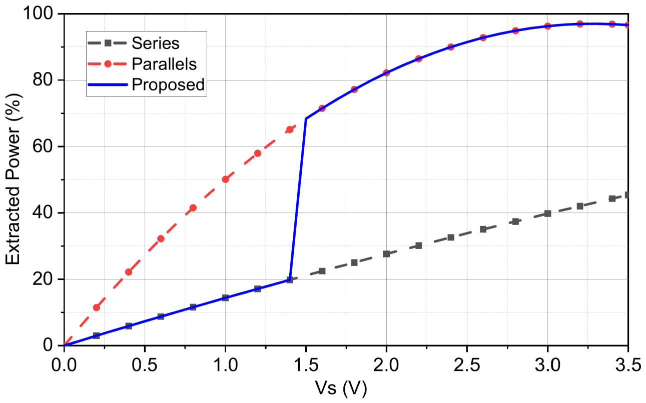

Figure 4.16: Extracted power simulation of the two connections.

connection is relatively low than the parallel connection. Therefore, a PTs connections selection is necessary to increase the extracted power: as the blue line shows, in the beginning, the series connection is selected to increase the maximum output voltage V_S. When V_S is built higher than the required supply voltage, the circuit turns into a parallel connection to achieve a higher extracted power.

4.2.2. System architecture

Fig. 4.17 shows the system architecture of the cold-startup circuit. There are mainly six blocks in the rectifier system: a PT array with 4 sub-PTs, a switch control block, a charge-up block, an SSHI rectifier, an FBR with an active diode, and an LDO.

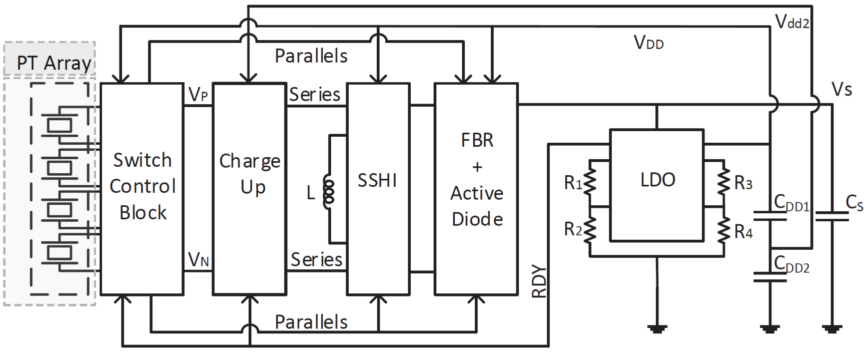

Figure 4.17: System architecture diagram.

These 4 sub-PTs are reconfigurable between series connection and parallel connection, depending on whether the cold-startup state is finished. The FBR with an active diode block is used to rectify the AC voltage generated by the PTs. The LDO is designed to regulate V_{DD} through C_{DD1} and C_{DD2} in the cold state. When the V_{DD} is built up, the LDO will generate a rising edge signal RDY to the switch control block. Then the switch control block will be able to switch the series connected PTs into parallel connections to increase the extracted power. Besides, the charge-up block connects C_{DD2} to V_P or V_N in one flip cycle to help the SSHI rectifier start to work correctly. Finally, the SSHI rectifier is started to flip the voltage across the PTs, which will significantly increase the output power.

4.2.3. Circuit implementation

The switch control block is designed to change the connection relationship between these sub-PTs as shown in Fig 4.18.

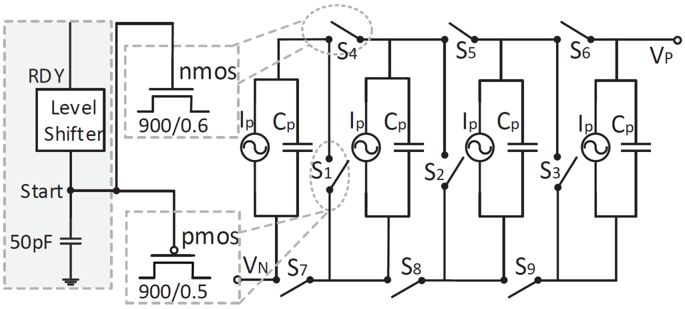

Figure 4.18: Switch control block.

In this figure, S_1, S_2, and S_3 are pMOS switches, while S_4 to S_9 are nMOS switches. The RDY signal is generated by LDO, and it will pass through a level shifter and becomes the $Start$ signal connected with the gates of these transistors. In the beginning, the RDY and $Start$ signals stay low, and all the nMOS are turned off while all the pMOS are turned on. Therefore, all the sub-PTs are connected in series. When the required V_{DD} is built up, the RDY and $Start$ signal become high to turn on all the nMOS and turn off all the pMOS. Consequently, all the sub-PTs become parallel connected. In addition, an on-chip $50pF$ capacitor is added to reduce the ripples on $Start$ signal, in order to decrease the current leakage.

However, there is still a problem that when the sub-PTs change from series connection to parallel connection after the cold-startup, the SSHI circuit cannot work correctly, since the voltage across PT will decrease by $4\times$ after the change. Besides, the open-circuit V_{OC} is not able to charge V_{PT} to overcome the threshold voltage. This would lead to the SSHI rectifier circuit going back to the cold state gradually since the parallel connected sub-PTs cannot transfer energy through the FBR to the output with a high voltage.

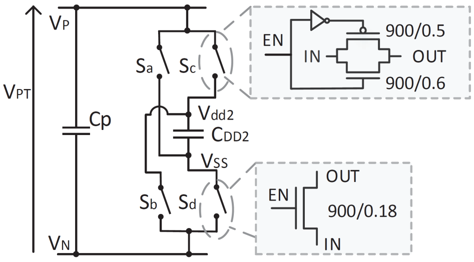

Figure 4.19: Charge-up block.

Therefore, to solve this problem, a charge-up block is designed to help charge V_{PT} to help SSHI startup. The charge-up block is only needed for one flip cycle, and its diagram is shown in Fig. 4.20. In this block, 4 switches are used to charge C_P by connecting it with C_{DD2}. S_b and S_c are transmission gates for charging, while S_a and S_d are nMOS switches connected to the ground. S_a and S_b are controlled by Φ_{VNC}, S_c and S_d are controlled by Φ_{VPC}. These two control signals, Φ_{VNC} and Φ_{VPC} are generated by the circuit in Fig. 4.20. The C_{OUT} signal is a synchronized signal indicating the moment when the voltage across the PT starts flipping, which is generated in the SSHI rectifier block, as shown in Fig. 4.22. When the C_{OUT} signal passes through a buffer, the SYN signal is generated, then it will form a pulse Φ_C by the pulse generation block. Besides, the PN signal is used to indicate the polarity of V_{PT} to determine the charging direction.

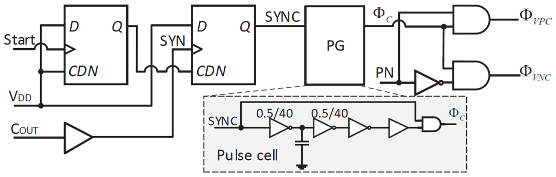

Figure 4.20: Charge-up control signal generation.

Finally, with the help of the charge-up block, PT voltage would be high enough to overcome the threshold to charge C_S, and the SSHI rectifier will start to work. the SSHI rectifier block is shown in Fig. 4.22, which structure is close to the SiC SSHI rectifier in Fig 4.7. When $V_1 < V_2$, the comparator will generate a rising edge at the output C_{OUT}. This rising edge will turn off the pMOS M_0 to reduce the leakage current. The rising edge also indicates the end of the charge and it is time to start the flip. Therefore, the C_{OUT} signal is used to control the flip switch S_0 indirectly. By turning off the switch S_0, an RLC loop is formed to flip the voltage, in order to achieve a higher output power.

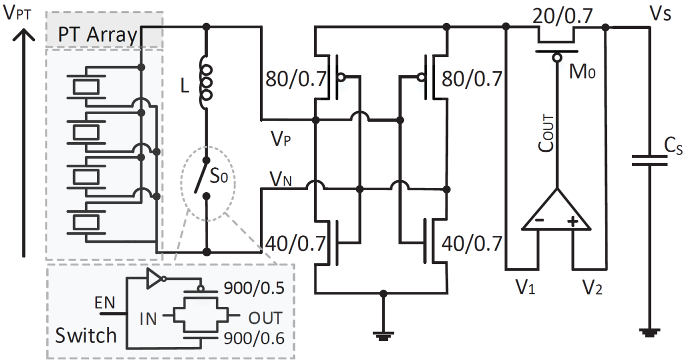

Figure 4.21: SSHI rectifier block.

4.2.4. Results

The Cold-startup SSHI rectifier is designed with the $0.18\mu m$ BCD process, and Fig. 4.22 shows the layout of the rectifier, whose area is $0.19mm^2$. The corresponding post-layout simulation results are shown as follows.

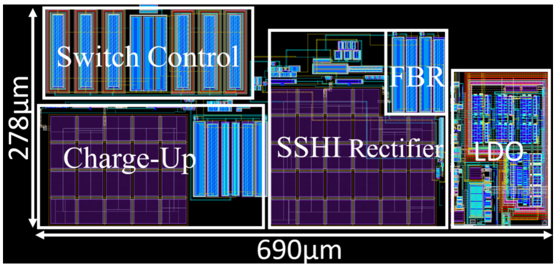

Figure 4.22: Layout diagram of the Cold-startup SSHI rectifier.

Fig. 4.23 presents the comparison of the conventional cold-startup circuit (a) and the proposed cold-startup circuit (b). For the conventional circuit, when the input open-circuit voltage V_{OC} reaches $0.5V$, the maximum voltage across PT V_{PT} is bounded at $0.5V$, while the maximum output voltage V_S is only around $0.4V$. As a comparison, for the proposed cold-startup circuit, the simulation results show that the maximum voltage across PT V_{PT} and the maximum output voltage V_S are both close to $1.9V$. This maximum output voltage is high enough to build a V_{DD} of $1.8V$.

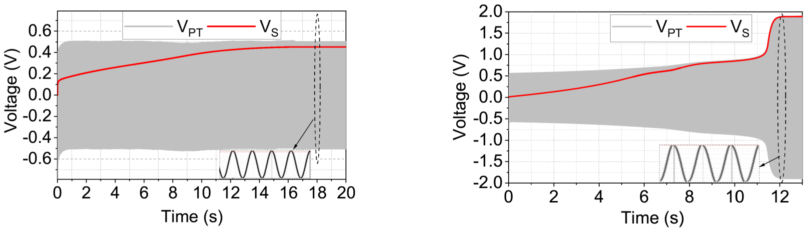

(a) Conventional cold-startup.

(b) Proposed cold-startup.

Figure 4.23: Comparison of conventional and proposed cold-startup.

Fig. 4.24 shows the important signals during the process of cold-startup. The output voltage V_S is simulated to be charged from $0V$ to $3.5V$, and the voltage V_{DD} is gradually built up to $1.8V$. During the cold state, the $Start$ signal with the red line keeps a low voltage to turn on the pMOS switches and turn off the nMOS switches in Fig. 4.18 to make the sub-PTs connected in series. When V_{DD} reaches $1.8V$, the cold state is finished and the RDY signal generates a rising edge. At this moment, the $Start$ signal turns to a high voltage following the V_S to turn off the pMOS switches and turn on the nMOS switches, in order to change the sub-PTs into parallel connection.

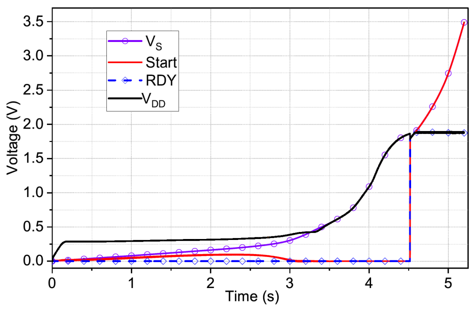

Figure 4.24: Output signals of the proposed design.

Finally, Fig. 4.25 simulated the output power rating to the output voltage V_S. The red line shows the output power of the FBR, where the maximum is $1.12\mu W$, and the corresponding output voltage V_S of the FBR is limited by $0.4V$. The black line shows the output power of the proposed design. The simulation results show that when V_S reaches $1.8V$ to provide the stable V_{DD}, the sub-PTs are reconfigured to parallel connection, and the charge-up block generates a signal Φ_{VNC} to flip the V_{PT} from negative to positive. Then the SSHI rectifier starts to operate, the output power is significantly increased and V_S can be charged to a higher voltage. As a result, the output power becomes $27.1\mu W$ when $V_S = 3.3V$.

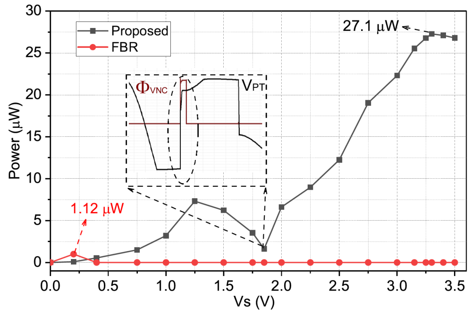

Figure 4.25: Output power of proposed design and FBR.

4.2.5. Conclusion

The proposed cold-startup SSHI rectifier circuit can be used to generate a $4 \times V_{OC}$ to build up the V_{DD} by configuring the four series connected sub-PTs into parallel connected. In the circuit, an LDO is used to build a $1.8V$ stable V_{DD}, and a charge-up block is designed to overcome the threshold voltage after the cold-startup. An SSHI rectifier block is used to improve the output power efficiency by flipping the voltage across the PT.

Consequently, the post-layout simulation results show that a $1.8V$ V_{DD} is built up by a $0.5V$ open-circuit voltage. The simulated maximum output power is $27.1\mu W$, which is $24\times$ larger than the conventional FBR circuit.

This proposed cold-startup SSHI rectifier circuit is useful to the energy harvesting roller if the generated open-circuit voltage is not high enough to build up the power supply of the active components. By dividing the piezoelectric device into sub-PTs, the idea of the proposed cold-startup circuit is possible to use in the final energy harvesting roller with different open-circuit voltage.

5

Conclusion and future work

This chapter first summarized the primary process and production of this project. Then the conclusion is drawn. Besides, this chapter brings up the work that could do in the future, including the planned harvester design and circuit design.

5.1. Summary

During this project, two generations of the energy harvester transducer prototype are made. The simulations and tests of the first prototype show many vital properties of the piezoelectric material and also provide a lot of useful information to improve the energy harvester.

Although the structure is too simple to be used in the roller, the first prototype shows the possible output power of $106.4mW$, which is much higher than the goal of the project. However, the test of the first prototype shows the frangibility of the piezoelectric ceramic material, and a $3.75MPa$ safe pressure level is defined with the destructive test. According to the test with the real components, Even with the safe pressure level, the output goal still can be achieved with a simple FBR circuit, and it will be significantly increased by using an SSHI rectifier. More than $15mW$ output power is achieved with an SSHI rectifier that only has 40% flip efficiency.

As for the design of the second prototype, the simulations about the supporting material and the piezoelectric material rule out some uncertainties in the first prototype design. Then a tube shape structure is selected and built as the final structure that will be used in the real roller. With the simulation and calculation, under the pressure level, an $8.1mW$ output power is achieved with the SSHI circuit. If the piezoelectric device is strong enough to stand the maximum displacement, a $19.2mW$ output power is easily obtained with a simple FBR circuit, and a $76.8mW$ output power is also possible with the help of an SSHI circuit. To make the piezoelectric transducer get enough pressure, a preload is necessary. Two preload structures are also designed. Currently, the second prototype is being manufactured with the help of SKF. In the future, a system-level test will be prepared to verify the performance of the prototype in the real roller in the bearing.

To further improve the performance of the Sensor Roller, four rectifier circuits are designed and taped out with different specialties. Three rectifier circuits are made with SiC technology which has a higher voltage and temperature tolerance than conventional Si technology: an FBR circuit, a passive rectifier circuit, and an SSHI rectifier circuit. As a result, both the FBR and the passive rectifier achieved more than $10mW$ output power with the proposed piezoelectric transducer in the roller. Under the same condition, the SSHI rectifier achieved a $37.1mW$ output power at the $330V$ maximum power point, which is $3.5\times$ larger than the simple FBR.

To solve the cold start problem when the open circuit is low, a cold-startup rectifier is designed and tape-out with the $0.18\mu m$ Silicon BCD process. By configuring the four sub-PTs from the series connection into the parallel connection, a $4\times$ open-circuit voltage is achieved to start up the circuit. As a result, the post-layout simulation shows that a $1.8V$ supply voltage is successfully built up by a $0.5V$ open-circuit voltage. The simulated maximum output power is $27.1\mu W$, which is $24\times$ large than the conventional FBR circuit.

5.2. Conclusion

Consequently, based on the results of this project, the following main conclusions are drawn:

- After the simulations and tests of the two generations of the harvester prototype, the results show a great possibility of replacing the battery with the piezoelectric energy harvester in the Sensor Roller. With the help of the piezoelectric energy harvester, the Sensor Roller will become a fully self-sustaining device, whose lifetime will also be significantly increased.
- The main physical part of the energy harvester is carefully designed, but some small parts of the Sensor Roller should be designed in the future, such as the preload structure and wire connections.
- To make the new Sensor Roller that can be directly used in the bearing, some system-level tests are necessary. Since there will be some manufacturing tolerances, the results of the tests could be different from the simulations. Therefore, some parameters could be adjusted in the future.
- The simulation of the proposed SiC rectifier circuits shows great compatibility between the high voltage tolerance of the SiC technology with the high-pressure working condition of the roller. In future commercial version Sensor Roller design, the SiC IC circuit will be a great choice compared with conventional Silicon IC technology.
- The idea of the re-configurable cold-startup SSHI rectifier shows a nice solution when the open circuit is too low to make the SSHI circuit work correctly. This circuit could be applied in the Sensor Roller by dividing the piezoelectric transducer into sub-PTs, in order to fix the problem that the generated open-circuit voltage is too low to start the SSHI circuit.

5.3. Future work

Due to the limited time of the project and some delays in the manufacturing, some work is still being processed and will be finished in the future. In this section, some arranged works are presented, and some plans for the future to improve the Sensor Roller are also introduced.

5.3.1. Planned tests

According to the plan, two tests will be made to check the final performance of the proposed piezoelectric energy harvester. One of the tests focuses on the output power of the piezoelectric material in the tube structure, while the other test concentrates on the overall performance of the harvester.

Test of the second prototype

To verify the result of the second prototype output power, a test is been preparing as shown in Fig. 5.1.

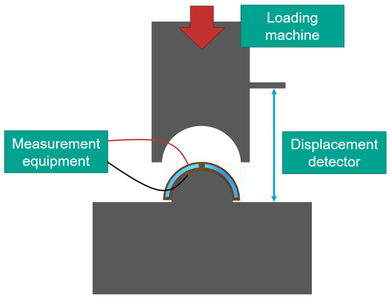

Figure 5.1: Demo of the planned second prototype test.

Instead of using the whole harvester, a half circle harvester is designed to save the time of preload structure design. Same with the original harvester, a three-layers structure is used: one piezoelectric layer inside, covered with two supporting layers. As shown in the figure, a half circle shape clamp is designed to hold the half tube harvester. The clamp will be attached with a dynamic test machine as used in the first prototype test. Since the input of the second prototype is displacement rather than pressure, a displacement detector will be used in the test to detect the applied displacement on the harvester.

When applying the same displacement in the simulation, the half circle harvester will be stressed and an open circuit will be generated by the piezoelectric transducer. Then by using the measurement equipment, such as the oscilloscope, the open-circuit voltage will be measured and recorded. With the data of the open-circuit voltage, the output power of the half circle will be calculated. Based on that, the overall output power will also be estimated.

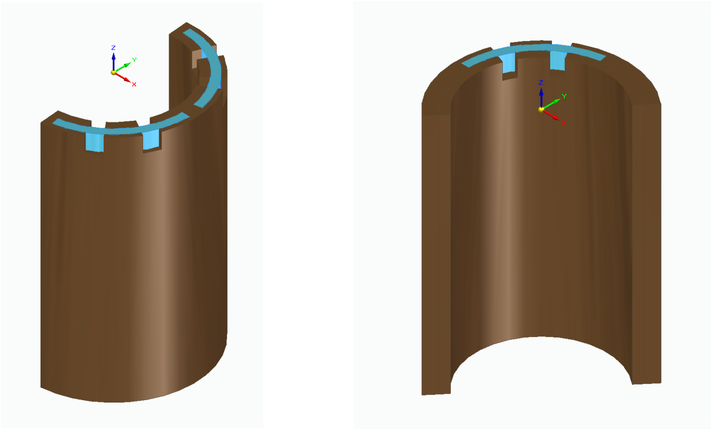

(a) Edge situation.

(b) [Middle situation.

Figure 5.2: The half circle harvesters with two situations.

However, this test cannot simulate the rotation of the roller. Therefore, as shown in Fig. 5.2, two half-circle harvesters with two situations are designed to analyze the output power then the roller is rotating. One is the edge situation when the pressure is mostly focused on the edge of each piezoelectric segment, while another is the middle situation when the pressure is applied to the middle of the segment. These two situations represent two extreme circumstances when the roller is rotating. Therefore, the real reaction of the harvester in the roller can be predicted by analyzing these two situations.

System-level test

When the simulated output power results are verified by the second prototype test, a system-level test is designed to test the final performance of the energy harvester. Different from the second prototype test, the system-level test should be made in the real working condition. Therefore, the proposed piezoelectric energy harvester will be embedded in the target roller and installed in the real bearing to get tested.

The goal of the system-level test is to figure out how much the output power will be generated. Therefore, the open-circuit voltage should be measured in the test. However, since the roller will be installed in the huge bearing, the measurement with a wire connection is no longer possible. Therefore, as Fig. 5.3 shows, a test circuit is planned to design to be used in the System-level test which can measure the open-circuit voltage wirelessly.

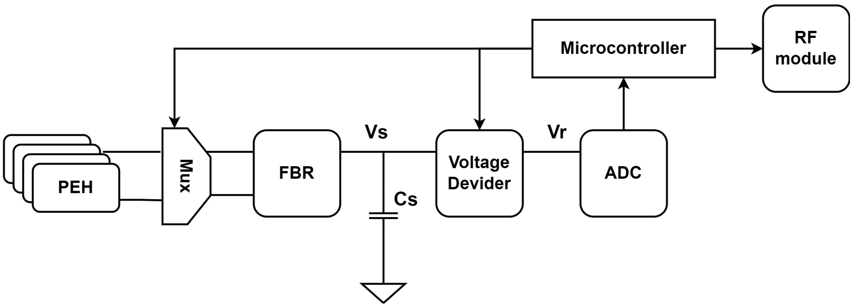

Figure 5.3: Test circuit architecture.

Since there will be four piezoelectric segments in the harvester, a multiplexer is used to select one of the piezoelectric segments to get measured. The voltage across the PEH will be verified by a simple FBR, and the generated voltage will charge a capacitor C_S. By measuring the voltage V_S on the capacitor with the ADC, the output power of a single segment will be calculated. However, since the input range of the ADC is limited and the voltage on C_S cannot be determined before the test, a voltage divider is designed to divide the V_S into V_r with a certain dividing ratio, then it can be measured by the ADC. The measurement data will be transferred to a micro-controller by the ADC, and then it will send to the host wirelessly by the RF module. The micro-controller is also used to select the channel of the four piezoelectric segments and adjust the dividing ratio of the voltage divider.

5.3.2. Future harvester design

For the commercial version of the energy harvesting roller in the future, there are some extra parts that should be designed:

- The preload structure will be added inside the tube shape harvester. Two structures are already designed and waiting to be manufactured, as shown in chapter 3.
- The connections between the harvester and the circuit should be designed in the future. Since the remaining space in the bore of the roller is limited, the connection should be small to put inside the roller.
- The seal parts are needed at the two sides of the roller to isolate the harvester from the outsides, but it should not block the connect signal between the RF module and the outer host.

These extra parts are not as important as the energy harvester, but they are still necessary to guarantee the correct functioning of the energy harvesting roller. These extra parts could get manufactured and tested together in the final system-level test.

5.3.3. Future circuit design

From the aspects of the circuit design, there are some points that could be designed in the future to improve the performance of the energy harvesting roller:

- The maximum power point tracking (MPPT) technique could be used in the proposed SSHI circuit. With the help of the MPPT block, the generated output power of the roller will maintain at a higher level.
- A rechargeable battery or a supercapacitor can be added to the energy harvesting roller to store the generated power. Since the sensors in the roller are not always used, the power could be stored and reused with the help of the power storage component.

References

[1] *Number of connected IoT devices growing 18% to 14.4 billion globally*. `https://iot-analytics.com/number-connected-iot-devices/`. (Accessed on 08/01/2022).

[2] Massimo Alioto. “From Less Batteries to Battery-Less Alert Systems with Wide Power Adaptation down to nWs—Toward a Smarter, Greener World”. In: *IEEE Design Test* 38.5 (2021), pp. 90–133. DOI: `10.1109/MDAT.2021.3069087`.

[3] Chrysanthi Tziortzioti et al. “IoT sensors in sea water environment: Ahoy! Experiences from a short summer trial”. In: *Electronic Notes in Theoretical Computer Science* 343 (2019). The proceedings of AmI, the 2018 European Conference on Ambient Intelligence., pp. 117–130. ISSN: 1571-0661. DOI: `https://doi.org/10.1016/j.entcs.2019.04.014`. URL: `https://www.sciencedirect.com/science/article/pii/S1571066119300179`.

[4] Hongzhi Guo and Albert A Ofori. “The internet of things in extreme environments using low-power long-range near field communication”. In: *IEEE Internet of Things Magazine* 4.1 (2021), pp. 34–38.

[5] James F Tressler, Sedat Alkoy, and Robert E Newnham. “Piezoelectric sensors and sensor materials”. In: *Journal of electroceramics* 2.4 (1998), pp. 257–272.

[6] Soham Adhya et al. “An IoT based smart solar photovoltaic remote monitoring and control unit”. In: *2016 2nd international conference on control, instrumentation, energy & communication (CIEC)*. IEEE. 2016, pp. 432–436.

[7] Maciej Haras and Thomas Skotnicki. “Thermoelectricity for IoT–A review”. In: *Nano Energy* 54 (2018), pp. 461–476.

[8] Erick O Torres and Gabriel A Rincón-Mora. “Electrostatic energy-harvesting and battery-charging CMOS system prototype”. In: *IEEE Transactions on Circuits and Systems I: Regular Papers* 56.9 (2008), pp. 1938–1948.

[9] *Energy Harvesting System Market Size Report, 2028*. `https://www.grandviewresearch.com/industry-analysis/energy-harvesting-systems-market`. (Accessed on 08/02/2022).

[10] *SKF Group homepage | SKF*. `https://www.skf.com/id`. (Accessed on 08/02/2022).

[11] *SKF Sensor roller collects information from large bearings | Evolution*. `https://evolution.skf.com/raising-the-bar-for-collecting-bearing-data/`. (Accessed on 08/10/2022).

[12] Warren P. Mason. “Piezoelectricity, its history and applications”. In: *The Journal of the Acoustical Society of America* 70.6 (1981), pp. 1561–1566. ISSN: 0001-4966. DOI: `10.1121/1.387221`.

[13] PI Ceramic GmbH. *Fundamentals of Piezo Technology*. URL: `https://www.piceramic.com/en/expertise/piezo-technology/fundamentals/`.

[14] Steven R Anton and Henry A Sodano. “A review of power harvesting using piezoelectric materials (2003–2006)”. In: *Smart materials and Structures* 16.3 (2007), R1.

[15] *Piezoceramic Materials*. `https://www.physikinstrumente.nl/en/expertise/technology/piezo-technology/piezoelectric-materials/`. (Accessed on 06/29/2022).

[16] *PZT Properties & PZT Manufacturing*. `https://www.americanpiezo.com/piezo-theory/pzt.html`. (Accessed on 06/23/2022).

[17] *PVDF Films | Supplier | Manufacturer | - TCI, Textiles Coated International*. `https://www.textilescoated.com/pvdf-films`. (Accessed on 06/29/2022).

[18] Anjana Jain et al. “Dielectric and piezoelectric properties of PVDF/PZT composites: A review”. In: *Polymer Engineering & Science* 55.7 (2015), pp. 1589–1616.

[19] Bilal Zaarour et al. “A review on piezoelectric fibers and nanowires for energy harvesting”. In: *Journal of Industrial Textiles* 51.2 (2021), pp. 297–340.

[20] Xi Chen et al. “1.6 V nanogenerator for mechanical energy harvesting using PZT nanofibers”. In: *Nano letters* 10.6 (2010), pp. 2133–2137.

[21] *Introduction to Piezoelectricity | PIEZO.COM*. `https://piezo.com/pages/intro-to-piezoelectricity`. (Accessed on 06/30/2022).

[22] Ching-Yu Lin and Nesbitt W Hagood. “Compression depolarization of PZT piezoelectric materials under high electromechanical driving levels”. In: *Smart Structures and Materials 2000: Active Materials: Behavior and Mechanics*. Vol. 3992. SPIE. 2000, pp. 114–125.

[23] Nurettin Sezer and Muammer Koç. “A comprehensive review on the state-of-the-art of piezoelectric energy harvesting”. In: *Nano Energy* 80 (2021), p. 105567.

[24] MY Gao et al. “A rail-borne piezoelectric transducer for energy harvesting of railway vibration”. In: *Journal of vibroengineering* 18.7 (2016), pp. 4647–4663.

[25] Nan Chen et al. “A piezoelectric impact-induced vibration cantilever energy harvester from speed bump with a low-power power management circuit”. In: *Sensors and Actuators A: Physical* 254 (2017), pp. 134–144.

[26] Roja Esmaeeli et al. “A rainbow piezoelectric energy harvesting system for intelligent tire monitoring applications”. In: *Journal of Energy Resources Technology* 141.6 (2019).

[27] Anil Can Turkmen and Cenk Celik. “Energy harvesting with the piezoelectric material integrated shoe”. In: *Energy* 150 (2018), pp. 556–564.

[28] Woo-Suk Jung et al. “Powerful curved piezoelectric generator for wearable applications”. In: *Nano Energy* 13 (2015), pp. 174–181.

[29] NA Kong et al. “Resistive impedance matching circuit for piezoelectric energy harvesting”. In: *Journal of Intelligent Material Systems and Structures* 21.13 (2010), pp. 1293–1302.

[30] Yogesh K Ramadass and Anantha P Chandrakasan. “An efficient piezoelectric energy harvesting interface circuit using a bias-flip rectifier and shared inductor”. In: *IEEE journal of solid-state circuits* 45.1 (2009), pp. 189–204.

[31] Lin Cheng et al. “Adaptive on/off delay-compensated active rectifiers for wireless power transfer systems”. In: *IEEE Journal of Solid-State Circuits* 51.3 (2016), pp. 712–723.

[32] Ahmadreza Tabesh and Luc G Fréchette. “A low-power stand-alone adaptive circuit for harvesting energy from a piezoelectric micropower generator”. In: *IEEE Transactions on Industrial Electronics* 57.3 (2009), pp. 840–849.

[33] Ethem Erkan Aktakka and Khalil Najafi. “A micro inertial energy harvesting platform with self-supplied power management circuit for autonomous wireless sensor nodes”. In: *IEEE Journal of Solid-State Circuits* 49.9 (2014), pp. 2017–2029.

[34] Sijun Du et al. “A nail-size piezoelectric energy harvesting system integrating a MEMS transducer and a CMOS SSHI circuit”. In: *IEEE Sensors Journal* 20.1 (2019), pp. 277–285.

[35] *Single row cylindrical roller bearings | SKF*. `https://www.skf.com/in/products/rolling-bearings/roller-bearings/cylindrical-roller-bearings/single-row-cylindrical-roller-bearings`. (Accessed on 07/10/2022).

[36] *RPT File (What It Is & How to Open One)*. `https://www.lifewire.com/rpt-file-4153494`. (Accessed on 07/08/2022).

[37] *MATLAB - MathWorks - MATLAB & Simulink*. `https://ww2.mathworks.cn/en/products/matlab.html`. (Accessed on 07/10/2022).

[38] *COMSOL - Software for Multiphysics Simulation*. `https://www.comsol.com/`. (Accessed on 07/12/2022).

[39] COMSOL Multiphysics. “Introduction to comsol multiphysics®”. In: *COMSOL Multiphysics, Burlington, MA, accessed Feb* 9.2018 (1998), p. 32.

[40] *Efficiently Mesh Your Model Geometry with Meshing Sequences | COMSOL Blog*. `https://www.comsol.com/blogs/efficiently-mesh-your-model-geometry-with-meshing-sequences/`. (Accessed on 07/14/2022).

[41] *Virtuoso Analog Design Environment | Cadence*. `https://www.cadence.com/ko_KR/home/tools/custom-ic-analog-rf-design/circuit-design/virtuoso-analog-design-environment.html`. (Accessed on 07/28/2022).

[42] *STEMINC - Piezoceramic Discs, Plates, Transformers, Bimorphs and Cylinders*. `https://www.steminc.com/PZT/en/`. (Accessed on 07/15/2022).

[43] *Dynamic and Fatigue Testing Systems - Instron*. `https://www.instron.com/en/products/testing-systems/dynamic-and-fatigue-systems`. (Accessed on 07/15/2022).

[44] *How to Inspect Your Mesh in COMSOL Multiphysics® | COMSOL Blog*. `https://www.comsol.com/blogs/how-to-inspect-your-mesh-in-comsol-multiphysics/`. (Accessed on 07/19/2022).

[45] *Forces and Stiffness*. `https://www.physikinstrumente.com/en/expertise/technology/piezo-technology/properties-piezo-actuators/forces-stiffnesses/`. (Accessed on 07/31/2022).

[46] *Solid Edge | Siemens | 3D Design, Simulation, Manufacturing*. `https://solidedge.siemens.com/en/`. (Accessed on 08/01/2022).

[47] *Silicon Carbide Market Size & Share Report, 2030*. `https://www.grandviewresearch.com/industry-analysis/silicon-carbide-market`. (Accessed on 07/19/2022).

[48] *Demystifying SiC MOSFETs challenges - Power Electronics News*. `https://www.powerelectronicsnews.com/demystifying-sic-mosfets-challenges/`. (Accessed on 07/19/2022).

[49] Werner Martienssen and Hans Warlimont. *Springer handbook of condensed matter and materials data*. Vol. 1. Springer, 2005.

[50] *Fraunhofer IISB (English)*. `https://www.iisb.fraunhofer.de/`. (Accessed on 07/19/2022).

[51] Geetanjali Singh, Srikanta Pal, and Sudip Kundu. “Efficient rectifier for piezoelectric energy harvester using active diode”. In: *2021 devices for integrated circuit (DevIC)*. IEEE. 2021, pp. 383–387.

[52] Koji Kotani and Takashi Ito. “High efficiency CMOS rectifier circuits for UHF RFIDs using Vth cancellation techniques”. In: *2009 IEEE 8th International Conference on ASIC*. IEEE. 2009, pp. 549–552.

[53] Shaochen Xi et al. “A self-powered piezoelectric energy harvesting interface circuit based on adaptive SSHI with fully integrated switch control”. In: *2020 IEEE International Symposium on Circuits and Systems (ISCAS)*. IEEE. 2020, pp. 1–4.

[54] Son H Nguyen, Heather Richardson, and Rajeevan Amirtharajah. “A Bias-Flip Interface and Dual-Input DC-DC Converter for Piezoelectric and RF Energy Harvesting”. In: *2021 IEEE International Symposium on Circuits and Systems (ISCAS)*. IEEE. 2021, pp. 1–5.

A

Publication I

A Reconfigurable Cold-Startup SSHI Rectifier with 4X Lower Input Amplitude Requirement for Piezoelectric Energy Harvesting.

A Reconfigurable Cold-Startup SSHI Rectifier with 4X Lower Input Amplitude Requirement for Piezoelectric Energy Harvesting

Xinling Yue[1], Yiwei Zou[1], Zhelun Chen[1], Junrui Liang[2] and Sijun Du[1]
[1] Department of Microelectronics, Delft University of Technology, Delft, The Netherlands
[2] School of Information Science and Technology, ShanghaiTech University, Shanghai, China
Email: sijun.du@tudelft.nl

***Abstract*—Synchronized switch harvesting on inductor (SSHI) is an efficient active rectifier to extract energy generated from piezoelectric transducer in piezoelectric energy harvesting system. Unlike passive rectifiers, SSHI rectifiers require a power supply to drive synchronized switches. Unfortunately, there is no stable supply when the system starts from the cold state. Most designs let the system work as a passive full bridge rectifier (FBR) to charge power capacitor until a supply is available. However, a FBR requires high open-circuit voltage (V_{OC}) and the FBR's output voltage cannot go over V_{OC}. This prevents the system from starting the SSHI rectifier if V_{OC} is low. This paper proposes a new transducer reconfiguration design to lower the required V_{OC} by 4× to start up the SSHI system from the cold state. The proposed system is designed in a 0.18-μm BCD process and post-layout simulations show that the successful cold-startup under low V_{OC} voltage.**

***Index Terms*—Cold-startup, energy harvesting, full bridge rectifier, open-circuit voltage, piezoelectric transducer, SSHI rectifier**

I. INTRODUCTION

Wireless sensors require batteries to operate, which are typically large in size and limited in lifetime. Extra costs would be introduced due to battery replacements. Piezoelectric energy harvesting (PEH) is a technique to harvest kinetic energy from the environment and generate electricity as an output. This technique is a promising way to untether from conventional batteries and achieve self-powered autonomy. In order to extract AC energy from piezoelectric transducer (PT) and convert it to DC energy, a rectifier is generally required. A Full bridge rectifier (FBR) is a widely used rectifier, but the output power and conversion efficiency of a FBR is relatively low. Some active designs like synchronous electric charge extraction (SECE) [1], [2], and synchronized switch harvesting (SSH) rectifiers [3]–[9] are all exploited to improve the output power extracted from the PT.

FBR results in low power conversion efficiency when PT voltage is flipped from positive to negative or vice versa. A SSHI rectifier helps to flip PT voltage to improve the power extraction with an inductor by forming a RLC oscillation loop. However, all active rectifiers require a stable DC supply (V_{DD}) to operate. In some cases, before V_{DD} is prepared, the interface circuits are out of charge and performed as a passive rectifier to build up the power supply. In [10], [11], high-efficiency SSHI rectifiers were proposed. However, these papers did not give more details realising cold-startup when the open-circuit voltage amplitude (V_{OC}) from the PT is lower than required power supply. The tricky thing is that when V_{OC} is lower than the required V_{DD}, the FBR is unable to build up a ready-use V_{DD} to power the SSHI rectifier; As a result, the SSHI rectifier would not start operating and flipping the voltage, which indicates the cold-start failure.

This paper proposes a new PT configuration design associated with a reconfigurable SSHI rectifier to realize cold-startup when the input V_{OC} is much smaller than the required V_{DD}. The post-layout simulations show that the system can be started from the cold state when V_{OC} is only $0.5\,\mathrm{V}$.

This paper is organised as follows: Analysis of the proposed design is given in Section II. Section III presents the system architecture. Circuit implementations are displayed in Section IV. Post-layout simulation results are shown in Section V to outline the effectiveness of the proposed design. Finally, Section VI summarises the work.

II. PROPOSED DESIGN ANALYSIS

A. Conventional Cold-Startup

Typically, during the cold state, a SSHI rectifier simply works as a passive FBR. Fig. 1 shows the equivalent circuit diagram during the cold-startup. The PT is modeled as an AC current source, I_P, in paralleled with a capacitor, C_P. A FBR is used to rectify the AC energy. The harvested energy is stored in a storage capacitor, C_S. A LDO is employed to generate a stable supply, V_{DD}, from V_S. When the cold state finishes, the proposed active rectifier would start operating with a stable V_{DD}. For a FBR, the maximum output voltage V_S is limited by V_{OC} and V_D as expressed below

$$V_S(max) = V_{OC} - 2V_D \tag{1}$$

where V_D is the voltage drop of the diode used in a FBR. However, for low excitation when $V_{OC} < V_{DD}$, the maximum output voltage V_S is also lower than V_{DD}. A desired V_{DD} would never be ready; hence, the cold state would not end and the designed active rectifier would not start operating.

B. Proposed Cold-Startup

In the proposed cold-startup circuit, the PT is divided into 4 equal sub-PTs as shown in Fig. 2. Because these sub-PTs

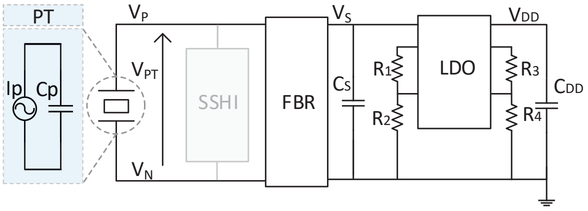

Fig. 1: Conventional cold-startup circuit – FBR

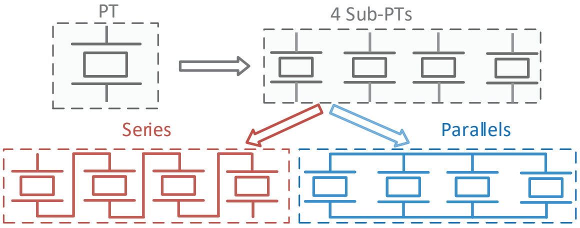

Fig. 2: PTs configurable

are fixed on the same substrate, they have the same frequency and amplitude when vibrating. Therefore, these PTs can be connected in series or parallel which are displayed at the bottom of Fig. 2. The parallel-connected output V_{OC} is the same as that of the monolithic PT; hence, is not able to build up a high V_S to generate a valid V_{DD} under low extraction levels. However, if the 4 sub-PTs are connected in series in cold state, the resulting output $V_{OC-series}$ is expressed as

$$V_{OC-series} = 4 \times V_{OC} \tag{2}$$

The maximum achievable ouput power of the FBR can be rewritten as

$$V_S(max) = V_{OC-series} - 2V_D = 4V_{OC} - 2V_D \tag{3}$$

Since the effective V_{OC} from the series-connected PT is increased by 4×, the new maximum output voltage V_S is also increased by approximately 4×. Assuming that the V_{OC} is $0.5\,\mathrm{V}$ and V_D is around $50\,\mathrm{mV}$, the series PTs would be able to build up 1.9-V V_S; as a result, up to 1.9-V V_{DD} can also be generated to start active rectification. However, for conventional cold-startup, the V_S can only be charged to $0.4\,\mathrm{V}$ (= $0.5\,\mathrm{V} - 2 \times 0.05\,\mathrm{V}$), which is too low to start active rectification. Hence, in our proposed design, the 4 sub-PTs are connected in series by default during the cold state to ensure successful cold-startup even at low V_{OC} levels.

C. PTs Connections Selection - After Cold-Startup

When cold-startup ends, it is important to find a suitable connection for these sub-PTs. Output power comparisons between series and parallel configurations are analyzed to find which connection is better for normal active rectification. When the active SSHI rectifier begins to work, according to [12], the extracted power from the SSHI rectifier is written as

$$P_{SSHI} = 2f_P C_P V_S (2V_{OC} - (V_S + 2V_D)\eta_L) \tag{4}$$

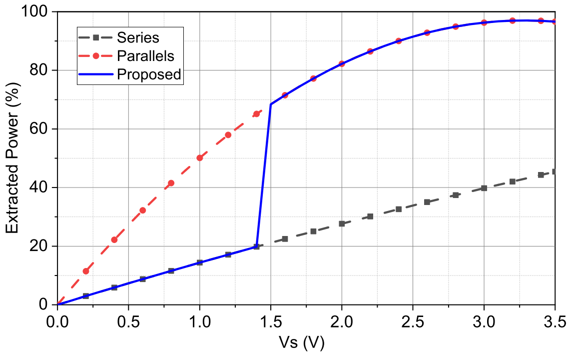

Fig. 3: Extracted power in different PT connections

where $\eta_L = 1 - \eta_F$, η_F is the flip efficiency of the SSHI rectifier and f_P is the vibrating frequency of PT. The above equation shows that when $V_S = \frac{V_{OC}}{\eta_L} - V_D$, the maximum power is written as

$$P_{SSHI}(max) = 2C_P f_P \eta_L (\frac{V_{OC}}{\eta_L} - V_D)^2 \tag{5}$$

The corresponding extracted power simulation results from PT are shown in Fig. 3 with the conditions: $V_{OC} = 0.5\,\mathrm{V}$, $\eta_L = 15\%$, $V_D = 50\,\mathrm{mV}$. When the PTs are connected in series, corresponding output efficiency with changing V_S is in grey dash line. It shows that the series-connected power is always lower than the red one representing the parallel connection. However, paralleled output 0.5-V V_{OC} is too low to build up required 1.8-V V_{DD} in cold state. Therefore, 4 sub-PTs are connected in series by default to increase V_{OC} at the beginning to build up V_{DD} during startup period. Then, the connection changes to parallel for extracting more power. Thus, in Fig. 3, the output power follows the grey one until startup ends and changes to red line, so the system output power follows the blue solid line.

III. SYSTEM ARCHITECTURE

Fig. 4 shows the system architecture. There are mainly six blocks in this system: a PT array with 4 sub-PTs, a switch control block, a charge-up block, a SSHI rectifier, a FBR and active diode block, a LDO. On the leftmost side, the output amplitude from each of the sub-PTs is $0.5\,\mathrm{V}$. These sub-PTs can be configured between parallel and series connections depending on whether the cold sate is ended. They are connected in series by default during the cold state, so that 4× higher output V_{OC} is generated from the series-connected sub-PTs to build up a 1.8-V V_{DD}.

A FBR and active diode block is used to rectify the generated AC energy. A LDO is employed to regulate V_{DD} through C_{DD1} and C_{DD2} in cold state. When the cold state finishes and V_{DD} is built up, a RDY signal from a LDO generates a rising edge. Then, the switch control block changes the connection of the 4PTs to parallel for the purpose of extracting more power. And the charge-up block connects

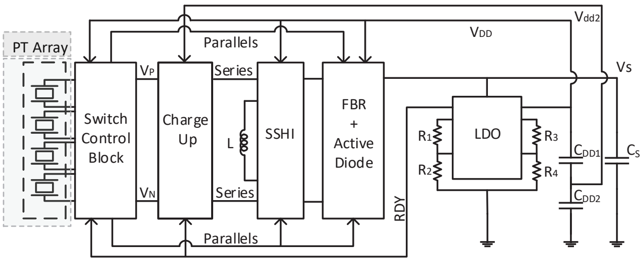

Fig. 4: System block diagram

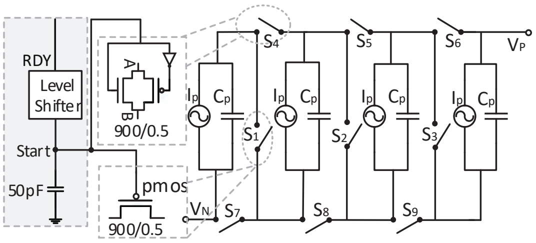

Fig. 5: Switches used in different PTs connections

C_{DD2} to V_P or V_N in one flip cycle to help SSHI rectifier to work normally. Finally, a SSHI rectifier is started to increase the output power efficiency with the stable V_{DD} supply by flipping PT voltage. Circuit implementations of key blocks are presented in the following section.

IV. CIRCUIT IMPLEMENTATION

A. Switch Control Block

As introduced in Section III, 4 PTs are connected in series by default to increase V_{OC} during cold-startup period. The switch control block is shown in Fig. 5. S_1, S_2 and S_3 are PMOS switches and S_4 to S_9 are transmission gate (TG) switches. The RDY signal is generated from a LDO. Through a level shifter, a 'Start' signal is generated. The RDY and 'Start' signal keep at low during cold state to turn on PMOS switches and turn off TG switches to keep 4 PTs connected in series. When required V_{DD} is attained, the RDY and 'Start' become high to turn off PMOS switches and turn on TG switches to change the connection to parallel.

However, since power supply is very small and unstable at the beginning, some ripples may exist in 'Start'. Additionally, due to the large width of the connection switches, MOSFET parasitic capacitors always affect the 'Start' signal. These effects prevent firmly turning on/off MOSFET switches, resulting in some current leakage. To address this issue, an on-chip 50 pF capacitor is added to stabilize the voltage and to eliminate undesired fluctuations in 'Start' signal in Fig. 5.

B. Charge-up Block

When the connection of the PTs changes from series to parallel after the cold-start stage finishes, the SSHI circuit would not work directly, because the PT voltage is decreased by 4× at this moment due to the resulting parallel connection. Additionally, the small resulting V_{OC} (4× lower compared to series connection) is impossible to charge V_{PT} to overcome the threshold voltage. As a result, the SSHI rectifier would not operate properly, and the system would go back to the cold state gradually since parallel-connected PTs cannot transfer any energy through a passive FBR to a high V_S voltage. Thus, a charge-up block is required to help charge V_{PT} to a certain voltage to help SSHI start. The charge block only works for one flip cycle.

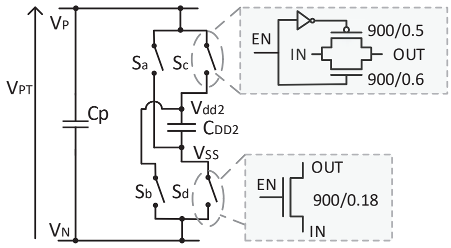

Fig. 6: Charge-up circuit

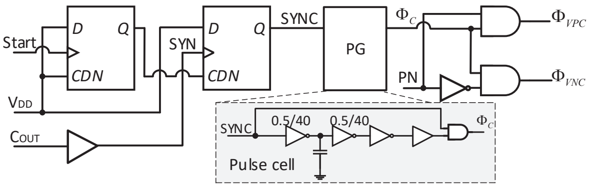

Fig. 7: Charge-up control signals generation

The diagram of the charge up block is shown in Fig. 6; 4 switches are used to charge C_P by connecting it to C_{DD2}. S_b and S_c are TG switches used for charging. S_a and S_d are NMOS switches connected to ground. S_a and S_b are controlled by Φ_{VNC}. S_c and S_d are controlled by Φ_{VPC}. These two phases are generated by the circuit shown in Fig. 7. The 'Start' signal is the same as in Fig. 5. The C_{OUT} is a synchronized signal indicating the moment when the voltage across the PT starts flipping which will be presented in the following sub-section. Through a buffer, the SYN signal is generated. When the SYN generates a rising edge, pulse generation block generates a pulse, Φ_C. The PN indicates the current polarity of V_P and V_N to determine the charging direction.

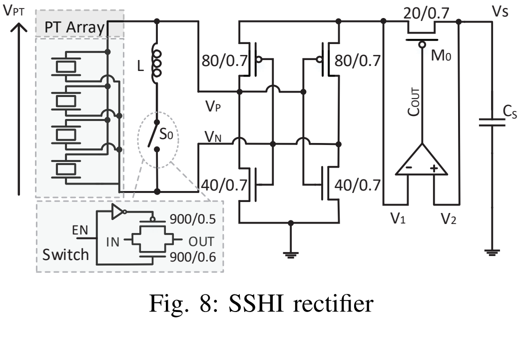

Fig. 8: SSHI rectifier

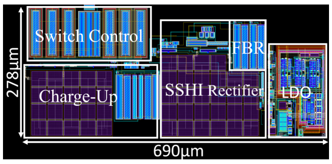

Fig. 9: Proposed layout diagram

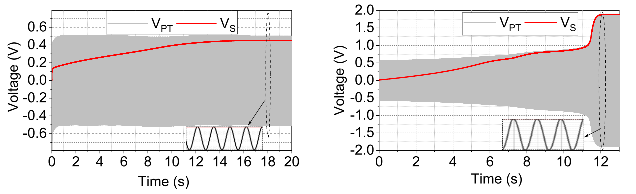

(a) Conventional cold-startup (b) Proposed cold-startup

Fig. 10: Comparison of conventional and proposed cold-startup

C. SSHI Rectifier Block

When the charge-up finishes, the PT voltage is flipped to a certain voltage. And through automatically charging by the generated energy, the PT voltage would be high enough to overcome the threshold to charge C_S. In the next flip cycle, the SSHI rectifier begins to work. A SSHI rectifier is presented in Fig. 9. When $V_1 < V_2$, the output C_{OUT} of the comparator generates a rising edge and M_0 is turned off to prevent the current going out of C_S. This rising edge means the ending time of charging and the starting time to flip V_{PT}. So, it is also employed to generate a pulse to control S_0. The SSHI rectifier employs an inductor temporarily connected into a RLC loop by turning on S_0 to flip V_{PT} to improve output power.

V. POST-LAYOUT SIMULATION ANALYSIS

This system is designed in a 0.18-μm BCD process with the parameters: $V_{OC} = 0.5\,\text{V}$, $C_P = 30\,\text{nF}$, $f_P = 200\,\text{Hz}$, $C_S = 2\,\mu\text{F}$, required $V_{DD} = 1.8\,\text{V}$. A monolithic PT is divided into 4 equal sub-PTs. Fig. 8 displays the layout of the system and the active area is $0.19\,\text{mm}^2$. The corresponding post-layout simulation results are presented as follows. Fig. 10, shows the simulation results of the conventional cold-startup design and the proposed cold-startup design. For the conventional cold-startup circuit, when the input V_{OC} is $0.5\,\text{V}$, the maximum grey V_{PT} is bounded by $0.5\,\text{V}$ while the maximum output red voltage V_S is $0.4\,\text{V}$ in Fig. $10(a)$. $0.4\,\text{V}$ is impossible to build up 1.8-V V_{DD}. In comparison, Fig. $10(b)$ shows the proposed cold-startup simulation result, where the maximum grey V_{PT} is close to $1.9\,\text{V}$. The resulting maximum red V_S is also very close to $1.9\,\text{V}$ which is high enough to build 1.8-V V_{DD}.

Some key signals in the proposed design are shown in Fig. 11. The V_S voltage, is simulated to be charged from $0\,\text{V}$ to $3.5\,\text{V}$. The voltage V_{DD}, is gradually built up to $1.8\,\text{V}$. During startup period, the red 'Start' signal is hold at low to turn on PMOS switches and turn off TG switches in Fig. 5 to keep PTs connect in series. When V_{DD} attains $1.8\,\text{V}$, the cold state is finished and the RDY signal generates a rising edge. At the same time, the 'Start' turns to the high level to follow the V_S to make the PTs connected in parallel by turning off PMOS switches and turning on TG switches.

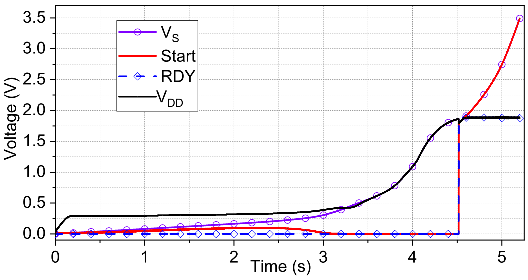

Fig. 11: Output signals of proposed design

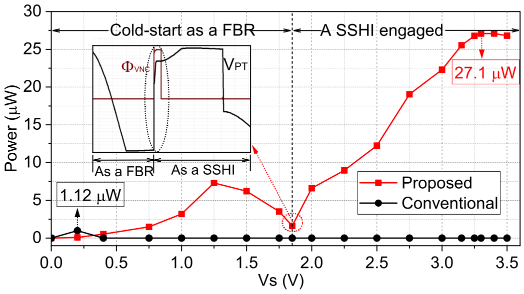

Fig. 12: Output power of proposed design and FBR

Fig. 12 shows the simulated output power related to V_S. Before V_S attains $1.8\,\text{V}$, the system works as a passive FBR and then works as a SSHI rectifier after startup. The maximum output power of the conventional design is $1.12\,\mu\text{W}$, and the corresponding output V_S is limited by $0.4\,\text{V}$. The red line is the output power of the proposed design. When V_S attains $1.8\,\text{V}$ to provide stable 1.8-V V_{DD}, the PTs connection is configured to parallel and the charge-up block generates a phase, Φ_{VNC}, to flip V_{PT} from negative to positive. After the SSHI rectifier starts operating, the output power is significantly increased and V_S can be charged to higher voltage. As a result, the output power becomes higher and attains $27.1\,\mu\text{W}$ when $V_S = 3.3\,\text{V}$.

VI. CONCLUSION

This paper proposes a cold-startup circuit for 0.5-V V_{OC}. The 4 series-connected sub-PTs are used to generate a 4× V_{OC} to build up V_{DD} and change to parallel for the purpose of extracting more power. A LDO is used to generate 1.8-V V_{DD}. A charge-up block is used to help V_{PT} overcome the threshold voltage after cold-startup. A SSHI rectifier is used to improve the output power efficiency by flipping V_{PT}. Corresponding post-layout simulation results show that 1.8-V V_{DD} can be built up even with 0.5-V V_{OC}. The simulated maximum output power is $27.1\,\mu\text{W}$ which is 24× larger than the maximum output power of the FBR.

REFERENCES

[1] A. Morel et al., “A Shock-Optimized SECE Integrated Circuit,” in IEEE Journal of Solid-State Circuits, vol. 53, no. 12, pp. 3420-3433, Dec. 2018, doi: 10.1109/JSSC.2018.2868299.

[2] L. Gao, L. Teng, J. Liang, H. Wang, Y. Liu and M. Fu, “A Self-Sensing Synchronous Electric Charge Extraction (SECE) Solution for Piezoelectric Energy Harvesting Enhancement,” 2021 IEEE Applied Power Electronics Conference and Exposition (APEC), 2021, pp. 1393-1397, doi: 10.1109/APEC42165.2021.9487209.

[3] L. Wu, W. Kang, M. Xie and P. Zhu, “A Self-Powered Multi-Input Bridgeless Series-SSHI Circuit for Piezoelectric Energy Harvesting,” 2021 IEEE International Symposium on Circuits and Systems (ISCAS), 2021, pp. 1-4, doi: 10.1109/ISCAS51556.2021.9401519.

[4] A. M. Eltamaly and K. E. Addoweesh, “A Novel Self-Power SSHI Circuit for Piezoelectric Energy Harvester,” in IEEE Transactions on Power Electronics, vol. 32, no. 10, pp. 7663-7673, Oct. 2017, doi: 10.1109/TPEL.2016.2636903.

[5] D. A. Sanchez, J. Leicht, E. Jodka, E. Fazel and Y. Manoli, “21.2 A 4μW-to-1mW parallel-SSHI rectifier for piezoelectric energy harvesting of periodic and shock excitations with inductor sharing, cold start-up and up to 681% power extraction improvement,” 2016 IEEE International Solid-State Circuits Conference (ISSCC), 2016, pp. 366-367, doi: 10.1109/ISSCC.2016.7418059.

[6] S. Du, Y. Jia, C. Zhao, G. A. J. Amaratunga and A. A. Seshia, “A Fully Integrated Split-Electrode SSHC Rectifier for Piezoelectric Energy Harvesting,” in IEEE Journal of Solid-State Circuits, vol. 54, no. 6, pp. 1733-1743, June 2019, doi: 10.1109/JSSC.2019.2893525.

[7] S. Du and A. A. Seshia, “An Inductorless Bias-Flip Rectifier for Piezoelectric Energy Harvesting,” in IEEE Journal of Solid-State Circuits, vol. 52, no. 10, pp. 2746-2757, Oct. 2017, doi: 10.1109/JSSC.2017.2725959.

[8] X. Yue and S. Du, “Voltage Flip Efficiency Optimization of SSHC Rectifiers for Piezoelectric Energy Harvesting,” 2021 IEEE International Symposium on Circuits and Systems (ISCAS), 2021, pp. 1-5, doi: 10.1109/ISCAS51556.2021.9401330.

[9] P. Angelov and M. Nielsen-Lönn, “A Fully Integrated Multilevel Synchronized-Switch-Harvesting-on-Capacitors Interface for Generic PEHs,” in IEEE Journal of Solid-State Circuits, vol. 55, no. 8, pp. 2118-2128, Aug. 2020, doi: 10.1109/JSSC.2020.2979178.

[10] S. Xi, W. Li, J. Guo and J. Liang, “A Self-Powered Piezoelectric Energy Harvesting Interface Circuit Based on Adaptive SSHI with Fully Integrated Switch Control,” 2020 IEEE International Symposium on Circuits and Systems (ISCAS), 2020, pp. 1-4, doi: 10.1109/ISCAS45731.2020.9180969.

[11] S. H. Nguyen, H. Richardson and R. Amirtharajah, “A Bias-Flip Interface and Dual-Input DC-DC Converter for Piezoelectric and RF Energy Harvesting,” 2021 IEEE International Symposium on Circuits and Systems (ISCAS), 2021, pp. 1-5, doi: 10.1109/ISCAS51556.2021.9401590.

[12] S. Du, Y. Jia, C. Zhao, G. A. J. Amaratunga and A. A. Seshia, “A Nail-Size Piezoelectric Energy Harvesting System Integrating a MEMS Transducer and a CMOS SSHI Circuit,” in IEEE Sensors Journal, vol. 20, no. 1, pp. 277-285, 1 Jan.1, 2020, doi: 10.1109/JSEN.2019.2941180.

B

Publication II

A Highly Efficient Fully Integrated Active Rectifier for Ultrasonic Wireless Power Transfer.

A Highly Efficient Fully Integrated Active Rectifier for Ultrasonic Wireless Power Transfer

Xinling Yue, Zhelun Chen, Yiwei Zou and Sijun Du
Department of Microelectronics, Delft University of Technology, Delft, The Netherlands
Email: sijun.du@tudelft.nl

***Abstract*—Ultrasonic wireless power transfer (WPT) has been proved to be a promising approach to power biomedical implants. To extract the energy generated from the transducer, a rectifier is typically required. Previous inductor-based rectifiers (SSHI and SECE) require a large off-chip inductor to achieve good performance, which is not desired for miniaturization and safety reasons. Synchronized switch harvesting on capacitors (SSHC) rectifiers have been proved to achieve high performance without inductors; however, they are mainly designed for low-frequency kinetic energy harvesting. In this paper, an improved SSHC rectifier is designed to achieve a fully integrated design with all flying capacitors implemented on-chip. The proposed SSHC rectifier can properly operate at ultrasonic excitation frequency ($100\,\mathrm{KHz}$) with precise switching time control and ultrafast voltage flipping techniques. In addition, an on-chip ultralow-power LDO allows the system to be self-sustained. The system is designed in a TSMC 180nm BCD technology and post-layout simulation results are presented.**

***Index Terms*—Biomedical application, energy harvesting, fully integrated, integrated circuit, SSHC rectifier, ultrasonic transducer**

I. INTRODUCTION

In recent years, piezoelectric energy harvesting (PEH) has been applied in various applications, especially in wireless sensors, biomedical implantable devices and wearable electronics [1]. For a PEH system, system miniaturization and energy efficiency are the key factors. In order to realize miniaturization, MEMS process is extensively used to fabricate PEHs. The energy efficiency depends on the performance of the used rectifier. A typically used rectifier in a PEH system is the full-bridge rectifier (FBR) for its stability and simplicity. In addition, a FBR does not depend on power supply to operate; therefore, it does not consider cold-startup ability. However, the high voltage threshold for a FBR significantly curtails the output energy efficiency [2]. In order to improve the efficiency, the Synchronized Switch Harvesting on Inductor (SSHI) rectifier was introduced to flip the voltage across the piezoelectric transducer (PT) by employing an inductor [3]–[6].

On one hand, the SSHI can enhance the performance by employing an inductor to form a RLC loop. On the other hand, the inductance is required around $10\,\mathrm{mH}$, which is not benefit for the system miniaturization, hence, the inductor should be replaced without decreasing the performance. Afterwards, the Synchronized Switch Harvesting on Capacitors (SSHC) rectifier was put forward. Several small switch capacitors were employed to replace the inductor for system miniaturization [7]. However, in previous typical SSHC systems, due to large intrinsic capacitance of PT, the required switch capacitors are too large to be put on a chip. Afterwards, the split-electrode (SE) SSHC rectifier was put forward to achieve fully integrated on-chip [8]. While the SE-SSHC requires thick oxide transistors in the CMOS process. Additionally, a typical SSHC rectifier is mainly designed for low-frequency kinetic energy harvesting, because the required operating period for a SSHC demands adequate time.

The system diagram is displayed in Fig. 1. In this work, as shown in Fig. 1, the ultrasonic PT is composed of an AC current I_P and in parallel with a capacitor C_P. A fully integrated SSHC rectifier is proposed in a standard CMOS process. This is the first time for all the flying capacitors to be implemented on-chip thanks to the small inherent capacitance of ultrasonic PTs. The running ultrasonic excitation frequency is $100\,\mathrm{KHz}$ which desires precise switching time control. A low-dropout (LDO) circuit provides a power supply (VDD) for the proposed transistors, so self-powered system is available. Post layout simulation results are presented to verify the system performance.

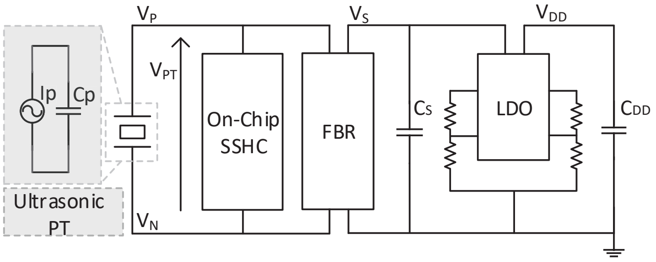

Fig. 1. System Diagram

The structure of this paper is organized as follows: Section II presents the SSHC rectifier in ultrasonic application. Section III shows the circuit implementation. Section IV shows the post-layout simulation results analysis of this proposed system. Finally, a conclusion is given in Section V.

II. SSHC INTERFACE CIRCUIT ANALYSIS

A. Typical SSHC rectifier

The system architecture of the SSHC rectifier is shown in Fig. 2. There are k capacitors and every capacitor is controlled by 4 switches. When the PT voltage flips from positive to negative, the controlled signals are sequenced as

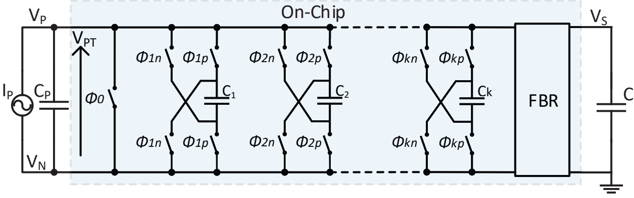

Fig. 2. SSHC Rectifier

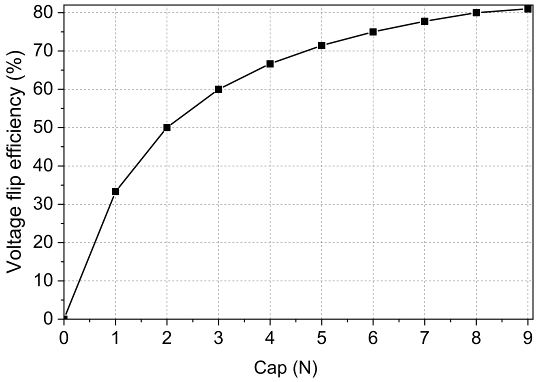

Fig. 3. Voltage flip efficiency related to different number of employed capacitors

$\phi_{1p} \to \phi_{2p} \to \ldots \to \phi_{kp-1} \to \phi_{kp} \to \phi_0 \to \phi_{kn} \to \phi_{kn-1} \to \cdots \to \phi_{2n} \to \phi_{1n}$. The charge in PT are dumped to the k capacitors when the first k phases are operating. Then, ϕ_0 clears the left charge after dumping. The last k phases are used to transfer the charge in the k capacitors to the PT in an opposite direction.

When we use 8 capacitors (k=8) as the flying capacitors, and every capacitance is the same as the intrinsic capacitance of PT, C_P, the flip efficiency is shown in Fig. 3. Fig. 3 shows that with the increasing numbers of capacitor the flip efficiency is also improved. The efficiency is 33% with one flying capacitor and 80% with 8 flying capacitors.

Generally, as shown in Fig 3, for the purpose of achieving high flipping efficiency, it is required to employ capacitance of C_K as same as C_P at least. However, C_P of typical PT is in nano-Farah level resulting in several tens nano-Farah level in total for the required flying capacitors. These flying capacitors are too large to be fully integrated on-chip which is bad for system miniaturization. Afterwards, SE-SSHC was proposed for the purpose of achieving fully integrated by dividing a monolithic PT into several pieces [8]. Although SE-SSHC provides a good method to put these capacitors on-chip, it has to use the thick oxide process for the switches and this is not preferred for a standard CMOS process.

B. SSHC in ultrasonic wireless power transfer

Despite a typical SSHC rectifier is hard to realize fully integrated on-chip, when PTs are used in ultrasonic wireless power transfer, the ultrasonic PTs usually have very small intrinsic capacitance. The size of the ultrasonic PT is not exceed cubic millimeter level in general. While the resonant frequency is above $100\,\mathrm{KHz}$, and the C_P is around $100\,\mathrm{pF}$. When the flying capacitors, C_K, is equal to C_P, the total capacitance is around $800\,\mathrm{pF}$ for a 8-stage SSHC rectifier, which is accessible to fully integrate on-chip. In the measurement, as long as the effective input C_P is smaller than $100\,\mathrm{pF}$, the system performance would not be affected [9]. The benefit of size and flipping time consideration are given as follows.

a) Size analysis: When the system is designed in a TSMC $180\,\mathrm{nm}$ BCD process, we can use the metal-insulator-metal (MIM) capacitor as the flying capacitor. The density of MIM capacitor is $2\,\mathrm{fF}/\mu\mathrm{m}^2$. Considering that when $C_P = 100\,\mathrm{pF}$, the area for the total capacitance of 8 flying capacitors is around $0.5\,\mathrm{mm}^2$. Area cannot be directly compared between a SSHC rectifier and a SSHI rectifier. The estimated minimum volume of this SSHC rectifier should be smaller than $1\,\mathrm{mm}^3$. While considering the same flip efficiency, when using a SSHI rectifier with a several millihenry inductor, the total occupied volume is at least several hundreds times larger than the proposed SSHC rectifier.

b) Flipping time analysis: On the other hand, due to the resonant frequency of the ultrasonic PT is $100\,\mathrm{KHz}$ which indicates $1000\times$ higher than a typical PT. The vibration period is $10\,\mu\mathrm{s}$. Thus, the flipping cycle for the PT voltage is only $5\,\mu\mathrm{s}$. When PT voltage changes the polarity, it is required to finish flipping in a period which is much less than the flipping cycle to avoid excessive energy wasting. In this design, we propose that the flipping time for the SSHC rectifier is no more than 15% of the flipping period.

III. CIRCUIT IMPLEMENTATIONS

This section presents the system architecture of the proposed ultrasonic PT receiver and a selection of key functional blocks in the system. The top level architecture of the design is given in Fig. 4, which contains a pulse generation block, a pulse sequencing block, a on-chip SSHC rectifier, a FBR and an on-chip voltage regulator. The FBR rectifies the received energy from AC to DC while generating a synchronized signal, SYN, which indicates the moment to start voltage flipping. This signal is fed into the pulse generator to generate a sequence of pulses. In this implementation, 8 on-chip flying capacitors require 17 pulses generation in total. These 17 pulses are then sequenced in the pulse sequencing block according to current voltage polarity. The sequenced pulses are level shifted to correct voltage levels to fully drive the switch arrays to perform voltage flipping.

A. Full-bridge rectifier

The FBR block plays a key role to rectify the energy and provide the SYN signal. The circuit diagram of the FBR is given by Fig. 5, which includes a FBR consisting of four MOSFETs and an active diode M_0 controlling by a comparator. The output signal of the comparator, SYN, indicates whether the FBR is conducting or not. When the

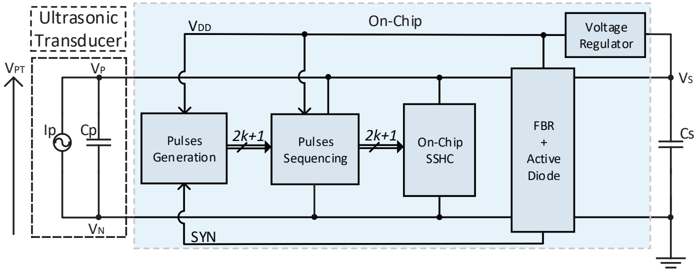

Fig. 4. System Architecture

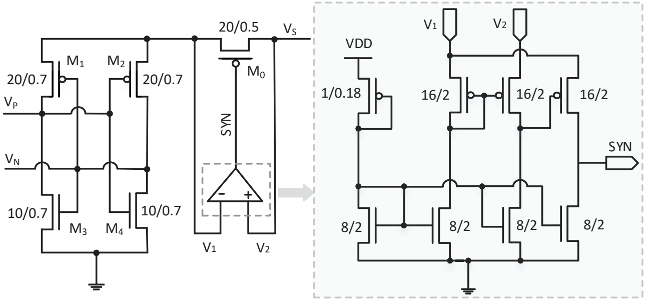

Fig. 5. Full-bridge Rectifier

voltage across the PT needs to be flipped, this is also the moment that the PMOS M_0 is turned OFF to cut off the FBR conduction. At this moment, a rising edge in SYN is generated, which indicates the FBR enters the non-conducting mode and the voltage across the PT needs to be flipped. This rising in SYN is fed into a pulse generation block.

B. Pulse generation

The pulse generation block is shown in Fig. 6, which contains 17 pulse generation cells to generate 17 sequential pulses: ϕ_1 to ϕ_{17}. The first pulse generation cell triggered by a rising edge of SYN. Each pulse generation cell simply ANDs the input with a delayed and inverted version of the input to generate a pulse. The pulse-width can be adjusted by tuning the the variable capacitor C_D to avoid excessive or insufficient flipping time caused by process deviation or parasitic parameter. An enable signal, EN, is added to bypass selected cells if less pulses are required for less enable flying capacitors.

C. Pulse sequencing

The generated 17 pulses are then fed into the pulse sequencing block, which contains 9 pulse sequencing cells. Fig. 7 shows the circuit diagram of one sequencing cell, which takes the i^{th} pulse and the $(17-i)^{th}$ together with a PN signal to sequence the two pulses according to the polarity of PN. The signal PN is generated according to the polarity of the voltage across the PT (V_P and V_N) before flipping is performed, and circuit for generating this signal is also shown at the left of the Figure. After this block, all the 17 pulses are sequenced to drive the switch array (as shown in Fig. 2) for PT voltage flipping by controlling 8 capacitors which are implemented on-chip thanks to the ultra-small inherent capacitance of the ultrasonic PT.

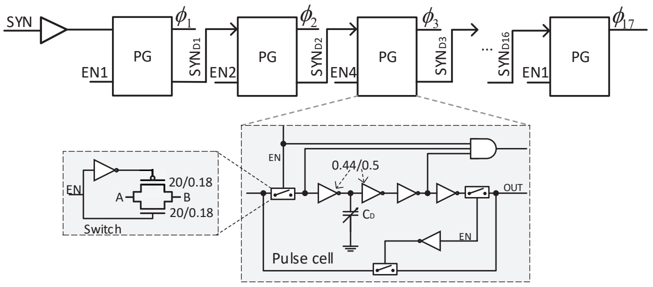

Fig. 6. Pulse Generation Cell

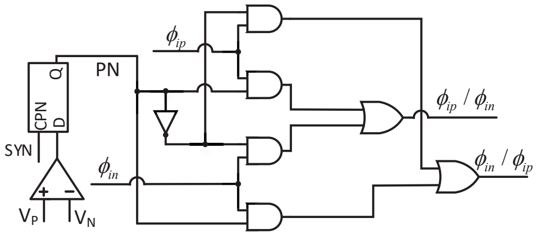

Fig. 7. Sequencing Cell

IV. POST-LAYOUT SIMULATION ANALYSIS

The system is designed in a 180nm BCD process. The piezoelectric ultrasonic transducer used in the simulation has the inherent capacitor, $C_P = 100\,\mathrm{pF}$, and the excitation ultrasonic frequency is set at $100\,\mathrm{KHz}$, which matches the natural frequency of the transducer. Fig. 8 shows that designed layout. The open circuit voltage, V_{OC}, is $2\,\mathrm{V}$. The LDO provides a 1.5-V power supply for the transistors, so the system achieves self-powered sustained. The active area is $0.74\,\mathrm{mm}^2$. Additionally, compared with [8], for the same 8-stage SSHC design with the same technology, the SE-SSHC rectifier takes up $3.9\,\mathrm{mm}^2$, which is above 5.3 × larger than the proposed design in this work. Different from [8], all transistors used in this design are standard process which means that no thick oxide transistor is employed.

Fig. 9 shows the simulated waveform of V_{PT}. When there are 8 switched capacitors, 17 pulses are required to control

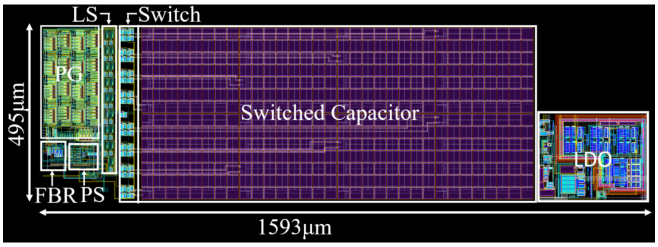

Fig. 8. Layout: PG-Pulse Generation; LS-Level Shifter; PS-Pulse Sequencing

TABLE I
DIFFERENT PERFORMANCE COMPARISON WITH PREVIOUS WORK

Publications	Technique	C_P	$V_{OC}(V)$	F (Hz)	Inductor	On-Chip	Volume (mm^3)	$Power_{Max}$ (μW)	Density$(\frac{Power}{Area})$
ISSCC'16 [12]	SSHI	26nF	2.45	134	3.3mH	No	15.9	160.7	10
TPEL'16 [11]	SECE	52nF	2.35	60	560μH	No	3.5	35	10
ISSCC17 [10]	FCR	78.4pF	1	110K	No	Yes	1.7	50.2	30
JSSC'17 [7]	SSHC	45nF	2.5	92	No	No	1.6	161.8	101
ISSCC'18 [8]	SSHC	1.94nF	2.5	219	No	Yes	5.38	16	2.97
This work	**SSHC**	**100pF**	**2**	**100K**	**No**	**Yes**	**0.74**	**197**	**266**

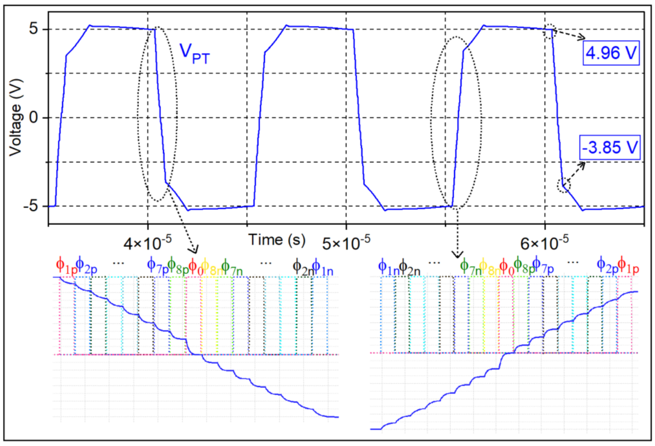

Fig. 9. Waveform of V_{PT} with 80% flip efficiency

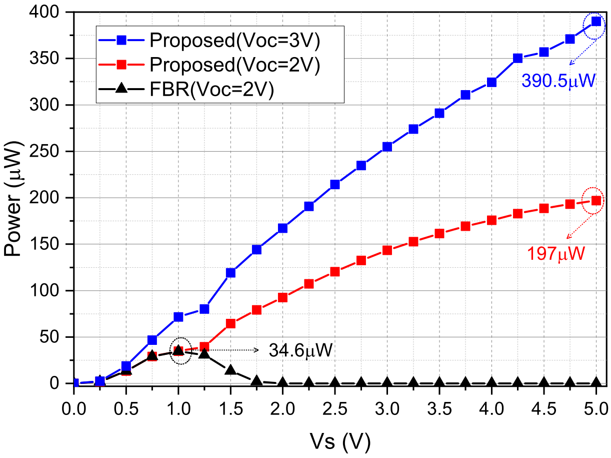

Fig. 10. Different output power comparisons of a FBR and the proposed method

these capacitors. As shown in the Fig. 9, the V_{PT} can be flipped from $4.96\,\mathrm{V}$ to $-3.85\,\mathrm{V}$. The flip efficiency is 78%. The left sub-window shows that When V_{PT} flips from positive to negative, ϕ_{1p}, ϕ_{2p}, $\ldots$, ϕ_{8p} are used to dump the charge from PT to the flying capacitors sequentially. ϕ_0 is used to clear the residual charge in PT. ϕ_{8n}, ϕ_{7n}, $\ldots$, ϕ_{1n} are employed to dump the charge from switched capacitors to the C_P. When V_{PT} changes from negative to positive, these pulses work in a reverse sequence as shown at the right sub-window. Every phase takes up $35\,\mathrm{ns}$, which is above $800\times$ smaller than the one in a typical PT ($29\,\mu\mathrm{s}$). Thus, it requires a more precision switching control than the typical design. The total flipping time of these phases is $0.6\,\mu\mathrm{s}$ which is 11.9% of the flipping period.

Fig. 10 displays the output power of the FBR and proposed design. When $V_{OC} = 2\,\mathrm{V}$, the maximum output power of the FBR is $34.6\,\mu\mathrm{W}$ and approaches to 0 at $V_S = 2\,\mathrm{V}$. While the maximum output power of the proposed SSHC rectifier is $197\,\mu\mathrm{W}$ at $V_S = 5\,\mathrm{V}$, which is $5.7\times$ larger than the FBR. When increase V_{OC} to $3\,\mathrm{V}$, the maximum output power reach $390.5\,\mathrm{uW}$ at $V_S = 5\,\mathrm{V}$ and it is high enough to power sensors and other wireless devices.

Table I displays the different performance comparisons with previous work. The second left column shows the technique used in different works. The next three columns show the parameters of the used PT model, where the C_P is the inherent capacitance of the PT and V_{OC} is the open circuit voltage of the PT. The output power can be increased with a larger V_{OC}. The resonant frequency, F, of this work is $100\,\mathrm{KHz}$ which is relatively high compared with most papers. There is no inductor employed in this work and eight on-chip capacitors are used to flip PT voltage. The total active area is $0.74\,\mathrm{mm}^2$ which is the smallest fully integrated SSHC rectifier. In order to compare this design with other works in volume, especially with SSHI rectifiers, it is assumed $1\,\mathrm{mm}$ for the height. Thus the volume is $0.74\,\mathrm{mm}^3$. The maximum output power when $V_{OC} = 2\,\mathrm{V}$ is $197\,\mu\mathrm{W}$ which is the highest output among these works although with relatively low V_{OC}. The effective density represents the ration of the maximum power over the active area. This work has the highest output power density at $266\mu W/mm^3$.

V. CONCLUSION

This work investigates a fully integrated active SSHC rectifier with standard CMOS technology in ultrasonic PT application. The resonant frequency of employed ultrasonic PT is $100\,\mathrm{KHz}$ which is $1000\times$ larger than a typical PT. The intrinsic capacitor, C_P, is $100\,\mathrm{pF}$ which provides the possibility to fully integrate the flying capacitors on a chip. 8 flying capacitors are employed to achieve 80% flip efficiency to improve the power efficiency. The simulated maximum output power is $390.5\,\mu\mathrm{W}$ with $V_{OC} = 3\,\mathrm{V}$ and is able to power the biomedical implants.

REFERENCES

[1] P. D. Mitcheson, E. M. Yeatman, G. K. Rao, A. S. Holmes and T. C. Green, “Energy Harvesting From Human and Machine Motion for Wireless Electronic Devices,” in Proceedings of the IEEE, vol. 96, no. 9, pp. 1457-1486, Sept. 2008, doi: 10.1109/JPROC.2008.927494.

[2] L. J. Blystad, E. Halvorsen and S. Husa,“Piezoelectric MEMS energy harvesting systems driven by harmonic and random vibrations,” in IEEE Transactions on Ultrasonics, Ferroelectrics, and Frequency Control, vol. 57, no. 4, pp. 908-919, April 2010, doi: 10.1109/TUFFC.2010.1495.

[3] A. Badel, D. Guyomar, E. Lefeuvre, and C. Richard, “Efficiency enhancement of a piezoelectric energy harvesting device in pulsed operation by synchronous charge inversion,” Journal of Intelligent Material Systems and Structures, vol. 16, no. 10, pp. 889–901, 2005.

[4] G. D. Szarka, S. G. Burrow, and B. H. Stark, “Ultralow power, fully autonomous boost rectifier for electromagnetic energy harvesters,” IEEE Transactions on Power Electronics, vol. 28, no. 7, pp. 3353–3362, 2013.

[5] S. Du et al., “An efficient sshi interface with increased input range for piezoelectric energy harvesting under variable conditions,” IEEE Journal of Solid-State Circuits, vol. 51, no. 11, pp. 2729–2742, 2016.

[6] E. E. Aktakka and K. Najafi, “A micro inertial energy harvesting platform with self-supplied power management circuit for autonomous wireless sensor nodes,” IEEE Journal of Solid-State Circuits, vol. 49, no. 9, pp. 2017–2029, 2014.

[7] S. Du and A. A. Seshia, “An inductorless bias-flip rectifier for piezoelectric energy harvesting,” IEEE Journal of Solid-State Circuits, vol. 52, no. 10, pp. 2746–2757, 2017.

[8] S. Du and A. A. Seshia, “A fully integrated split-electrode synchronized-switch-harvesting-on-capacitors (se-sshc) rectifier for piezoelectric energy harvesting with between 358enhancement,” in 2018 IEEE International Solid - State Circuits Conference - (ISSCC), Feb 2018, pp. 152–154.

[9] X. Yue and S. Du, “Voltage Flip Efficiency Optimization of SSHC Rectifiers for Piezoelectric Energy Harvesting,” 2021 IEEE International Symposium on Circuits and Systems (ISCAS), 2021, pp. 1-5, doi: 10.1109/ISCAS51556.2021.9401330.

[10] Z. Chen, M. Law, P. Mak, W. Ki and R. P. Martins, ”22.2 A 1.7mm2 inductorless fully integrated flipping-capacitor rectifier (FCR) for piezoelectric energy harvesting with 483% power-extraction enhancement,” 2017 IEEE International Solid-State Circuits Conference (ISSCC), 2017, pp. 372-373, doi: 10.1109/ISSCC.2017.7870416.

[11] M. Dini, A. Romani, M. Filippi and M. Tartagni, “A Nanopower Synchronous Charge Extractor IC for Low-Voltage Piezoelectric Energy Harvesting With Residual Charge Inversion,” in IEEE Transactions on Power Electronics, vol. 31, no. 2, pp. 1263-1274, Feb. 2016, doi: 10.1109/TPEL.2015.2417352.

[12] D. A. Sanchez, J. Leicht, E. Jodka, E. Fazel and Y. Manoli, “21.2 A 4μW-to-1mW parallel-SSHI rectifier for piezoelectric energy harvesting of periodic and shock excitations with inductor sharing, cold start-up and up to 681% power extraction improvement,” 2016 IEEE International Solid-State Circuits Conference (ISSCC), 2016, pp. 366-367, doi: 10.1109/ISSCC.2016.7418059.